Master Thesis, Department of Geosciences

The polar low in the Norwegian Sea March 16-17 2008

Bjørg Jenny Kokkvoll Engdahl

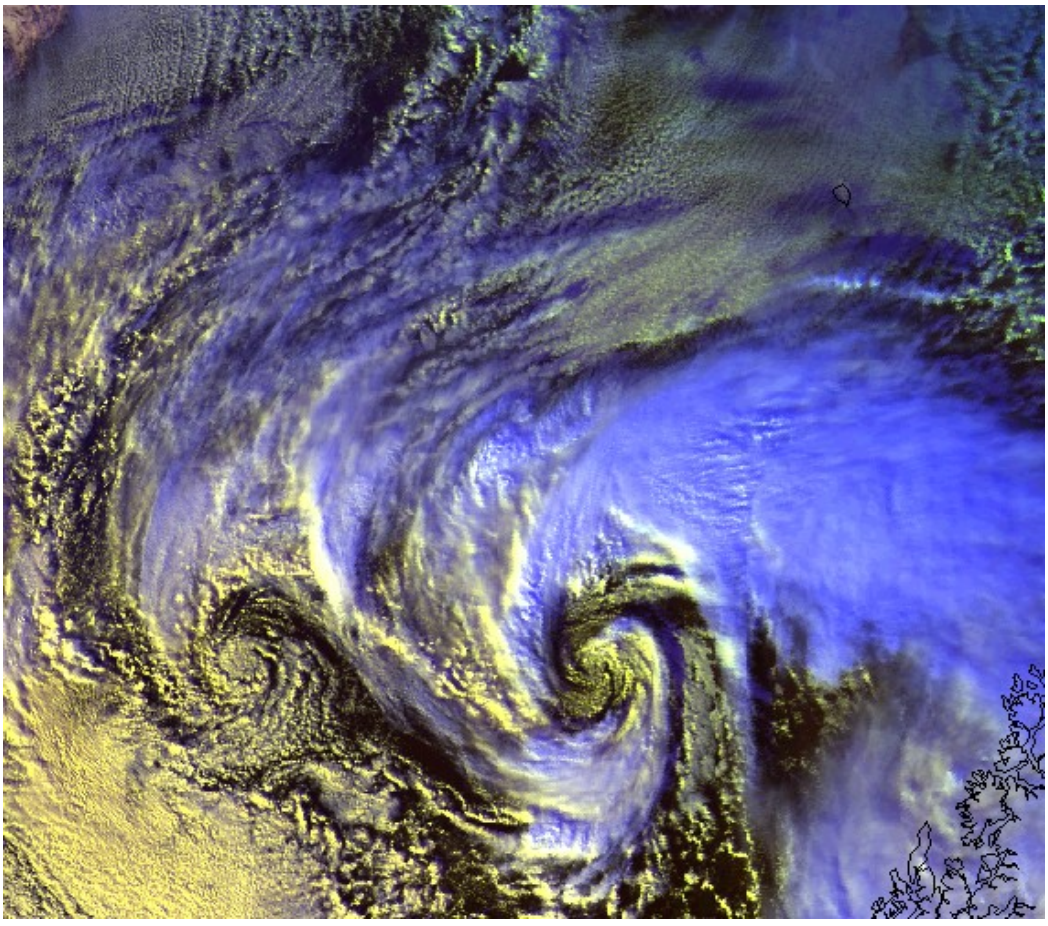

NOAA-16 SAF_SE day_night 2008-03-16 1508 UTC

UNIVERSITY OF OSLO

FACULTY OF MATHEMATICS AND NATURAL SCIENCES

The Polar Low in the Norwegian Sea March 16-17 2008

Bjørg Jenny Kokkvoll Engdahl

Master Thesis in Geosciences

Discipline: Meteorology and Oceanography

Department of Geosciences

Faculty of Mathematics and Natural Sciences

University of Oslo

01.12.2011

Contents

Abstract

The polar low in the Norwegian Sea on March 16-17 2008 has been studied using both weather analysis and the numerical weather prediction (NWP) model weather research and forecasting (WRF). This particular polar low was poorly forecasted by several operational models, and has therefore been subject to this study. Weather analysis show that the low developed during a complex weather situation, in a confluence zone between polar and arctic air. It was one of three vortices found simultaneously in a wave-like cloud pattern along the confluence zone. There was a clear upper-level forcing by an advancing potential vorticity (PV) anomaly, along with strong convection during the cyclogenesis stage. The polar low developed in a region of the confluence zone with relatively high surface temperature and low static stability in the lower troposphere. It is suggested that this contributed to the rapid development of the vortex, and that the two other vortices might not have experienced this.

Sensitivity studies with different initial times, high resolution runs and different parametrisation schemes representing microphysics, cumulus clouds and planetary boundary layer, were carried out. There were great deviations between all the simulations, particularly regarding time and location of development as well as trajectory and depth of the polar low, but all managed to produce at least one clear low. Most of the models produced several lows, which could be connected to the multiple vortices found in the confluence zone.

The simulations initiated after cyclogenesis reproduced the depth of the polar low much better than the simulations initiated before cyclogenesis. It appears that the model have trouble simulating particularly the rapid development at the early stage. In contrast to previous studies, the high resolution runs did not improve the forecast much. The sensitivity study of the different parametrisation schemes of microphysics, cumulus clouds and planetary boundary layer, only showed improvements by changing the boundary layer scheme. It is concluded that the WRF simulations produced a much improved forecast compared to the operational HIRLAM simulations, and also the UM simulations carried out by McInnes et al. (2011). It is suggested that this may be due to better lateral boundary conditions due to the nesting option in WRF. Further investigations could reveal if the WRF model, in general, is be better suited for polar low forecasts than the operational HIRLAM.

Acknowledgements in Norwegian

Først og fremst vil jeg takke min veileder, Jón Egill Kristjánsson, for nyttige diskusjoner og god veiledning. Min medveileder Trygve Aspelien skal ha stor takk for all hjelp med DIANA. Jeg vil også takke Nedre Blindern Flisespikkeri representert ved Filip, Beate, Anders, Christian, Anette, Matias og Helga for korrekturlesning av ypperste kvalitet. Min gode bror Geir, skal ha en kjempestor takk for å ha korrekturlest hele oppgaven, og reddet meg fra "the clam center". Kyrre og Irene fortjener også en takk for å ha hjulpet meg med latex .

Mine medstudenter skal ha takk for et hyggelig miljø på MetOs og gode sosiale og faglige samtaler. Generelt vil jeg takke Studentorchesteret Biørneblæs som har gjort torsdag til den beste dagen i uka og for å male en ellers grå hverdag, gul og grønn. Ellers vil jeg også takke mine andre venner som ikke faller inn i de to foregående kategoriene. Jeg vil spesielt takke min familie for alltid å ha troen på meg og støtte mine valg. Denne oppgaven har vært svært spesiell å jobbe med ettersom jeg mistet min far, Øyvind, samme dag som det polare lavtrykket oppstod. Jeg vet du har vært med meg gjennom hele oppgaven. Takk for at du alltid støttet meg.

Sist, men ikke minst, skal min kjæreste, Øyvind, ha den største takken av alle. Både for å ha hjulpet med det tekniske og lest korrektur, men også for å stille opp med kake på lesesalen, god mat når jeg kommer hjem og for å holde ut med meg når frustrasjonen tar overhånd.

Blindern, 1.desember 2011
Bjørg Jenny Kokkvoll Engdahl

Chapter 1

Introduction

1.1 Polar lows

Polar lows are mesoscale low pressure systems that usually form over open water at high latitudes during the winter season. Both their spatial and temporal scales are smaller than ordinary synoptic lows, having a horizontal extent of around 200-1000km (McInnes et al. (2011)) and lasting from a couple of hours to a couple of days (Blechschmidt (2008)). The formation of polar lows is normally associated with cold air outbreaks, where cold, dry air from above the polar icecaps is advected towards open water and the relatively warm and moist air over the ocean surface (Kolstad (2006)). This results in strong vertical turbulent fluxes of heat and moisture from the ground surface and a reduced static stability in the lower troposphere (Kristiansen et al. (2011)).

Polar lows are sometimes referred to as arctic hurricanes because of their sometimes hurricane-like appearances, with bands of clouds spiralling out from a cloud-free "eye". This type of polar lows is called spiraliform polar lows, and the mechanisms driving them also resembles the mechanisms behind tropical cyclones (Rasmussen and Turner (2003)). Spiraliformed polar lows are also often referred to as convective polar lows, where the main forcing mechanism behind is thermal instability. But polar lows also appear in several other forms with different forcing mechanisms. For instance a comma shaped polar low, with cloud bands resembling a comma, which is usually a mainly baroclinic system. These kinds of systems take their energy from the main baroclinic flow, which may appear when there is a clear difference in the wind speed and direction between the lower and higher tropospheric layer of air masses. Blechschmidt (2008) studied 90 polar lows that occurred in 2004 and 2005, and found that the number of comma shaped lows were five times higher than spiraliformed lows.

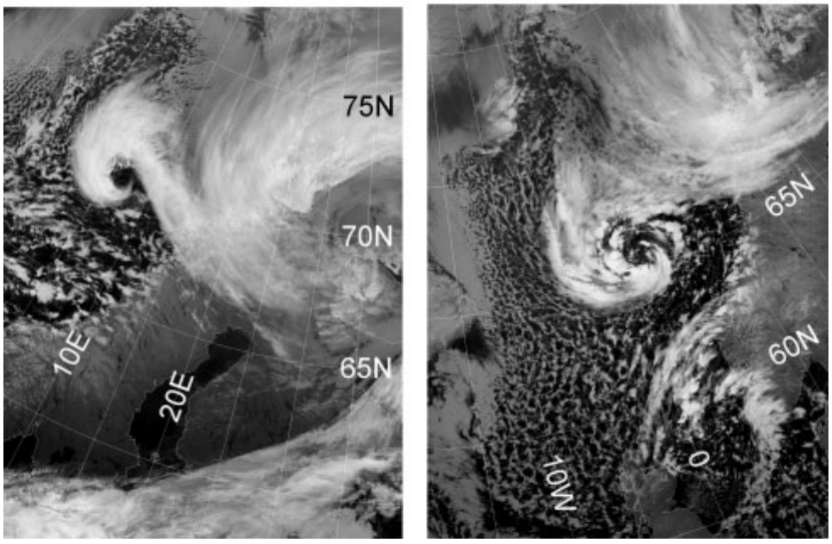

(a) A comma shaped polar low. (b) A spirali form polar low.

Figure 1.1: IR-satellite images of two polar lows. NOAA AVHRR imagery retrieved from the NERC Dundee Satellite Receiving Station. In Bracegirdle and Gray (2009).

Figure 1.1 shows the infrared (IR) satellite images of two different polar lows where 1.1(a) is a typical comma shaped low and 1.1(b) is typical spiraliform.

Polar lows can occur from middle to high latitudes in the winter season, but are more common at high latitudes near the ice edge. The Norwegian coast and waters are highly exposed to polar lows, as the weather conditions over the seas surrounding the country, particular the Norwegian Sea, often are favourable for polar low development during the winter season (Kolstad (2006)). High sea surface temperatures (SST) in the Norwegian and Barents Sea favour polar low development.
The most dangerous aspects with polar lows are the strong and shifting winds, combined with heavy precipitation, normally in the form of snow (Rasmussen and Turner (2003)). The polar lows that impact Norway are usually formed in a generally northerly main wind direction due to a cold air outbreak. Since the wind spins around the low counterclockwise, there will not be just an increase in the main wind speed on the western side of the low, but also a decrease in the main wind speed on the eastern side. This can give a sort of false calm when the storm first reaches land. In a television documentary about the IPY-THORPEX Andøya campaign, a fisherman from Northern Norway explained how he and his brother saw a wall of dark clouds approaching from the north when they were surprised by a poorly forecasted polar low (Kristjánsson et al. (2011). The consequences

were fatal, as their boat capsized and his brother drowned.

Hardly any polar lows are just baroclinic or just convective. Most of them are a mix between barotropic and convective systems, and it is therefore more common to refer to the polar low spectrum instead of a common phenomenon (Kristiansen et al. (2011)). The range of the polar low spectrum and the variety of the different forcing mechanisms for triggering, development and intensification is one of the main reasons why polar lows are difficult to forecast. Few observations from the areas where polar lows occurs also contribute to the difficulties (Kristjánsson et al. (2011)), and is still a major problem for verifying model simulations and increasing knowledge about the lows.
Another problem is the mesoscale size, mostly in the order of 100km in horizontal extent, making it a challenging task to forecast by the coarser grid weather models designed to forecast synoptic scale weather systems (McInnes et al. (2011)). In addition to the relatively small horizontal scale, the time scale of polar lows is also small compared to larger weather systems, which means that they can develop during a short period of time, making it even more difficult to forecast. This has, however, greatly improved over the past few years, as computing capacity has increased, making it possible to run the weather models with a much higher resolution than previously. But even nowadays, many polar lows are not well forecasted, and those that are picked up by the operational forecasts often only give a few hours warning.

Unfortunately, this is not much time to warn potentially threatened ships and onshore settlements. They will need more time to secure lives and property should the polar low develop close to human activities. There are also still some problems that remain unsolved considering that the weather models often have trouble predicting the strength, position and trajectory of the polar lows.

1.2 Short historical review and background

Polar lows first caught attention in the 50's with the introduction of satellites, as satellite images revealed small vortices of clouds at high latitudes. Although the effects of polar lows had been known by sailors and coastal communities for centuries earlier, and Norwegian weather forecasters were also well aware of the lows, it was nearly impossible to forecast them with just the data from the synoptic observation network (Rasmussen and Turner (2003)).
Peter Dannevig, was one of the first to refer to polar lows, when he wrote a paper on "instability lows" in the seas around Norway in 1954. He suggested

that the vortices were related to the typical airflow around Norway during a cold-air outbreak, and also considered that the mechanisms behind their formation could be thermal instability as in tropical cyclones.
British meteorologists also took keen interest in polar lows, as these phenomena could bring extensive snowfall across the British Isles. The first British case studies of polar lows were published as early as in 1960, and were based on routine surface observations. Satellite images were not much used before the arrival of the polar orbiting satellites, that provided sounder measurements, scatterometer data for estimation of surface winds, and microwave data.
Theoretical studies considering the development of polar lows were carried out parallel to the observational studies. During the late 60's and 70's scientists discussed if the mechanisms behind polar lows were mainly baroclinic or convective. The Norwegian Polar Lows Project from 1983-1985, improved the knowledge of polar lows significantly. During the project the first aircraft observations were collected from within a polar low, a climatology of polar lows was prepared and modelling studies were carried out. Even though the knowledge of polar lows has increased rapidly during the last decades, there are still many questions left unanswered and the subject remains active.

1.3 The polar low from March 16-17

A few field campaigns have been carried out recently in order to increase the knowledge of polar lows. The polar low in this study occurred during a field campaign launched by IPY-THORPEX. The field campaign lasted for three weeks in February and March 2008, and two polar lows occurred in that period: one from March 3-4 and the other from March 16-17 (Kristjánsson et al. (2011)). Around midnight on March 16 2008, a development within an area of high cumulus clouds in connection with a trough, occurred roughly one hundred kilometres west of the coast of northern Norway. This is only some 100km away from Andenes, where the IPY-THORPEX Andøya field campaign was situated at that time. During the night and morning hours the disturbance developed into a polar low. It remained almost stationary through most of the day on March 16, and deepened. Later in the evening the polar low moved southwards almost parallel with the coast of Nordland in Northern Norway, and had by that time the appearance of a spiraliform polar low. The low lasted for about 36 hours, before it made landfall at the coast of Trøndelag in middle Norway around 1200 UTC on March 17.
What made this polar low so special is that it was not very well forecasted. It was expected that a polar low would develop as the weather conditions were favorable for polar low development, but the operational weather models had forecasted that the low would develop further to the north-west, some

hundred kilometers away. The forecasts made during the presence of the polar low also predicted the low to move earlier and faster southwards than it actually did. Figure 1.2 shows the MODIS Terra infrared satellite image from 1050 UTC on March 16 2008. The polar low has a clear comma-shape and is located at 71.5°N, 11°E. L1, L2 and L3 denote predicted positions (+36 h) of the polar low at 12 UTC by three major operational models at the time (Kristjánsson et al. (2011)). The operational models miss out on the real polar low by several hundred kilometres. As the low itself is only around 300km wide, this would make a huge difference to for instance ships and coastal settlements. In this particular event, the consequences of the operational weather models' misplacing of the polar low were not too dramatic. But for later review, it is discouraging, as on another occasion there can be ships or other human interests involved, which need accurate weather forecasts.

The March 3-4 polar low has been thoroughly studied and several papers have been written, for instance: "*The full life cycle of a polar low over the Norwegian Sea observed by three research aircraft flights*" by Føre et al. (2011) and "*The mesoscale structure of a polar low: airborne lidar measurments and simulations*" by Wagner et al. (2011). In these studies it appears that the polar low was well forecasted, and that the three research aircraft flights were successful, giving valuable data of the whole life cycle of the polar low. The three-dimensional structure of the polar low was investigated using dropsonde data and LiDAR[1]. Fluxes of latent and sensible heat were also estimated. Satellite images and operational modelling data were also used in order to get a more complete image of the life cycle of the polar low.

Both the March 3-4 and 16-17 polar low were studied in the paper *Short-range probabilistic forecasts from the Norwegian limited-area EPS: long-term validation and a polar low study* by Aspelien et al. (2011). The purpose of this study was to validate a short-range Ensemble Prediction System (EPS) called LAMEPS for the two polar low cases. The polar lows are briefly described in this study based on satellite images. This study concludes that the LAMEPS is very well able to forecast the March 3-4 polar low, but the March 16-17 case was a lot poorer forecasted and the authors suggested that this was because of the more complex development of this polar low.
This polar low was also studied briefly by Linders and Saetra (2010) and McInnes et al. (2011). Linders and Saetra (2010) addressed the convective available potential energy (CAPE) by analysing the data from the dropsondes. McInnes et al. (2011) tried to simulate the polar low using the Unified Model (UM) from the UK Met Office, but the model failed to even produce a low. Only Randriamampianina et al. (2011) studied the 16-17 March polar

[1]Light Detecting And Ranging.

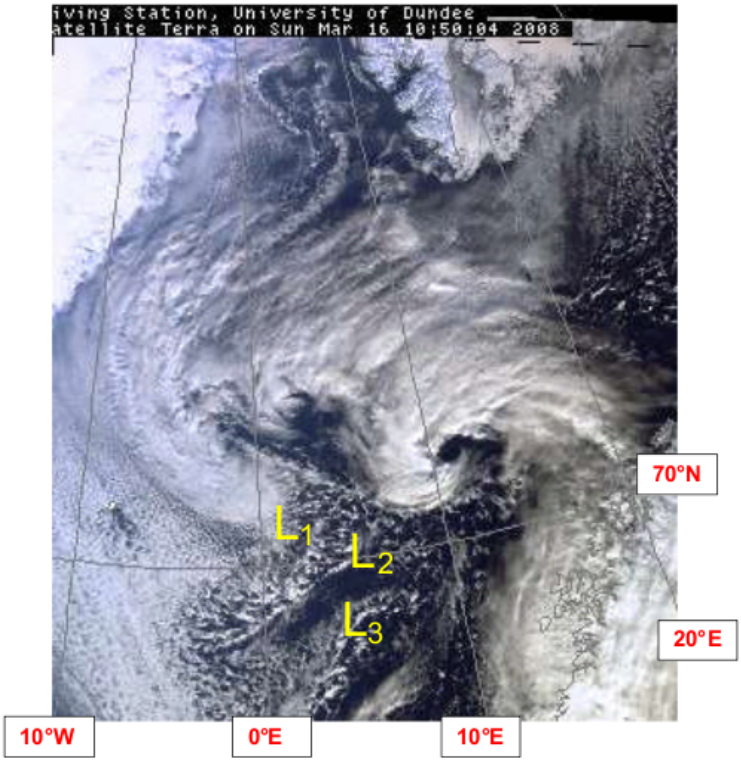

Figure 1.2: A MODIS Terra IR satellite image from 1050 UTC on March 16 2008. The image was obtained from the web server of the University of Dundee (http://www.sat.dundee.ac.uk). L1, L2 and L3 denote predicted positions (+36 h) of the polar low at 12 UTC by three major operational models at the time. From Kristjánsson et al. (2011)

low in particular. Their method of assimilating Infrared Atmospheric Sounding Interferometer (IASI) radiances from satellites, improved the forecast of the low considerably, but still placed the development of the low too far west.

1.4 Outline of this study

The objective of the present study is to find out why the March 16-17 polar low was so difficult to forecast, and how future forecasts can be improved. The means of doing so is twofold; First, the weather conditions prior to, and forcing mechanisms during the formation and life cycle of the low, will be analysed. Secondly, several simulations using the NWP model, Weather Research and Forecasting (WRF), are performed to see if this model is able to provide a better forecast, and address the factors that may affect the model's ability to do so.

The theory will be thoroughly described in chapter 2. This chapter will consider both the general theories for polar lows, and also go deeper into the theory that may be particularly interesting for this low. In chapter 3, the method used to investigate and model the polar low will be given. This will contain both how the observations were obtained, along with a description and a thorough explanation of the WRF model. In chapter 4, satellite images, dropsondes and ECMWF's[2] model analyses are used to give a general picture of the polar low. Chapter 5 presents and discusses the results from the WRF simulations. Finally a conclusion is given in chapter 6.

[2]European Center for Medium-Range Forecast.

Chapter 2

Theory

This chapter aims to give a general understanding of polar lows, and also a deeper explanation on the theories that may describe the development, motion and structure of the polar low March 16-17 2008 in particular. The theory is mostly taken from chapter 4 in Rasmussen and Turner (2003), written by A. Van Delden et al. Different forcing mechanisms for cyclogenesis are addressed first, with baroclinic and thermal instability as well as upper-level forcing and means of recognising this. Structure of a mature polar low will be described during the final section.

2.1 Cyclogenesis

Polar lows usually form near the ice edge during a cold air outbreak. Marine cold-air outbreaks (MCAOs) are large-scale departures of cold, polar air masses over warm, ice free waters (Kolstad et al. (2008)). Due to the relatively high wintertime sea surface temperatures (SSTs) along the North Atlantic Current, this phenomenon is common during winter. During these events, the static stability of the lower troposphere is severely lowered due to the high fluxes of sensible and latent heat, which can trigger various weather conditions such as arctic fronts, roll clouds, fog, icing and polar lows. Blechschmidt et al. (2009) found a typical temperature difference of 48°K between the surface and the 500hPa layer and a geopotential height at 500hPa about 5030 meters, during MCAOs. In addition to MCAOs, there are a variety of factors that are known to contribute to polar low development, such as surface baroclinicity and upper-level forcing.

The relative importance of the different forcing mechanisms vary a lot from various polar lows. This is because of the different environments they develop in, from regions with high baroclinicity, around the main baroclinic

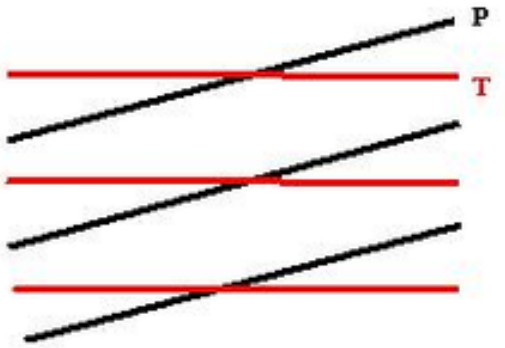

Figure 2.1: Isobars (black lines) and isothermals (red lines) in a horizontal plane in a baroclinic region. From wikipedia: http://en.wikipedia.org/wiki/Baroclinity .

zone, to nearly barotropic regions, where convective instability plays a major role (Rasmussen and Turner (2003)).
In the late 70's and early 80's, it was thought that polar lows were either baroclinic disturbances or convective systems. This view gradually changed into the understanding that both mechanisms were important, and generated a spectrum of polar lows. A study by Wilhelmsen (1985) from 1978-85, suggested seven types of polar low classes, based on synoptic patterns associated with the polar lows, and the basic mechanisms for development. The groups are: Reverse shear systems, trough systems, boundary layer front type, cold low types, comma clouds, baroclinic waves and orographic polar lows.

2.1.1 Baroclinic instability

One of the main forcing mechanisms for development of polar lows is baroclinic instability. A baroclinic region is defined as a region where the density is dependent on both temperature and pressure, and not just pressure as in barotropic regions. The baroclinicity of a region is proportional to $\nabla p \times \nabla \rho$ and can be seen in a horizontal plane as regions where the isobars and isothermals do not run parallel, as illustrated in figure 2.1.

The instabilities grow by converting potential energy associated with the mean horizontal temperature gradient into kinetic energy (Holton (2004)). This is done by lowering the center of gravity in the fluid. Perturbations in an unstable flow will grow in time, and eventually develop into larger systems, such as storms.
Jules Charney (1947) and Eric Eady (1949) were the first to suggest baroclinic instability as one of the main forcing mechanisms for development of synoptic cyclones at middle-latitudes.

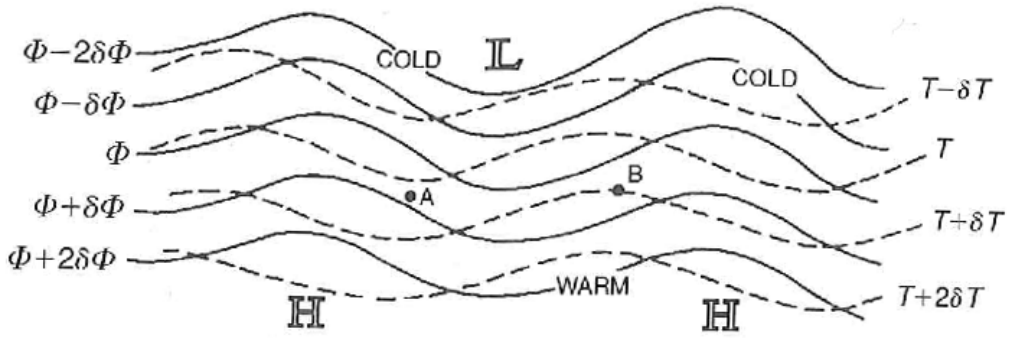

Figure 2.2: The distribution of geopotential height (solid lines) and temperature (broken lines) on a constant pressure surface in a developing baroclinic wave in the Northern Hemisphere. The pressure surface is located near the level where the speed of the wave is the same as the speed of the mean zonal flow. (From Wallace and Hobbs, 1977, in Rasmussen and Turner, 2003.)

Rasmussen and Turner (2003) give a good example on how an initially small perturbation in a baroclinic environment grows. The example is reproduced here, with an illustration in figure 2.2. A small perturbation is induced into a uniform zonal flow, by some external forcing like for instance topography. The meridional motions associated with the perturbation will distort the originally east-west oriented isotherms causing a wave in the temperature field to form. This wave will be displaced one quarter of a wavelength to the west of the pressure field. The distortion of the isotherms will be further increased by the horizontal temperature advection in association with the pressure field. The wave in the temperature field will grow because of the difference in temperature between point A and B in figure 2.2. The warm air at point B will rise and the cold air at point A will descend, and by that lowering the fluids center of gravity.

Type A, B and C cyclones

Pettersen and Smebye (1971) discussed the role of upper-level troughs for development of baroclinic waves (Rasmussen and Turner (2003)). They suggested two ways that lead to development of extratropical cyclones. The first, type A, was characterized by a development under a straight upper-level current, and an initially strong low-level baroclinicity that decreases as the wave occludes (figure 2.3 top panel). There is a characteristic phase locking between the upper- and lower-level trough during intensification (Bracegirdle and Gray (2008)). The intensification is dominated by lower-level forcing (mainly thermal advection), but the upper-level forcing (mainly vorticity advection) may increase as the cyclone intensifies.
Type B development is when an upper-level trough with high vorticity on

its forward side, spreads over an area of low-level warm advection. Mostly a type B development is referred to when an upper-level disturbance initiates development over a low-level baroclinic zone (Rasmussen and Turner (2003)). The middle panel in figure 2.3 shows type B development. As the cyclone intensifies, the tilt between the upper- and lower-level troughs decreases. The intensification is dominated by upper-level forcing (mainly vorticity advection) which decreases as the cyclone intensifies, while the lower-level forcing (mainly thermal advection) increases from initially low values (Bracegirdle and Gray (2008)).

Deveson et al. (2002), suggested a third type of extratropical cyclone that did not fit into either of the former categories. The most notable feature of these cyclones was the crucial role of strong latent heat release. These type C cyclones (figure 2.3 bottom panels) possessed large forcing by pre-existing upper-level troughs (suggestive of type B), remained phase locked during intensification (suggestive of type A) and possessed weak baroclinicity in the lower troposphere.
Plant et al. (2003) described type C cyclogenesis as an interaction of an upper-level potential vorticity (PV) anomaly, with a low-level diabatically generated PV-anomaly and pointed out the role of latent heat release as a substitute of for the basic state baroclinicity.

Bracegirdle and Gray (2008) found in their study a distinct contrast between the north and south in the Nordic Seas. Type C cyclones were dominant in the southern part of the Norwegian Sea, while type A and B cyclones dominated the northern part of the Norwegian Sea and the Barents Sea. This is consistent with weak low-level baroclinicity and widespread conditional instability found in the southern Norwegian Sea, and the more baroclinic regions found in the northern Nordic seas.

Reverse-shear lows

An important group of polar lows are the reverse-shear lows. They differ from the "normal" baroclinic systems in the way that the wind at the low-level steering level is opposite to the thermal wind in the adjoining layers (Kolstad (2006)). The wind speed generally decreases with height and there is a forward tilt of the disturbances in the vertical direction. Figure 2.4 illustrates the difference between a reversed-shear flow and a forward shear flow. Relative to the motion of the system, there will be warm air to the left, and cold air to the right of the path. The effects of horizontal advection will be to move warm air behind the trough so that kinetic energy will be gained at the expense of available potential energy if ascending motion predominate behind the trough with descending motion in the cold air ahead (Rasmussen

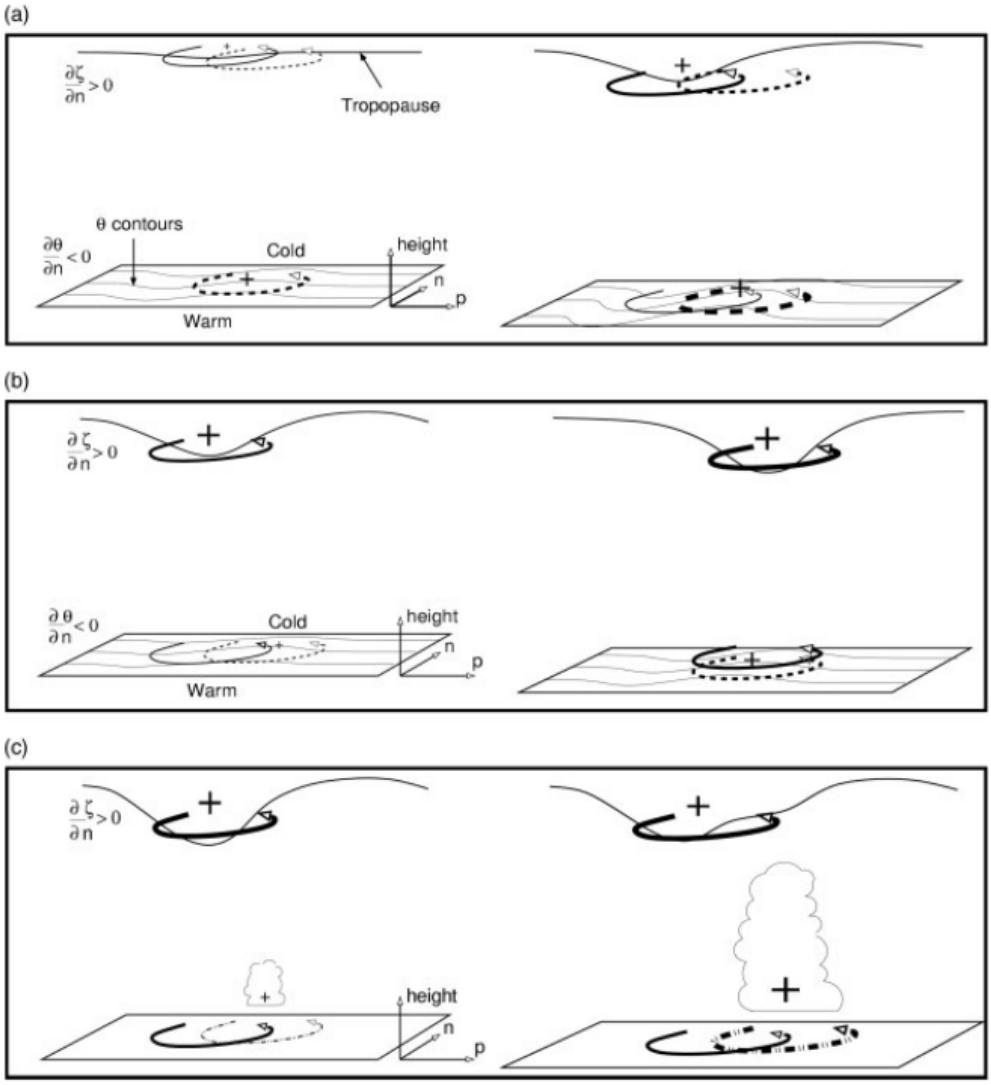

Figure 2.3: The structure and evolution of cyclogenesis types A (top panel), B (middle panel) and C (bottom panel). For each cyclone type both the early period of development and mature system are shown. The local and remote circulations due to different forcings are shown in different line styles (solid for upper-level vorticity anomalies, dashed for lower-level thermal anomalies and dot-dashed for mid-level latent heat release). The relative strength of the circulations is qualitatively indicated by the thickness of the arrows. The p-axis is parallel to the environmental near-surface temperature gradient with cold to the left. The n-axis is normal to the p-axis and points towards the cold air. From Bracegirdle and Gray (2008).

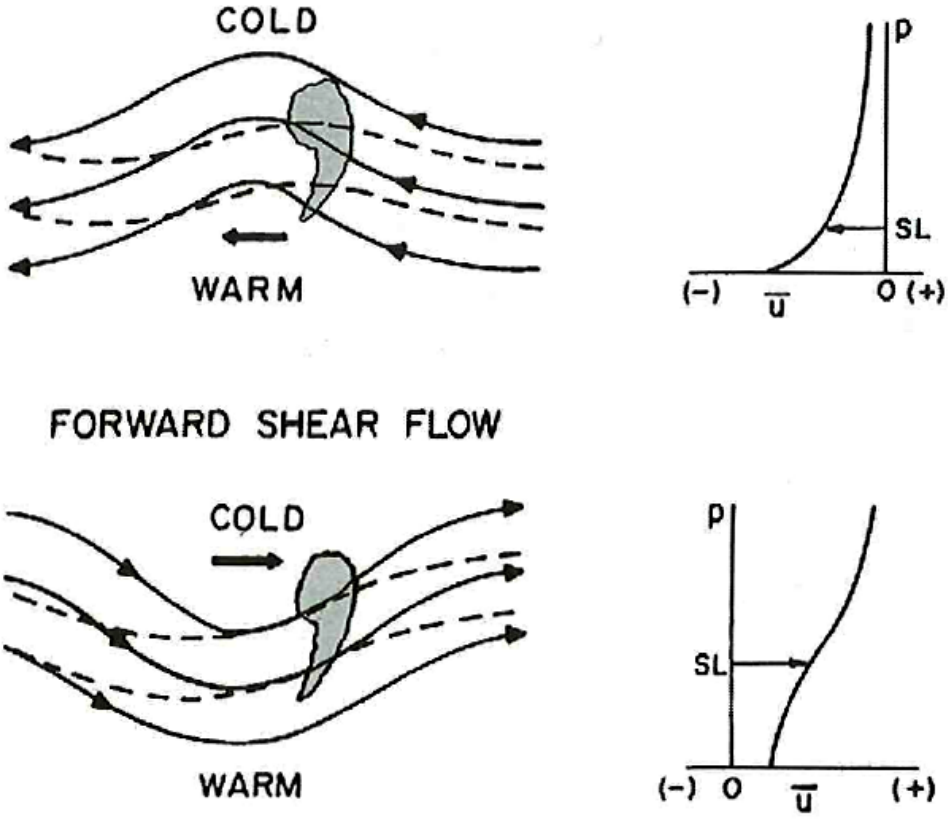

Figure 2.4: Comparison of the structure of disturbances in reverse-shear flow (above) and forward-shear flow (below). Solid lines show streamlines, broken lines isotherms at the steering level (SL) wind; stippling indicates the extent and position of an associated comma cloud (from Businger and Reed, 1989b, in Rasmussen and Turner (2003))

and Turner (2003)).

Kolstad (2006) identified reverse shear conditions as favorable for polar low development, and Blechschmidt (2008) studied 90 polar lows during a 2-year period and found that the reverse shear criteria were fulfilled for approximately 22 percent of the polar low events.

2.1.2 Thermal instability

Thermal or convective instability plays a major role in the development and growth of polar lows. In most significant polar lows there is a large amount of convective clouds associated with the low (Rasmussen and Turner (2003)). Thermal instability refers to the stability in the vertical direction, for instance if a parcel of air were lifted from one pressure level to another, would the

parcel descend, stay where it is, or continue to ascend by itself? As a parcel of moist air rises and becomes supersaturated, the moisture can condensate into droplets and latent heat will be released in the process. This heats up the parcel allowing it to rise even further, until the parcel and the environment have the same temperature and the parcel of air is no longer super-saturated.

Thermal instability has been known to be important both for development and growth of polar lows, since Dannevig wrote his paper on 'instability lows' in 1954. However, the precise way thermal instability affects the lows, and how important the contribution is, has been disputed over the years.
Føre et al. (2011) used bulk formulae to calculate the vertical surface fluxes of latent heat (LH) and sensible heat (SH). Here it is assumed (Hartmann, 1994) that the surface fluxes are proportional to the mean wind speed roughly at 10 m height (U_r):

$$SH = c_p \rho C_{DH} U_r (T_s - T_a(Z_r)) \tag{2.1}$$

$$LH = L \rho C_{DE} U_r (q_s - q_a(Z_r)) \tag{2.2}$$

In the bulk aerodynamic formulae, ρ (1.225 kg m^{-3}) is the air density, L is the latent heat of vaporization, c_p (1004 $m^{-2}s^{-2}K^{-1}$) is specific heat at constant pressure, and C_{DH} (1.14×10^{-3}) and C_{DE} (1.2×10^{-3}) are aerodynamic transfer coefficients for the temperature and humidity, respectively. T_s and q_s are the surface temperature and humidity, while T_a and q_a are the temperature and humidity at 10 m height, respectively. Equations 2.1 and 2.2 states that the temperature and humidity difference between the surface and the 10 m air, along with the 10 m wind speed, is proportional to the strength of the surface fluxes. During a MCAO where cold dry air is advected over a warm and moist ocean surface, the differences will be huge, and large fluxes will be generated.

Latent heat release can contribute to the intensification of a polar low through many mechanisms, and theories commonly used to explain hurricane growth can be used to explain the intensification of intensely convective polar lows. Two of the most used theories are conditional instability of the second kind (CISK), and wind-induced surface heat exchange (WISHE). These theories describe a positive feedback loop where a cyclone induces localised tropospheric heating associated with strong convection, which results in further intensification of the cyclone (Bracegirdle and Gray (2009)).

CISK

Conditional Instability of the Second Kind (CISK) was introduced by Ooyama (1964) and Charney and Eliassen (1964) in slightly different forms. Since then it has been modified and generalized. Ooyama (1982) describes it as a cooperative intensification involving organized moist convection and the cyclone-scale vortex (Craig and Gray (1996)).
In short, CISK describes how a cyclone can intensify itself. The cycle is shown in figure 2.5. A necessary condition for CISK is presence of a sufficient reservoir of Convective Available Potential Energy (CAPE), in the atmosphere, so that an air parcel which has been lifted to its level of free convection, will continue to ascend. First, radiation, surface fluxes or other forcing mechanisms destabilize the atmosphere, which starts vorticity in the friction layer. Then Ekman pumping starts convection. Latent heat is released and the air expands as it rises, pushing the air at the higher levels aside, inducing a divergence at the upper-level and a low-pressure at the lower levels. This again leads to convergence at the surface level, and produces more vorticity inducing more Ekman pumping. This cycle will repeat itself until some other factors, for instance if the cyclone makes landfall weakens it. The idea that deep convection is important to polar low as well as tropical cyclone development with CISK, was revived by Rasmussen (1977, 1979) and Økland (1977) (Rasmussen and Turner (2003)).
Linders and Saetra (2010) addressed the role of CISK in the two polar low events during the IPY-THORPEX Andøya field campaign and found that the reservoir of CAPE was virtually nonexistent, so that CISK is unlikely to be a major contributor to these cases.

WISHE

Wind-induced surface heat exchange (WISHE) instability was introduced by Emanuel (1986) as an alternative to CISK. Since CISK is dependent on sufficient CAPE in the nearby atmosphere, it did not explain the thermal intensification of polar lows when the atmosphere was almost convectively stable (Rasmussen and Turner (2003)). WISHE relates the tropospheric heating directly to fluxes of heat and moisture from the ocean to the atmosphere in an atmosphere that is nearly neutral to moist convection (Bracegirdle and Gray (2009)).
In the WISHE theory the surface fluxes of heat and moisture are of more importance than in CISK. Craig and Gray (1996) states: *Moist convection mixes air through the troposphere, but does not cause any temperature perturbation unless the boundary layer is anomalously heated as a result of surface fluxes of heat and moisture. The surface fluxes are wind speed dependent and, therefore determined by the vortex-scale flow.* A schematic of WISHE is shown in figure 2.6. The inflow at a forming low pressure system at lower

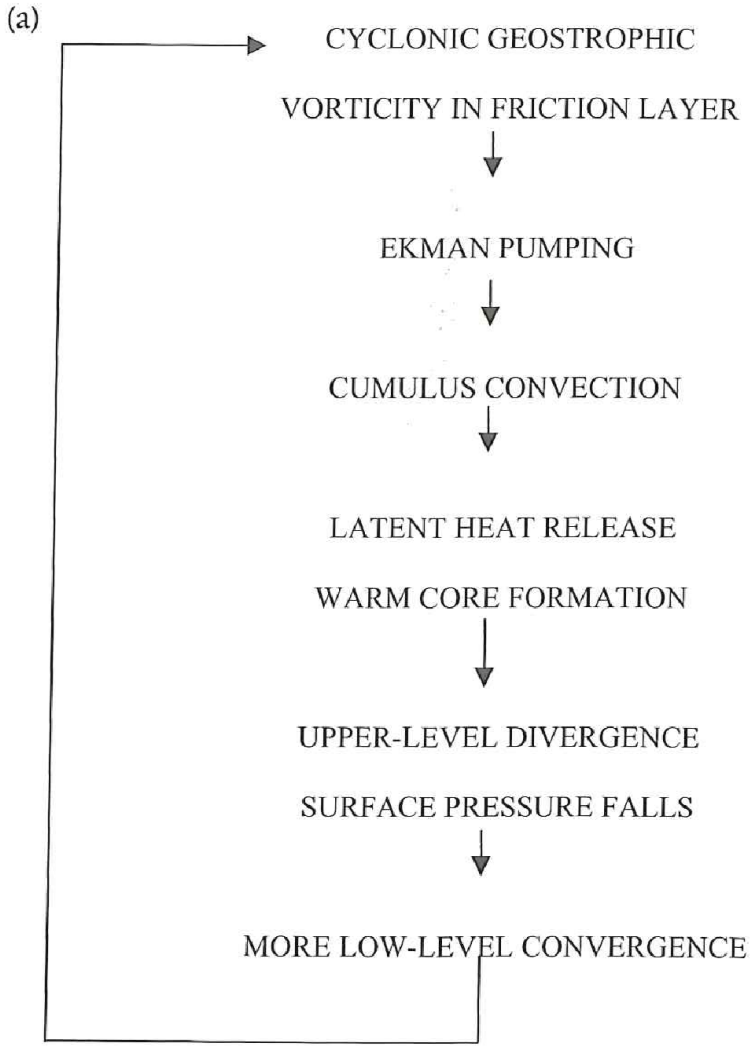

Figure 2.5: Schematic diagram of CISK. (From Bluestein, 1993, in Rasmussen and Turner (2003))

levels, will result in increased surface fluxes from the sea close to the low (Rasmussen and Turner (2003)). Latent and sensible heat are transported upwards by turbulence and convection. The energy source of the cyclone in this case is the surface fluxes, since there is little or no CAPE in the atmosphere.

Bracegirdle and Gray (2009) found that WISHE contributed to at least 18% of the amplitude of the mature surface polar low studied in their paper. They also stated that three points indicated dominance of WISHE during the polar lows mature stage. The first was weak baroclinic interaction between different PV anomalies, secondly that small values of CAPE were found in the vicinity of the polar low and thirdly the strong surface fluxes found within the polar low.

The CISK and WISHE theories are widely accepted as mechanisms that intensify polar lows, but have never been able to explain the initial develop-

ment from an infinitesimal disturbance to a polar low. This indicates that thermal instability in itself is not enough to produce a polar low, and that other factors must be present.

2.2 Upper-level forcing and potential vorticity (PV)

In many cases, polar low development is triggered by upper-level forcing by stratospheric air that is advected into the troposphere. An effective tool to recognise the stratospheric air is to consider the potential vorticity (PV) of the air. Figure 2.7 shows a tropopause folding event from USA. A jet stream is market by the "J". Beneath the stream is a layer characterized by very strong vertical wind shear and high temperature gradients. The PV values are much higher within this upper-level frontal zone, than that of typical air parcels at this level, which indicate intrusion of stratospheric air into the troposphere.

PV is conserved in an inviscid, adiabatic flow, a condition that is generally met in the lower stratosphere and higher troposphere. The quasi-geostrophic PV-equation described in Rasmussen and Turner (2003) is given by:

$$q_p = \nabla^2\psi + f + f_0^2 \frac{\delta}{\delta p}\left(\frac{1}{\sigma}\frac{\delta\psi}{\delta p}\right) \tag{2.3}$$

In equation 2.3, ψ is the streamfunction, f_0 is the constant Coriolis parameter at a specific standard latitude, f is the Coriolis parameter at the latitude of consideration, σ is a static stability parameter given by $\sigma \equiv -\frac{\alpha}{\theta}\frac{\delta\theta}{\delta p}$, where α is specific volume, θ is potential temperature and p is pressure. q_p is expressed by, from the left to right, the relative vorticity, planetary vorticity and stretching vorticity. As mentioned earlier potential vorticity is conserved on a θ-surface if diabatic and frictional effects are neglected. The result is the equation of conservation of potential vorticity in a geostrophic flow:

$$\frac{dq_p}{dt} \equiv \left(\frac{\delta}{\delta t} + \vec{v}_g \cdot \nabla_p\right) q_p = 0 \tag{2.4}$$

An example of how this works is given in Rasmussen and Turner (2003). As a column of air, confined between two isentropic surfaces moves into an area where the isentropic surfaces have wider separation, the column will be stretched. The upper part of the column will rise and cool, while the lower part descend and heat up adiabatically. In this case the stretching vorticity

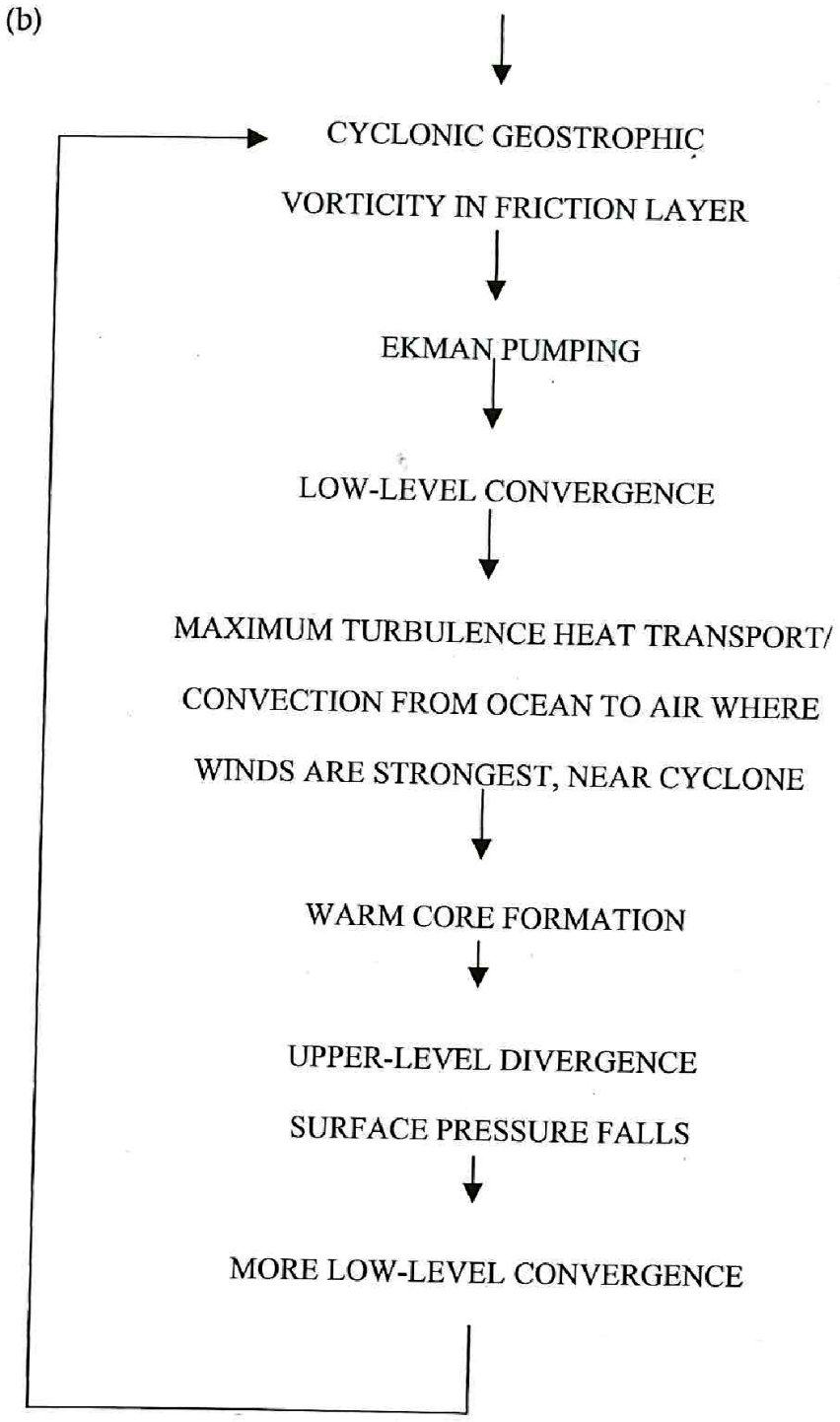

Figure 2.6: Schematic diagram of WISHE. (From Bluestein, 1993, in Rasmussen and Turner (2003))

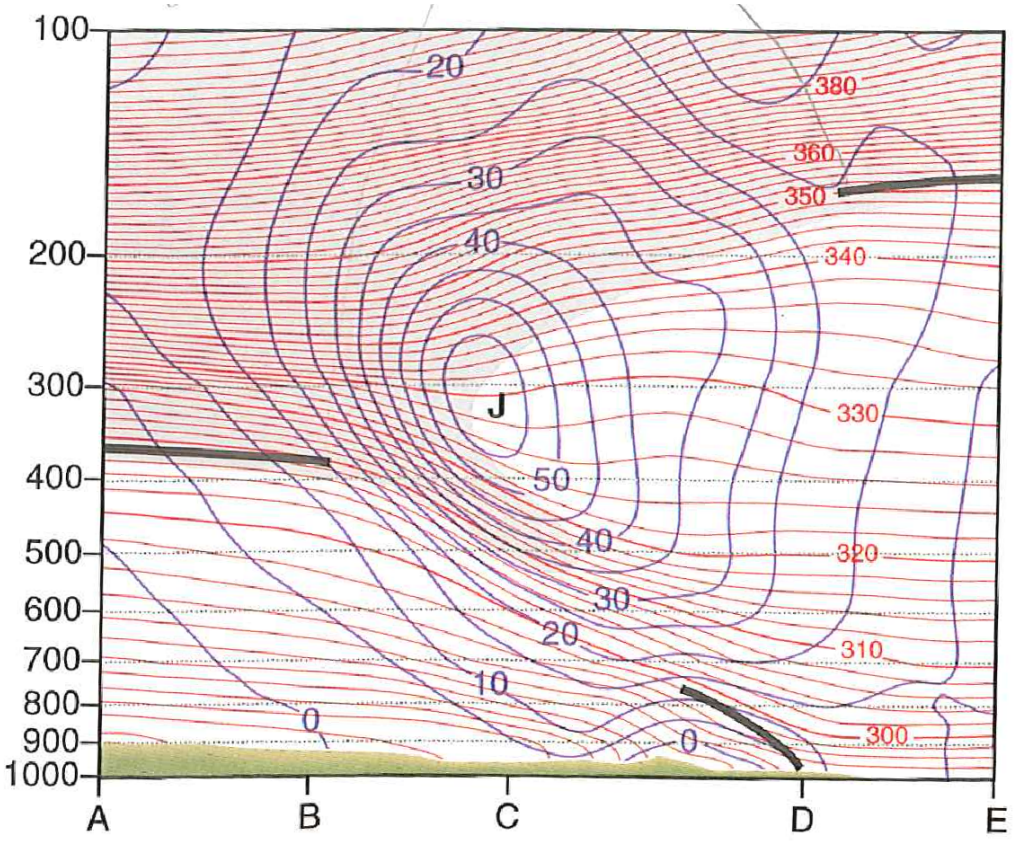

Figure 2.7: Vertical cross section of wind and potential temperature for 12 UTC Nov. 10, 1998. This section extends from North Platte, Nebraska to Jackson, Mississippi. Potential temperature is indicated by red contours, and isotachs of geostrophic wind speed normal to the section are plotted in blue with positive values defined as southwesterly winds directed into the section. The region in which isentropic potential vorticity exceeds $10^{-6} Km^2 s^{-1} kg^{-1}$ is indicated by shading. Heavy black lines represent the position of the surface-based fronts and tropopause. (Courtesy of Jennifer Adams, COLA/IGES) From Wallace and Hobbs (2006)

in equation 2.3 will become smaller, and the relative vorticity on the right hand side will have to increase in order to conserve PV, assuming that the changes in planetary vorticity are small. This is illustrated in figure 2.8.

Quasi-geostrophic PV is normally used on larger-scale flows, where diabatic heating and frictional forces can be neglected. However this is not the case for smaller scale phenomenon such as polar lows. It is therefore necessary to obtain an expression for PV that also accounts for diabatic heating and friction. Ertel potential vorticity is used for this purpose, $EPV \equiv q$ is given by:

$$q = \frac{1}{\rho}\left(\vec{\zeta}_a \cdot \nabla\theta\right) \tag{2.5}$$

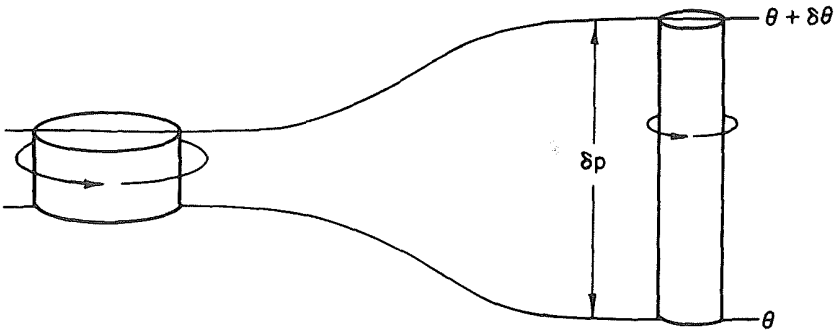

Figure 2.8: A cylindrical column of air moving adiabtically, conserving potential vorticity. (From Holton (2004).)

Here ρ is the density of air and $\vec{\zeta_a}$ the total vorticity. Change in q due to diabatic heating and friction is expressed by the following relation:

$$\frac{dq}{dt} = \frac{1}{\rho}\left(\vec{\zeta_a} \cdot \nabla\dot{\theta}\right) + \frac{1}{\rho}\left(\nabla \times \vec{F} \cdot \nabla\theta\right) \tag{2.6}$$

$\dot{\theta}$ denotes diabatic heating and $\vec{F}$ is the friction force. Equation 2.6 states that if the gradient of a diabatic heating has a component in the direction of the total vorticity vector, there will be a decrease in PV above the level of the diabatic heating maximum, and a similar increase of diabatic heating below. From this it is possible to conclude that an upper negative PV anomaly and a lower positive PV anomaly tends to develop due to diabatic heating. A clockwise circulation associated with the upper-level negative PV anomaly, may counteract and delay an advancing upper-level positive PV anomaly, and thereby contribute to a prolonged deepening phase of the cyclone, as Føre et al. (2011) found in their study of the March 3-4 2008 polar low.
The friction term in equation 2.6 contributes normally to a decrease in PV, but in regions where the low-level wind has a component directed in the opposite direction of the thermal wind (warm-front) the friction will tend to increase the low-level PV.
The expression for EPV can also be written in a slightly simpler way by introducing isentropic coordinates in relation 2.5 for q. This gives the relation for isentropic potential vorticity:

$$q = (\zeta_0 + f)\left(-g\frac{\delta\theta}{\delta p}\right) \tag{2.7}$$

where ζ_0 is the relative vorticity on an isentropic surface. q is usually expressed in PV units defined by $q = 10^{-6}m^2s^{-1}Kkg^{-1} \equiv 1PVU$.
As mentioned earlier the conservation of PV in an inviscid, adiabatic flow

has important implications. For instance that the conservation of PV can be seen in an exchange of air between the stratosphere and troposphere. If a column of air is advected from the relatively static stable stratosphere to the less stable troposphere $-g\frac{\delta\theta}{\delta p}$ will decrease in equation 2.7 and the relative vorticity will increase to compensate this. Therefore stratospheric air that has been advected into the troposphere has higher PV than its surroundings. The increased vorticity can contribute to cyclogenesis. When cyclogenesis occurs, the diabatic and frictional effects become essential. The effect of diabatic heating from condensation within a polar low can be seen in the PV-fields at the lower level as the heating will give a positive PV-anomaly.

2.2.1 The Invertibility principle

One essential aspect of considering PV is the invertibility principle that provides the streamfunction and geopotential height field. From this it is possible to obtain the wind and temperature fields, given a PV anomaly and suitable balance and boundary conditions. If the PV is larger than the reference PV, there is a negative streamfunction or negative geopotential, and vice versa.
The invertibility principle of PV can be used to measure the contribution of a PV anomaly to the flow and its interaction to other anomalies. Bracegirdle and Gray (2009) used piecewise PV inversion to study the dynamics of a polar low event that occurred over the Norwegian Sea on October 13 1993. The methodology used, consisted of performing two inversions to quantify the instantaneous wind and temperature distribution attributable to a PV anomaly of interest. One inversion of the full PV field was performed, as well as an inversion of the PV field with the anomaly removed. The difference of the unmodified and modified inverted fields gave a measure of the contribution of the anomaly to the flow and its interaction with other anomalies.
Bracegirdle and Gray (2009) identified the polar low as a type C cyclone, with three clear stages of development. The first stage was an initial baroclinic stage dominated by the arrival of an upper-level PV anomaly over a low-level baroclinic zone, the second stage a baroclinic stage with strong heat release and maintenance of a vertical tilt of the geopotential height perturbation, and the third stage was a non-baroclinic WISHE stage that occurred as a deep warm core formed.
Wu et al. (2011) also used this method to diagnose the development of a polar low over the Sea of Japan in December 2003. They suggested that the polar low was initiated as a result of the combined effect of a positive PV anomaly near the tropopause and a near-surface positive temperature anomaly induced by the upper-level positive PV anomaly.

2.2.2 Static stability in the lower layers

For upper-level disturbances to penetrate great vertical distances, the static stability of the lower layers must be low. Kolstad (2006) investigated in the 925-700hPa layer. The Rossby radius of deformation is defined in Holton (2004) as:

$$L_R \equiv NH/f_0 \tag{2.8}$$

where f_0 is the Coriolis parameter, H is the height of the tropopause and N is the Brunt-Väisällä frequency. Small values of N allow upper-level disturbances to penetrate greater vertical distances. To evaluate the lower-level static stability, a dimensionless normalized radius of deformation defined as:

$$R_N \equiv L_R/H = N/f_0 \tag{2.9}$$

is used. Kolstad (2006) calculated N for the 700-925hPa layer as the real part of

$$N = \sqrt{g\frac{\Delta(\ln\theta)}{\Delta z}}. \tag{2.10}$$

When R_N is small (Kolstad (2006) used 80 as an upper-level value in his study) the static stability is low, and conditions for polar low development are favorable.

2.3 Structure of mature polar lows

It is often seen that polar lows develop as a mainly baroclinic-driven comma shaped low, and later take on convective characteristics as spirali formed low (Bracegirdle and Gray (2008)). As baroclinicity tends to be the most effective forcing at the early developing stage, convective and thermal effects is commonly the main forcing mechanisms for intensifying and maintaining the polar low. The release of latent heat becomes very intense in some polar lows, leading to the formation of a warm core. A warm core normally extends through most of the troposphere, and is characterized by warm ascending air with surrounding clouds, with cyclonic in-flow at the surface layer, and anti-cyclonic out-flow at the upper level (Rasmussen and Turner (2003)). In satellite images this is often seen as the characteristic “eye” of the low. The structure of the polar low from March 3-4 has been investigated in at least

two papers (Føre et al. (2011) and Wagner et al. (2011)).

The polar low event on March 3-4 is described by Føre et al. (2011). The study was based on dropsonde data from three flights, the first from prior to cyclogenesis, second from the developing state, and the third from the mature stage of the low. Vertical cross-sections were made from the dropsonde data and figure 2.9 shows the equivalent potential temperature (upper panel), relative humidity (middle panel) and wind (lower panel) from the cross section taken from the core at mature stage on March 4.
The results showed a clear warm core with a characteristic "eye" in the center of the cyclone during the mature stage. The warm core had 3 K higher potential temperature than the cold air outbreak southwest of the core. It could also been seen that there were two columns of air with very different relative humidity (RH), within the core, one with RH up to 60% at 500hPa-level and another with RH down to 20% at 700hPa-level. Føre et al. (2011) links this with a similar downfolding of the potential temperature surfaces, and suggest that there was an intrusion of dry stratospheric air, that probably contributed to the early development of the low, and also for surface development in the later stages.
There was also a sharp inversion found just below the 800hPa-level southwest of the low, and satellite images showed shallow stratiformed clouds in this region indicating a cold air outbreak. The convective towers near the center of the cyclone reached up to the tropopause. Maximum wind speed could be found between 700 and 900hPa in a low-level jet on the southwestern part of the center of the cyclone, and were measured to be around 26-28 m/s. The highest fluxes were found west of the center, and were estimated to be around 300 W m^{-2} for latent heat, and 280 W m^{-2} for sensible heat, suggesting considerable contribution of condensational heating.

Wagner et al. (2011) wrote another paper regarding the same polar low event, where the structure of the low was investigated using lidar measurements and model simulations with WRF. The lidar data gives vertical cross-section with a lot better resolution than the dropsondes. A disadvantage with this method is that the lidar has difficulties when it comes to penetrate clouds. However, it was possible to identify mesoscale structures such as shallow convection in a cold-air outbreak, a dry intrusion in the "eye" and deep convection around the center.
The core of the cyclone was investigated with particular emphasis. It was an area of 100-150km characterized by an almost symmetrical V-shaped intrusion of dry upper-level air and calm winds. Equivalent potential temperature contour lines were downward-bending at the center, indicating a warm core. The core area was not cloud-free as often seen in tropical cyclones, but had some low-level clouds. At the edges the core was surrounded by moister air masses north and south, with higher convective clouds in the north. However

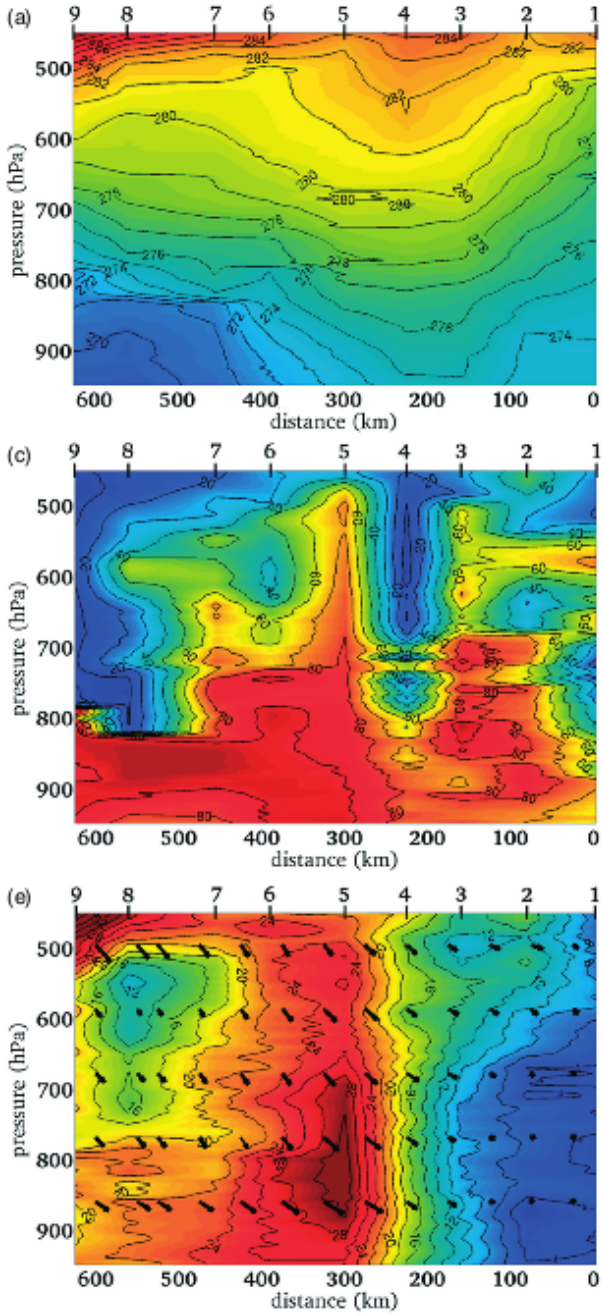

Figure 2.9: The upper panel show potential temperature (K), middle panel relative humidity (%) and the bottom panel wind speed (ms^{-1}) from a cross section taken of the core structure of the 3-4 March 2008 polar low taken on March 4. From Føre et al. (2011).

the convective clouds did not form a closed ring around the core. Simulation showed a spiral band of dry air along a dry surface ridge with origin at the eastern side. Horizontal wind speed was observed to be 5 m/s in the lower levels at the center, and increased radially outwards to 20 m/s in the north. Results from the model simulation showed that the polar low was significantly weaker when the effects from the surface fluxes were turned off. Wagner et al. (2011) concluded that the main energy source for maintaining the polar low was surface fluxes.

Chapter 3

Methods

Observations from the Andøya field campaign and operational model analyses are used for the analysis of the March 16-17 polar low in chapter 4. A summary on how the observations were obtained, along with a description of the WRF model and the setup used for the simulations of the polar low, is also given.

3.1 Observations

As part of the international IPY-THORPEX[1]-project, which took aim at improving forecasting for adverse weather in the arctic region, several field campaigns were launched. The Andøya field campaign lasted from February 25 to March 17 in 2008, and the project leader was Jón Egill Kristjánsson from the University of Oslo. An extensive description of the campaign is given in Kristjánsson et al. (2011).
The objective was to investigate polar lows and other arctic weather phenomena to improve the weather forecasts for ships and coastal interests. Researchers from the Norwegian meteorological institute, the Bjerknes center, the universities of Bergen and Oslo along with international researchers from various countries, were situated at the base at Andøya Rocket Range during the campaign. The most important tool for gathering in-situ data from the polar lows was the DLR Falcon research aircraft from the German aerospace center.

The aircraft measured air pressure, temperature, humidity and wind speed including turbulence. All the measurements were made at least each second

[1]International Polar Year- The Observing System Research and Predictability Experiment.

to get all the variations right. There were also two LIDARs (Light Detection and Ranging) on board, one for wind speed and one for humidity. In addition to this, the aircraft launched dropsondes for gathering vertical profiles of the atmosphere during the flights. 150 dropsondes were launched during twelve flights that lasted for a total of 55 hours (Kristjánsson et al. (2011)). All the retrieved dropsonde observations were transmitted onto the Global Telecommunication System (GTS), so the observations were added to the operational model analysis at the time. The missions were mostly flown at an altitude of 8 km, which is a suitable altitude for both LIDAR and dropsonde profiling.

Two drones from the university of Braunschweig in Germany, and from Norut in Tromsø were also used in this mission. These light airplanes weighing only 30 kg and 580g, are equipped to measure air temperature, pressure, humidity, and the sea surface temperature. The range of the drones is about 300 km. In addition, the Norwegian coast guard was aiding the mission with the two ships KV Svalbard and KV Senja. Normally, ships would not be a good way to measure polar lows directly, as they are too slow to direct into the lows, but they can aid in other ways with radar, weather balloons etc., providing data of the atmospheric conditions around the spot where they are stationed. IPY-THORPEX researchers were on board both of these vessels, sending up radiosondes to measure temperature, air pressure, humidity and wind velocity. Weather balloons were also released from scientists over Novaja Semlja, Franz Josefs land, Murmansk, Ny-Ålesund, and Bjørnøya. Finally, drifting buoys from the integrated Arctic Ocean Observing System (iAOOS) supplied the campaign with observations of sea-level pressure and near-surface winds (Kristjánsson et al. (2011)).

3.2 The WRF model

To investigate the polar low in this study, the weather research and forecasting (WRF) model version 3.2 was used. It is a mesoscale numerical weather prediction (NWP) system designed both for operational forecasting as well as for research applications. The model is developed as a collaboration between several agencies, principally the National Center for Atmospheric Research (NCAR) which is operated by the University Corporation for Atmospheric Research (UCAR), the National Oceanic and Atmospheric Administration (NOAA),the National Centers for Environmental Prediction (NCEP) and the Forecast Systems Laboratory (FSL), the Air Force Weather Agency (AFWA), the Naval Research Laboratory, the University of Oklahoma, and the Federal Aviation Administration (FAA) (Skamarock et al. (2008)). It can be used on a large spectrum of applications from thousands of kilometers down to a few kilometers. WRF currently supports two different dynamical solvers, Advanced Research WRF (ARW) and the non-hydrostatic mesoscale model

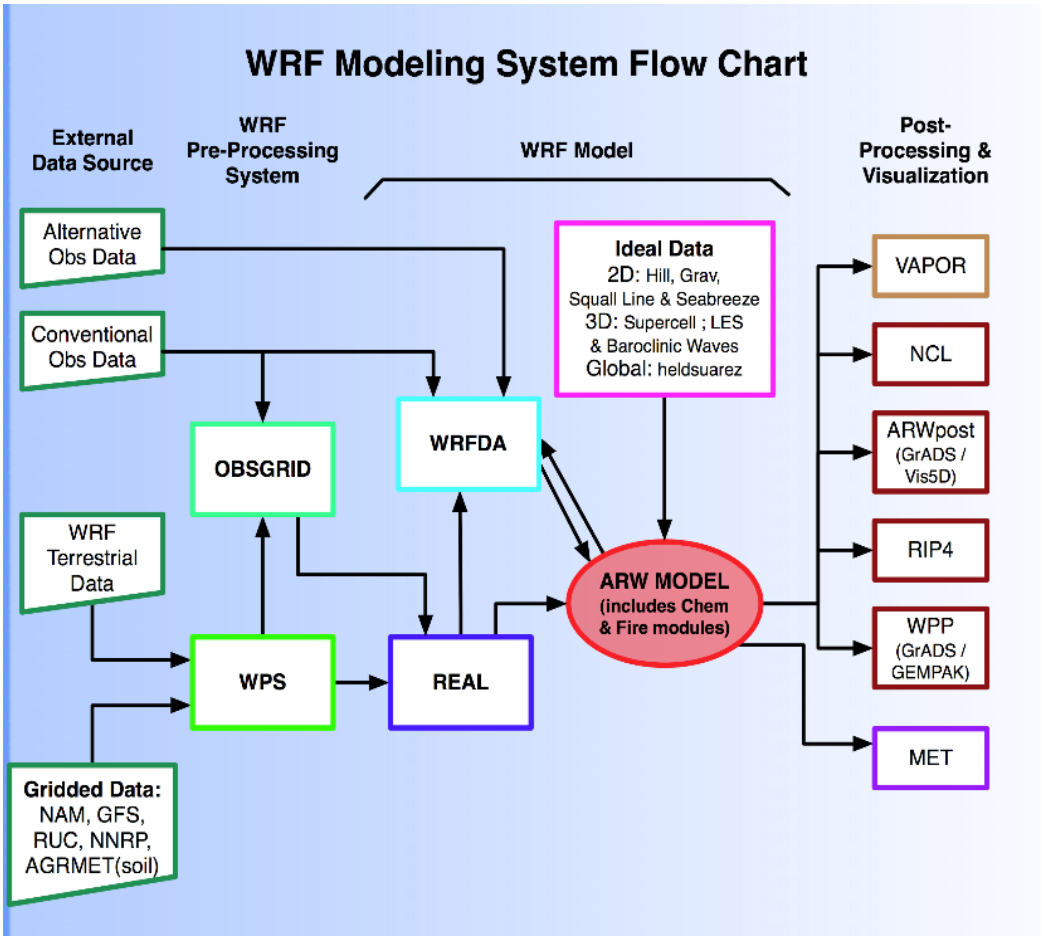

Figure 3.1: A flow chart of the various components in WRF. From the WRF users page: http://www.mmm.ucar.edu/wrf/users/model.html (UCAR)

(NMM). The ARW-solver is the default solver and is used in this study. It contains an equation set which is fully compressible, Eulerian and non-hydrostatic with a run-time hydrostatic option. Other main components of WRF are the WRF Pre-Processing System (WPS) and WRF variation data assimilation (WRF-Var) (Hodnebrog (2008)). Figure 3.1 shows a more detailed outline of the various ARW-components. The model can be run with both idealized and real-time input data, generated by the programs Ideal.F and real_em.F, which also generate boundary conditions files if necessary. WRF supports several physics schemes, two-way, one-way and two-way moving nests, analysis and observation nudging. Domain and landscape information and input is processed and generated by the WPS. It also takes real-time data analyses/forecasts from other models, and interpolates the data to the WRF grid. The purpose of WRF-Var is to assimilate observations into the model initial conditions.

3.2.1 WRF dynamics and numerics

Atmospheric flow solvers produce spatial and temporal integrations of the Euler equations, and accurate solutions for time-evolving flows are of utmost importance for NWP and most research applications (Skamarock and Klemp (2007)). The modes of meteorological interest are relatively slow. Fast modes in the solutions are the acoustic modes and contain no significant energy or amplitude relative to the meteorological modes. However, these acoustic modes inflict a significant restriction to the explicit time-integration methods, because a time step too large to capture the sound waves will cause numerical instability. Various ways of filtering the acoustic modes have been tested out in the past decades, but they always have drawbacks. In ARW, time-splitting methods are applied to solve the full Euler equations. The methods involve integrating terms associated with the acoustic modes with smaller time steps than those associated with the meteorologically significant modes. Most of the simplicity of fully-explicit solvers is maintained with these methods, and they have also proved more efficient than semi-implicit methods for limited-area NWP applications, where maximum Mach numbers of the modes in question do not exceed 1/3. High-order time and space discretizations can also be easily implemented within the splitting method (Skamarock and Klemp (2007)). The time-splitting methods also have some drawbacks. For instance that they are explicit and therefore also Courant-number limited. This implies that their ideal use is in limited area NWP, with a grid that is relatively isotropic. In other words, that the domains cover a smaller portion of the globe and are situated away from the poles and the problems associated with converging longitude lines that would impose severe restrictions on the time steps. However, starting with the ARWV3 release, WRF now support anisotropic projections, and with it the full latitude-longitude global model (Skamarock et al. (2008)). Semi-implicit methods can also be more efficient than time-splitting methods on modes with very low Mach-numbers.

Continuous Equations

The continuous equations solved in the ARW model are the Euler equations cast in a flux (conservative) form (Skamarock and Klemp (2007)). Here, the vertical coordinate, η, is defined by a normalized hydrostatic pressure (or mass) following Laprise:

$$\eta = \frac{(p_h - p_{ht})}{\mu} \text{ where } \mu = p_{hs} - p_{ht} \tag{3.1}$$

Here p_h is the hydrostatic component of the pressure, and p_{hs} and p_{ht} are the values for the dry atmosphere at the surface and top boundaries, respectively.

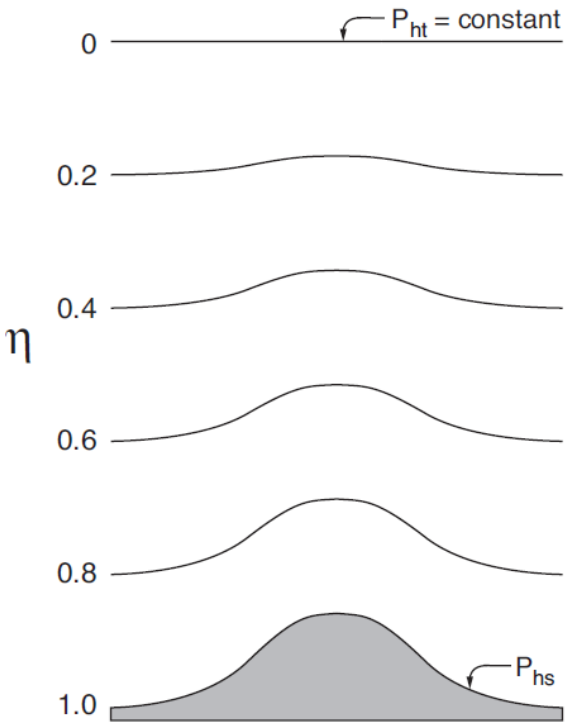

Figure 3.2: Schematic of the terrain following η coordinate. From Skamarock and Klemp (2007)

It is common practice to set p_{ht} = constant. η decreases monotonically from a value of 1 at the surface to 0 at the top of the domain, as shown in figure 3.2.

Using this vertical coordinate, the flux form equations are expressed as:

$$U_t + (\nabla \cdot \mathbf{V}u) + P_x\,(p, \phi) = F_U \tag{3.2}$$

$$V_t + (\nabla \cdot \mathbf{V}v) + P_y\,(p, \phi) = F_V \tag{3.3}$$

$$W_t + (\nabla \cdot \mathbf{V}w) + P_\eta\,(p, \phi) = F_W \tag{3.4}$$

$$\Theta_t + (\nabla \cdot \mathbf{V}\theta) = F_\Theta \tag{3.5}$$

$$\mu_t + (\nabla \cdot \mathbf{V}) = 0 \tag{3.6}$$

$$\phi_t + \mu^{-1} \left[(\mathbf{V} \cdot \nabla \phi) - gW \right] = 0 \tag{3.7}$$

$$(Q_m)_t + (\nabla \cdot \mathbf{V} Q_m) = F_{Q_m} \tag{3.8}$$

where $\mu(x, y)$ represents the mass of the dry air per unit area within the column in the model domain at (x, y), hence the flux form variables are defined as:

$U = \mu u/m, V = \mu v/m, W = \mu w/m, \Omega = \mu \dot{\eta}/m$

m is a map-scale factor that allows mapping of the equations to the sphere and is given by

$m = \frac{(\Delta x, \Delta y)}{\text{distance on the earth}}$.

$V = (u, v, w)$ are the physical velocities in the two horizontal and vertical directions, respectively, $\omega = \dot{\eta}$ is the transformed 'vertical' velocity, and θ is the potential temperature. $Q_m = \mu q_m; Q_m = Q_v, Q_c, Q_i, \ldots$, represent the mass of water vapor, cloud, rain, etc., and q_* are their mixing ratios. $\phi = gz$ (geopotential), p (pressure) and $\alpha = \frac{1}{\rho}$ (specific volume) are non-conserved variables that appear in the governing equations. α_d is the specific volume of dry air, whereas α refers to the specific volume including all moist species. To close the system, a diagnostic relation for the specific volume (the hydrostatic relation for dry air)

$$\phi_{eta} = -\alpha_d \mu, \tag{3.9}$$

and the moist equation of state

$$p = p_0 \left(\frac{R_d \theta \left(1 + \left(R_d/R_v\right) q_v\right)}{p_0 \alpha_d} \right)^{\gamma}, \tag{3.10}$$

are applied. Here $\gamma = c_p/c_v = 1.4$ is the ratio of the heat capacities for dry air, R_d is the gas constant for dry air, and p_0 is a reference pressure. x, y, η and t denote partial differentiation, and

$\nabla \cdot \mathbf{V} a = m^2 \left[(Ua)_x + (Va)_y \right] + (\Omega a)_\eta,$
$\mathbf{V} \cdot \nabla a = m^2 \left[U a_x + V a_y \right] + m \Omega a_\eta,$

where a represents a generic scalar variable. The pressure gradient terms in 3.2-3.4 are given by

$$P_x(p,\phi) = \left(\frac{\alpha}{\alpha_d}\right)\left[-\delta_x\left(p\phi_\eta\right) + \delta_\eta\left(p\phi_x\right)\right]$$
$$P_y(p,\phi) = \left(\frac{\alpha}{\alpha_d}\right)\left[-\delta_y\left(p\phi_\eta\right) + \delta_\eta\left(p\phi_y\right)\right]$$
$$P_\eta(p,\phi) = -gm^{-1}\left[\left(\frac{\alpha}{\alpha_d}\right)p_\eta - \mu\right].$$

The right hand side terms F_U, F_V, F_W, F_Θ and F_{Q_m} represent forcing terms arising from model physics, turbulent mixing, spherical projections, the earth's rotation and moist physics. All the prognostic equations 3.2-3.8 are cast in conservative form except for 3.7 since this is the material derivative of the definition of the geopotential and $\mu\phi$ is not a conserved quantity.
When solving these equations, a perturbation formulation is used. The atmosphere is strongly stratified and is in approximately hydrostatic balance, it is therefore useful to recast the thermodynamical variables into a reference profile plus a perturbation, where the reference profile is in hydrostatic balance. This is done to reduce truncation errors in the horizontal pressure gradient calculation in the discrete solver and also the machine rounding errors in the vertical pressure gradient and buoyancy calculations.
In the ARW model an original third-order Runge-Kutta (RK3) type scheme is used as the basis for the time-split scheme. It is not a standard Runge-Kutta scheme in itself, because it is third-order accurate for linear equations, but only second-order for non-linear equations. Skamarock and Klemp (2007) state however, that this scheme is more easily adaptable for stable time-splitting than other Runge-Kutta variants. The RK3 also avoids problems that afflict other common NWP-schemes such as the leapfrog scheme.
The spatial discretization for the ARW model is performed on a staggered C-grid, and is commonly used in non-hydrostatic NWP models, since it provides the most accurate representations of gravity waves. An illustration of the grid is shown in figure 3.3. The C-grid staggering allows for a discretization of the pressure gradient and divergence term across a single grid interval without any averaging, achieving a highly accurate second-order difference. The timestep constraint associated with a one-grid-interval gradient operator is relaxed by a factor of 2 with the use of an explicit forward-backward acoustic-mode integration.

3.2.2 Nesting

A nested run contains one or more smaller domains within a larger domain. It can be embedded simultaneously inside a coarser-resolution model run,

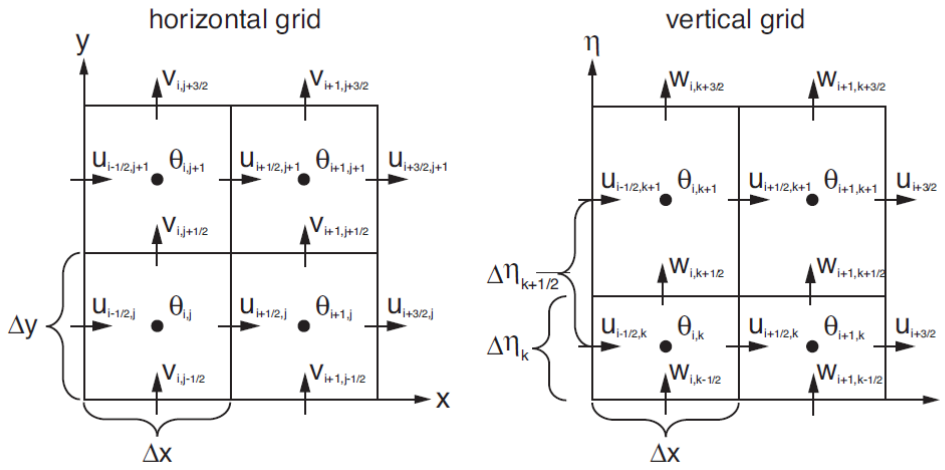

Figure 3.3: Horizontal (left) and vertical (right) staggering for the C-grid. From Skamarock and Klemp (2007).

or independently as a separate model run. The nest or child domain covers a portion of the parent domain, which also provides its lateral boundary conditions (Gill and Pyle (2008)). There can be several nested domains within a parent domain, both inside other nested domains and also several domains with the same parent domain, but a child domain can not have more than one parent domain. The advantages of using nested domains include the possibility of running a high-resolution model within a minor domain at a significantly lower computational cost, than running a uniformly high resolution model over a larger domain. Nested domains also avoid the problem of having mismatched time and lateral boundary conditions in a very small domain, since the parent domain will provide the boundary conditions. Another advantage of the nesting technique in ARW is the efficiency when doing nested simulations on parallel computer systems, and the support for moving nested grids (Hodnebrog (2008)). There are two options of nesting in ARW, one way nesting and two way nesting. In one way nesting, information from the parent domain is used to produce boundary conditions for the finer grid before the latter is integrated, there is no feedback from the child domain. However, in two way nesting, the solution from the child domain replaces the values in the coarser grid for those points that are inside the child domain.

3.2.3 WRF setup

The main goal of the model simulations was to be able to predict and simulate the March 16-17 polar low better than the operational forecast done by the HIRLAM model, and also the simulation with the UM for the same polar low described by McInnes et al. (2011). Three key features have been

varied and tested out in the WRF-simulations, the initial time, horizontal resolution and physics options. The focus on how well the different model runs performed has been whether a low was actually produced, if so, where did it develop? Finally the movement and the strength of the low, will be addressed.

The namelist in the WRF-program contains the choices of schemes used to parametrize different physical processes that cannot easily be resolved in the WRF-simulations. For instance, convective clouds are not resolved in domains with horizontal resolution less than 5km. The initial choices for physics schemes are given here. For domains with lower resolution than 5km, Grell 3D ensemble cumulus scheme was utilized. Mellor-Yamada-Janjic TKE scheme was used as boundary-layer option, as microphysics option the Purdue Lin et al. scheme was used. This scheme is a 5-class microphysics scheme that also contains graupel, ice sedimentation and timesplit fall terms (Dudhia). The RRTM and Goddard scheme were used for longwave and shortwave radiation, respectively. Monin-Obukhov (Janjic) scheme was chosen as surface-layer option and Unified Noah land-surface model was chosen as land-surface physics option.

3.2.4 Domain setup

In this study a large parent domain with a horizontal grid spacing of 30km and a smaller child domain with a grid spacing of 10km was used. Figure 3.4(a) show the horizontal extent of the two domains. Two-way nesting was turned on. The parent domain covers most of Scandinavia, the Norwegian Sea and Svalbard, and the child domain was designed to mainly capture the developing stage of the low and cover the coast of Nordland and Troms in Norway, in addition to the Norwegian Sea outside the coast and up to the tip of Spitsbergen, Svalbard. This domain does not cover the whole trajectory of the polar low, so at the time when the low makes landfall it is not visible here. The center of the parent domain was set to 70°N and 10°E, approximately where the polar low is situated in the March 16 1200 UTC satellite image.

Meteorological data from ECMWFs[2] global model was used as initial conditions to WRF. These data have a grid spacing of $0.25° \times 0.25°$ and contain analysed fields for every 6th hour, including SST and sea ice. Geogrid data from the WRF users site, including MODIS[3] were used for the land and terrain input.

[2]European Center for Medium-Range Weather Forecast
[3]Moderate Resolution Imaging Spectrometer

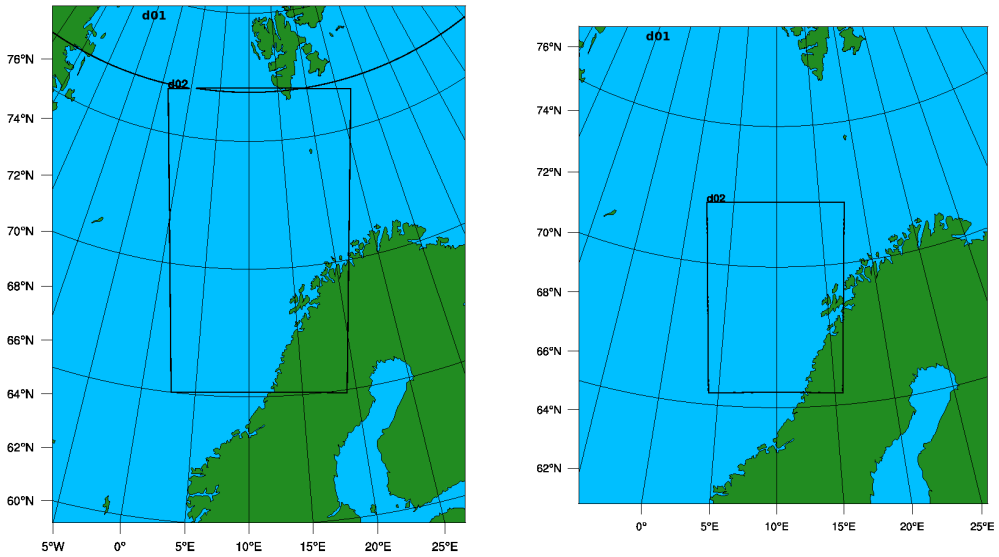

(a) (b)

Figure 3.4: Parent (d01) and child (d02) domains for a) the original WRF simulations, and b) the high resolution WRF simulations.

3.2.5 Simulations

The simulations were divided into three main groups of experiments.

The first set of simulations focused on the importance of the initialization time. McInnes et al. (2011) found in their study that the initial conditions were important for the model performance, especially for the high resolution runs. Minor changes in the initial time (only 1-2 hours) gave few differences between the simulations, but when starting 24 hours apart, the differences were huge for the high resolution runs. They found that starting the model 24 hours later dramatically reduced the performance for the high resolution runs. It was suggested that this could indicate the high resolution runs needed to be initialized at a relatively early stage in order to create their own dynamics during the pre-conditioning of the low. The time it takes to do this is called model spin-up time.

In this study the reference time (RT) was set to 0000 UTC on March 16 when the polar low started to develop. Simulations starting from -72h 0000 UTC on March 13, -36h, -24h, -12h, -6h, +0h, +12h and +24h (the last two to model the trajectory and the strength of the low) were carried out. These simulations were divided into three subsets of simulations. Long lead-time

(72-24 hours in advance of RT), short lead-time (24-0 hours in advance of RT) and post-cyclogenesis (12-24 hours after RT) initialization.

Set number two of model runs emphasised the horizontal resolution. Both McInnes et al. (2011) and Yanase et al. (2002) found that high resolution models managed to reproduce the structure and movements of polar lows successfully. McInnes et al. (2011) found that by lowering the grid spacing from 12km to 4km gave considerable benefits with the UM model, and concluded that this was mainly due to cumulus handling.
Two new domains were made, this time with a parent domain with grid spacing of 9km and a child domain with 3km grid spacing, the integration time step was reduced to 40 sec for the outer domain. The new domains are smaller than the original ones, but still cover the area of interest, as seen in figure 3.4(b). Given that the new domain must have a lot more grid boxes to cover this area, the computation time increased. Model runs were initialized at 0h and -24h, to see if the initial time would impact the performances of the high resolution runs more than the coarse resolution runs, as suggested by McInnes et al. (2011).

The third and last set of simulations was carried out with different options of parametrisation schemes for bulk microphysics, cumulus clouds and planetary boundary layer (PBL). As both microphysics and cumulus clouds parametrisation contribute to condensation, and theories presented in chapter 2 suggest an important role of diabatic heating, it will be interesting to study how different schemes impact on the simulations. The PBL schemes control the turbulent fluxes in the whole atmospheric column, not just the boundary layer, and is responsible for the transport of heat and moisture from the surface layer to the rest of the atmosphere. PBL may therefore also impact on the model's ability to simulate polar lows.

Original domains were used, and the model runs were initialized at -24h (0000 UTC March 15). Only one parametrisation scheme was changed in each experiment. For the microphysics experiment the Purdue Lin scheme was changed into the WRF Single-Moment 6-class (WSM6) scheme. Microphysics includes explicitly resolved water vapor, cloud, and precipitation processes Skamarock et al. (2008). Both schemes contain six classes of hydrometeors: water vapor, cloud water, rain, cloud ice, snow and graupel. A major difference from Purdue Lin to WSM6 is that a diagnostic relation based on ice mass content rather than temperature, is used for ice number concentrations. Wu and Petty (2010) studied the intercomparison of bulk microphysics schemes in model simulations of polar lows, and concluded that the WSM6 scheme appeared to reproduce the cloud and precipitation processes most realistically. However, the different schemes did not appear to

change the positions of the polar lows.

For the cumulus scheme experiment the Kain-Fritsch scheme was used. As the Grell-3 scheme was introduced in WRF version 3, it has not been tested out as extensively as the other cumulus schemes. The Kain-Fritsch scheme however, is common for polar low simulation, and has recently been used by Wu et al. (2011) and Wagner et al. (2011). It makes use of a relatively simple cloud model with moist updrafts and downdrafts, including the effects of detrainment, entrainment, and relatively simple microphysics. There are no studies on comparison between the performance of the different cumulus parametrisation schemes of polar low simulation in particular, but a study made by Wang and Seaman (1996) concluded that the convective available potential energy-based Kain-Fritsch scheme performed better overall in the six different precipitation cases studied. The Grell-3 scheme is based on an ensemble mean approach, where multiple cumulus schemes and variants are run within each grid box and then the results are averaged and to give feedback to the model Skamarock et al. (2008). It is distinguished from other cumulus schemes by allowing subsidence effects to be spread to neighboring grid columns, making the method more suitable to grid spacings less than 10 km, while it can also be used at larger grid sizes where subsidence occurs within the same grid column as the updraft.

Finally, the Mellor-Yamada-Janjic (MYJ) scheme was changed to the Mellor-Yamada-Nakanishi-Niino (MYNN), which is an improved version of the prior scheme. Both schemes are based on the Mellor-Yamada Level 2.5 turbulence closure model (Mellor and Yamada, 1982), and utilize the same form of the turbulent kinetic energy (TKE) equation. They differ in their formulations of mixing length scales, l_m, and were tuned to different data sets: The MYJ was tuned to observations while the MYNN was turned to large eddy simulations (LES). A potential advantage of the latter is that LES provide a whole range of turbulence statistics throughout the entire PBL under controllable conditions (Olson and Brown). There are not many studies that have addressed the role of PBL schemes in polar low simulations, but as the turbulent fluxes of heat and moisture are important in polar low theory, it is interesting to address this question.

Configuration	Initialization	Grid spacing domain 1, domain 2	Comment
WRF1300	0000 UTC March 13	30km, 10km	
WRF1412	1200 UTC March 14	30km, 10km	
WRF1500	0000 UTC March 15	30km, 10km	
WRF1512	1200 UTC March 15	30km, 10km	
WRF1518	1800 UTC March 15	30km, 10km	
WRF1600	0000 UTC March 16	30km, 10km	
WRF1612	1200 UTC March 16	30km, 10km	
WRF1700	0000 UTC March 17	30km, 10km	
WRF15HR	0000 UTC March 15	9km, 3km	
WRF16HR	0000 UTC March 16	9km, 3km	
WRFMP	0000 UTC March 15	30km, 10km	WSM6 bulk microphysics scheme
WRFCU	0000 UTC March 15	30km, 10km	Kain-Fritsch cumulus clouds scheme
WRFPBL	0000 UTC March 15	30km, 10km	MYNN planetary boundary layer scheme

Table 3.1: Summary of the configurations for the WRF simulations.

Chapter 4

Weather conditions on March 15-17

This chapter contains results and analysis from dropsondes launched during the Andøya field campaign, satellite images and model weather analyses provided by ECMWF, right before and during the life cycle of the polar low. Topics like the role of potential vorticity in different altitude, forcing mechanisms and type of polar low, will be addressed. The aim of this is to have the best basis for understanding the weather conditions in which the polar low developed, and also to be able to validate the simulations in chapter 5. This chapter is divided into four main sections. First, this chapter will focuses on the atmospheric conditions prior to the formation of the polar low, with the satellite images, ECMWF-analysis and results from the dropsondes on March 15. Secondly the weather conditions during cyclogenesis will be investigated. This period reaches from 0000 UTC to around 1800 UTC on March 16. The third section focus on the structure and movements of the low from 1800 UTC on March 16, until the low makes landfall 18 hours later. Dropsondes with measurements from the low at mature stage on March 17 are presented in this section. The satellite images used in this chapter are retrieved via NEODAAS - the Dundee satellite receiving station[1]. All the results from HIRLAM are presented using the meteorological visualization and production software, DIANA[2] developed by DNMI.

4.1 Weather conditions prior to cyclogenesis

According to Kristjánsson et al. (2011) the weather conditions changed around March 12 to gradually become more favorable for polar low development.

[1]http://www.sat.dundee.ac.uk/
[2]https://diana.wiki.met.no/doku.php

From March 15, a sustained period of high MCAO index values, sometimes more than 10 units higher than the climatological mean, occurred in the region east of the 0°meridian. The favorable conditions was found in various factors. The temperature difference between the 500hPa-layer and the sea surface exceeded 40K, there was an upper-level low (around 500hPa), and a PV-anomaly propagating along the tropopause was approaching the area of interest.

Figure 4.1 shows the satellite image from 1121 UTC (4.1(a)), and the ECMWF model analysis at 1200 UTC on March 15, with surface pressure and wind fields (4.1(b)), and potential vorticity (PV) at the upper level, approximately 290K-surface[3] (4.1(c)) and absolute vorticity (AV) at the lower layer approximately 925hPa-surface[4] (figure 4.1(d)), from when the flight missions of March 15 were made.

In figure 4.1(b) there is a surface trough stretching north-westward from off the coast of the counties of Troms and Finnmark, Norway, at about 71°N and 15°E, leading to the Fram Strait in between Greenland and Spitsbergen around 77°N and 3°W (not seen in the figures). A band of high clouds, seen in the satellite image in figure 4.1(a), lies above the whole surface trough on its north-eastern side, indicating a confluence zone between the warmer surface air within the trough and the cold air to the north.
There is a surface low present within the trough just south-west of Spitsbergen, at 75°N and 5°E with a minimum pressure of 1003hPa. Comparing the surface low with the satellite images, shows that the low is stationed almost in the middle of the high clouds following the trough. The wind speed is high on both sides of the surface low.

An upper-level PV-anomaly is approaching from the west and can barely be seen between 72 and 74°N in the left edge of figure 4.1(c). There is also an area of high PV over Spitsbergen at the north-eastern corner of the domain, where PV exceeds 1 PVU. AV is a measure of the rotation in the fluid, and the distribution of AV is therefore a good diagnostic for weather analysis (Holton (2004)). Regions of positive absolute vorticity are associated with cyclonic storms. The AV at the lower levels (figure 4.1(d)) is high along the whole trough, with a maximum of $70 \times 10^{-5} s^{-1}$ at the area around the surface low.

[3]The closest value to 290K in each vertical column has been chosen.
[4]Same as 290K, but for 925hPa.

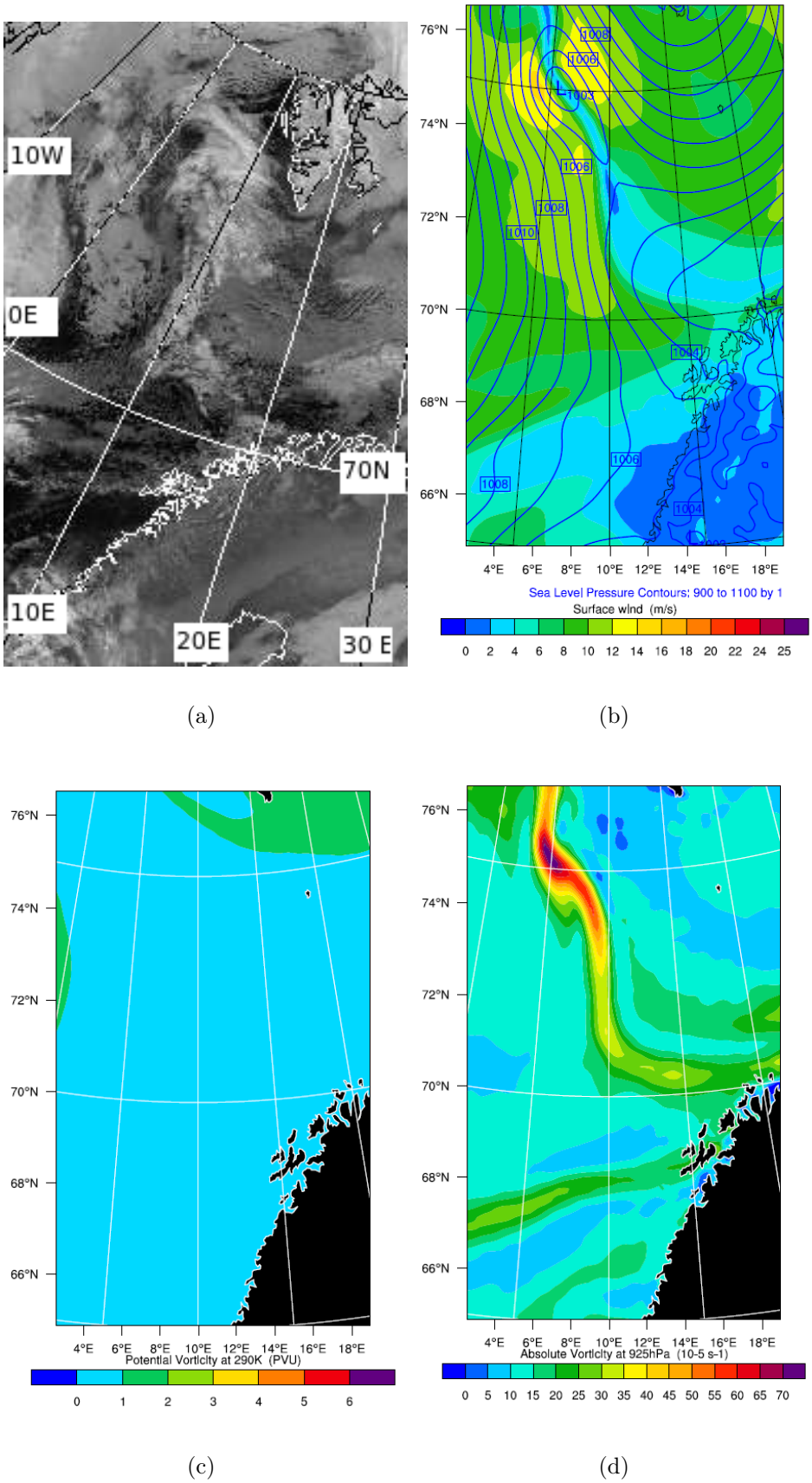

(a) (b)

(c) (d)

Figure 4.1: Analysis from 1200 UTC on March 15. a) NOAA AVHRR channel 4 IR-satellite image at 1112 UTC. Retrieved from Dundee Satellite Receiving Station. ECMWF-analysis of b) surface pressure and wind, c) PV at approximately 290K and d) AV at approximately 925hPa.

4.1.1 Cross sections from March 15

On March 15, the Falcon aircraft flew from Andøya to Spitsbergen, landed in Longyearbyen, and then flew back to Andøya, with a detour just north of Spitsbergen. The data from some of these dropsondes were processed first in Aspen[5] and then in MATLAB[6] to give two sets of vertical cross sections. These plots give an overview of the atmospheric conditions in an approximately straight line from the first to the last dropsonde. The next two subsections will focus on the results from these flights, but more on the first flight as it is taken closer to the area where the polar low actually formed.

Cross section A

The first flight (Flight A) lasted for about two hours, and six dropsondes were launched in the morning hours on March 15, reaching from 71°N 14.5°E, just off the coast of Finnmark, Norway, to 80°N 2.5°E, north-west of Svalbard. The first three dropsondes were dropped over open ocean, while number 4 and 5 were dropped quite close to the land on Spitsbergen. The sixth dropsonde was launched "well on the ice", according to the flight protocol. Figure 4.2 show the positions of the dropsondes. Data from the dropsondes were plotted in an approximately north-south vertical cross section, with dropsonde 1 in the south and 6 in the north. The cross sections are shown in figure 4.3. The spots where the dropsondes were dropped is marked on top of the figures, and the rest of the figure has been generated by the interpolation function in MATLAB. It should be mentioned that there are several hundred kilometres between some of the dropsondes, so the cross sections do not give the exact variations. Note that dropsonde 1 was launched where the polar low developed about twelve hours after the soundings were taken.

In figure 4.3(a) the vertical cross section of the temperature is plotted as a function of latitude and pressure. The surface temperature is around 0°C at dropsonde number 1 and 2, and then gradually decrease to -12°C before dropsonde number 5. There is a clear drop between dropsonde 5 and 6, probably due to the ice cover at dropsonde 6. Surface temperatures in that area drop to about -25°C. The horizontal surface temperature gradient indicate strong baroclinicity in the whole cross section.In the surface region around dropsonde 6, the temperature is increasing with height, indicating an inversion around 900hPa, which can also be seen in the potential temperature and equivalent potential temperature profiles in figures 4.3(b) and 4.3(c). This is common for arctic air over ice or other cold surfaces. A small increase in the temperature with height also in the region at 900hPa-level from dropsonde

[5]http://www.eol.ucar.edu/isf/facilities/software/aspen/aspen.html
[6]http://www.mathworks.se/products/matlab/index.html

3 to 5, is probably also due to a weak inversion. At dropsonde 1-3, the same can be found at a higher altitude at 800hPa height, indicating a deeper mixed layer than in the rest of the section.
The temperature difference between the surface air at dropsonde 1 and the 500hPa layer is around 36 K, 8 K lower than the typical threshold value found by Blechschmidt et al. (2009). An interesting feature in this region is that the temperature is constant up to 950hPa, indicating a very well mixed surface layer, possibly due to convection.

The potential temperature in cross section A is shown in figure 4.3(b). A strong inversion is seen at the northernmost area between dropsonde 5 and 6. at 900hPa, where the air below appears very stable. In contrast, the rest of the section appears to be relatively well-mixed up to the inversions. Near the 650hPa-layer is a second inversion between dropsonde 2 and 3, with relatively well mixed air in the layer between the first inversion and the second. In the surface layer, up to 950hPa, the potential temperature is nearly constant with height, indicating instability.

This surface instability is also seen in figure 4.3(c), which illustrates the equivalent potential temperature in the cross section. The equivalent potential temperature is actually decreasing with altitude in the surface layer in most of the figure. Also in the layer above 950hPa the troposphere is only neutral, or weakly stable up to the inversion at 800hPa, and above the inversion is another layer with neutral or even unstable air up to 700hPa, between dropsonde 1-3. The lower part of the troposphere is stable only in the northmost regions. The area around dropsonde 1 should be noted once again, as there are no inversions before 700hPa, and the troposphere is unstable or neutral up to this height, a sign of convection. Linders and Saetra (2010) estimated the time-scale t_{CAPE} that is necessary for the heat fluxes from the ocean to transfer the corresponding amount of energy stored in CAPE, and found very low values of between 1-41 minutes for the three first dropsondes in this cross section. The rest of the profiles had no positive CAPE. They suggested that the low time-scales means that the energy from the ocean surface fluxes was not stored, but released as convection at once due to an unconditional instability.

The relative humidity (RH) profile, given in figure 4.3(d) confirms the trends seen in the previous figures. In the southern part of the cross section, the relative humidity is very high, with values of 80% up to 550hPa and 60% up to 400hPa height at dropsonde 1, indicating convective clouds, which is probably also present at dropsonde 3. The northern part is very dry in comparison, with values of more than 60% only up to 850hPa. The division between the maritime and arctic air is pronounced between dropsonde 3 and

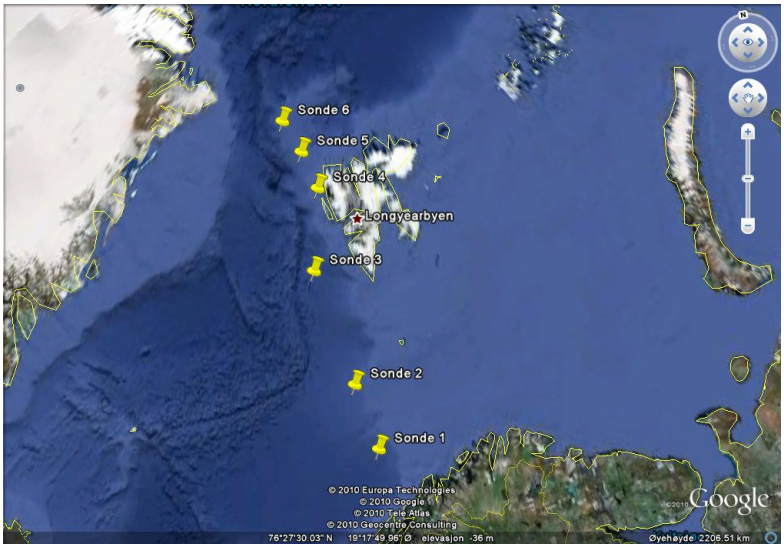

Figure 4.2: Dropsondes launched during flight A. (Generated using google earth: http://www.google.com/earth/index.html)

4, where the relative humidity values drop from over 80% in the 600hPa layer down below 20%, indicating a frontal structure.

Figure 4.3(e) mirrors the trends in the past figures. This figure gives the specific humidity of the cross section, and shows high surface values in the south. The values in the south are almost 9 times less than the values in the north. The inversions appear pronounced in this figure.

The wind speed and directions are plotted in figure 4.3(f). The arrows indicate the direction of the wind, and is given in a horizontal plane, that is, the arrows give the direction in north-south and east-west, and must not be confused with the vertical plane in the cross section. The wind is generally in the opposite direction in the lower and the higher levels, with easterly winds near the surface, and westerly winds in the higher levels. The values reach a peak at dropsonde 3, where the wind exceeds 18 m/s at 400hPa and above. This could indicate an upper-level jet, in accordance with the area of positive PV-anomaly over the southern tip of Spitsbergen, as seen in figure 4.1(c). Near the surface, the strength of the wind is generally lower, but it is between 12-14 m/s at dropsonde 3 and 5-6. Even in this figure there is a clear division between the northern and southern part, between dropsonde 3 and 4, with a change in direction and wind speed on each side of the surface trough, as seen in the surface analysis in figure 4.1(b). A reversed shear can be seen in the lower layers near dropsonde 3 and also at dropsonde 5 and 6, where the wind speed is decreasing with height. Kolstad (2006) connected reverse shear to cold air outbreaks.

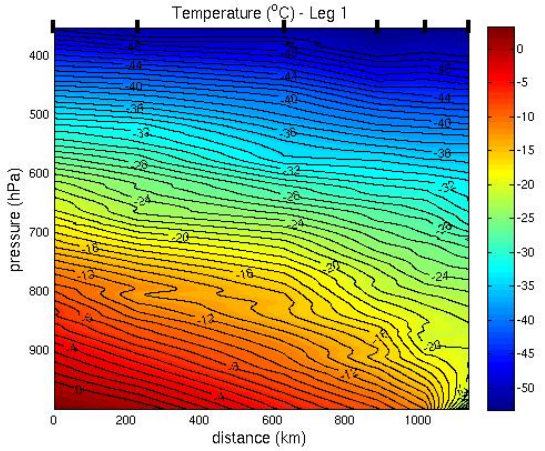

(a) Temperature in Celsius.

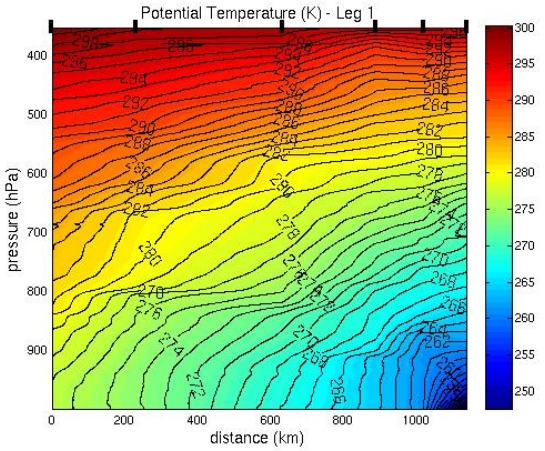

(b) Potential temperature in Kelvin.

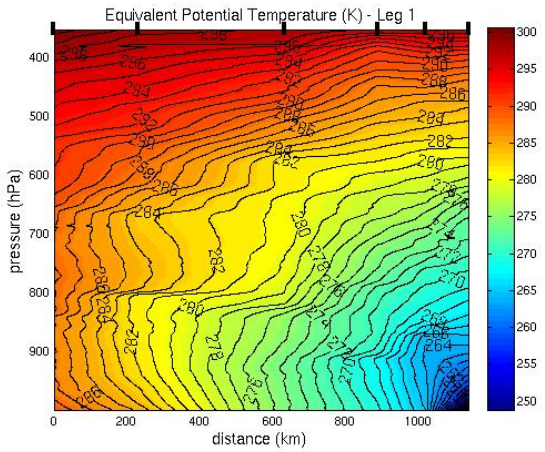

(c) Equivalent potential temperature in Celsius.

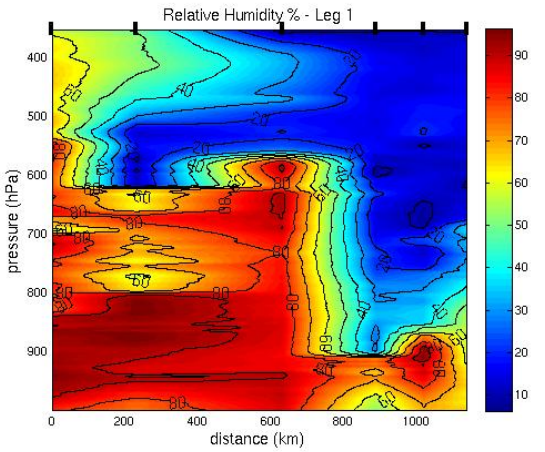

(d) Relavtive Humidity in %.

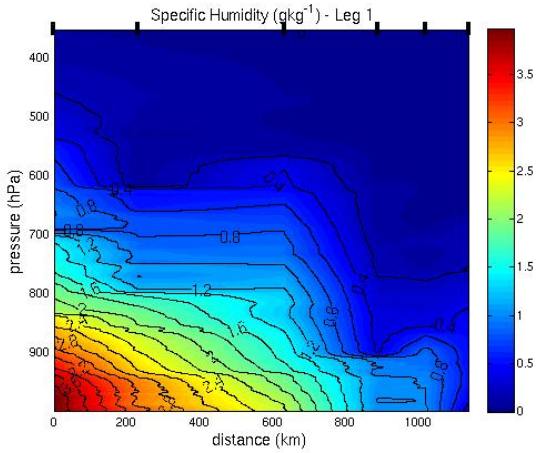

(e) Specific humidity in g/kg.

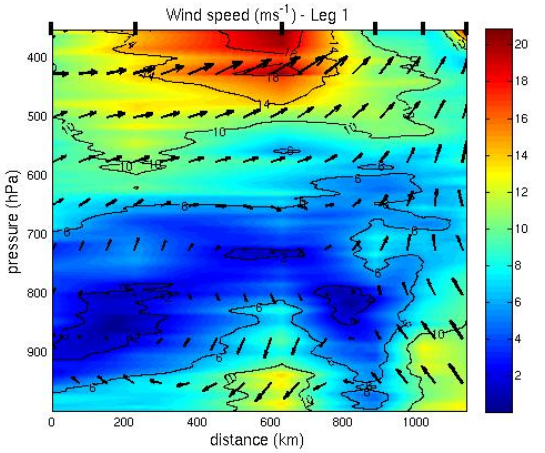

(f) Wind speed in m/s.

Figure 4.3: Results from cross section A. South (dropsonde 1) is to the left in the figures, and north is to the right (dropsonde 6). The black dots on top of each frame marks the dropsondes.

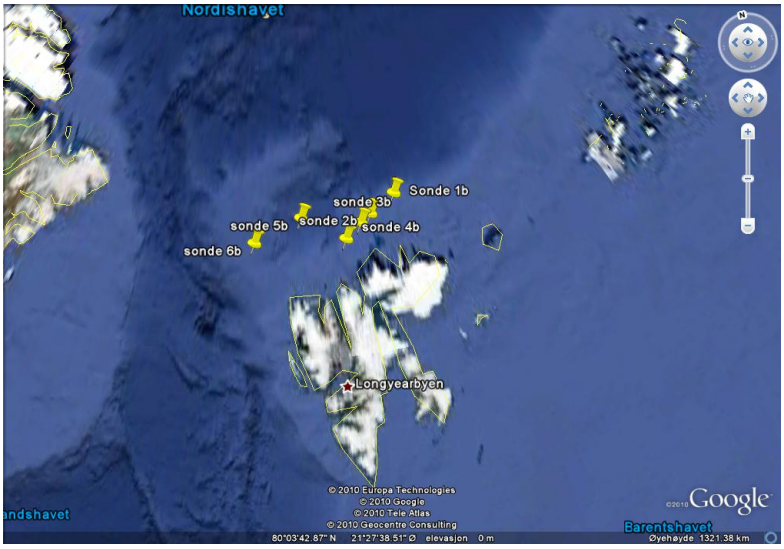

Figure 4.4: Dropsondes from flight B. (Generated using google earth: http://www.google.com/earth/index.html)

Cross section B

The second flight lasted about two hours starting around 1300 UTC on March 15, and focused on the atmosphere just north of Svalbard. Eight dropsondes were launched, the first six on the ice north of the islands Spitsbergen and Nordaustlandet, the seventh northwest of prince Karls Forland, and the eighth just southwest of Spitsbergen quite close to dropsonde 3 from cross section A. The first six were dropped almost on a straight line, and were used to plot a set of vertical cross sections of the troposphere. The positions of the dropsondes are shown in figure 4.4. The resulting cross sections are shown in figure 4.5. The figures are west-east oriented with dropsonde 1 to the right (east) and dropsonde 6 to the left (west).

The dropsondes were dropped over or very close to the sea ice in the arctic, and the air measured was therefore relatively cold and dry, compared to the first cross section. The surface temperature in figure 4.5(a) does not vary much, and is just below -20°C in the whole cross section, except in the region of dropsonde 1-3, where the temperature is lower, around -25°C. This is probably due to a change in the surfaces from ocean to ice. There are some pockets with higher temperatures just over the surface layer at about 900hPa at the eastern side, which indicates temperature inversions. There are few baroclinic regions in this cross section, only in the surface area between the dropsondes 2-4 is there some baroclinicity. The temperature difference between the surface and the 500hPa is only 25 K at most, so the conditions do not appear favorable for polar low development in this region.

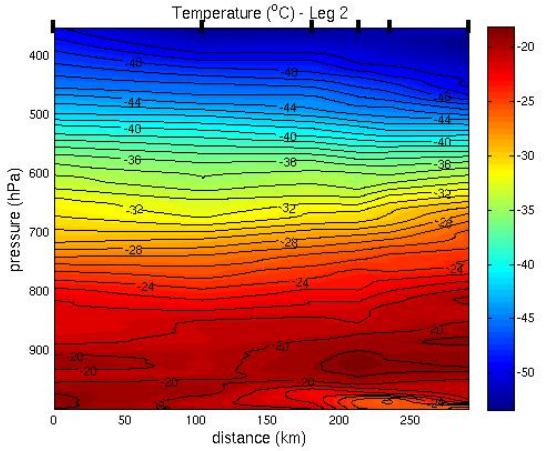

(a) Temperature in Celsius.

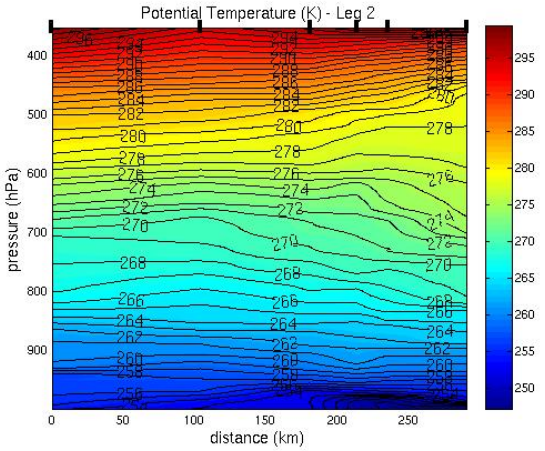

(b) Potential temperature in Kelvin.

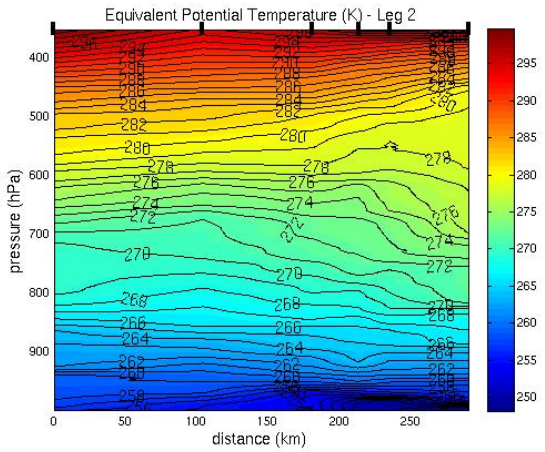

(c) Equivalent potential temperature in Celsius.

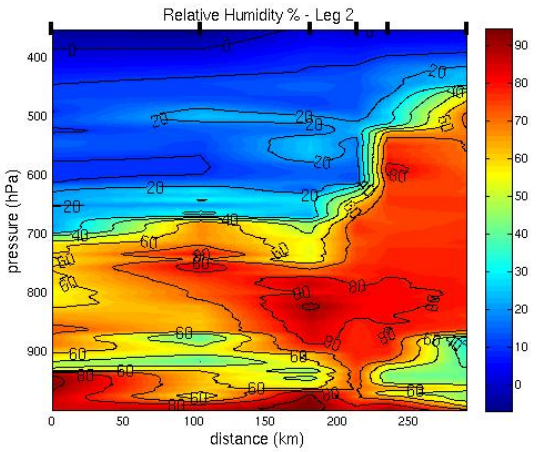

(d) Relavtive Humidity in %.

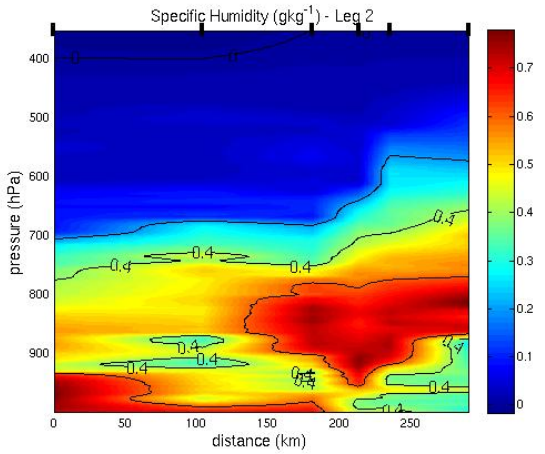

(e) Specific humidity in g/kg.

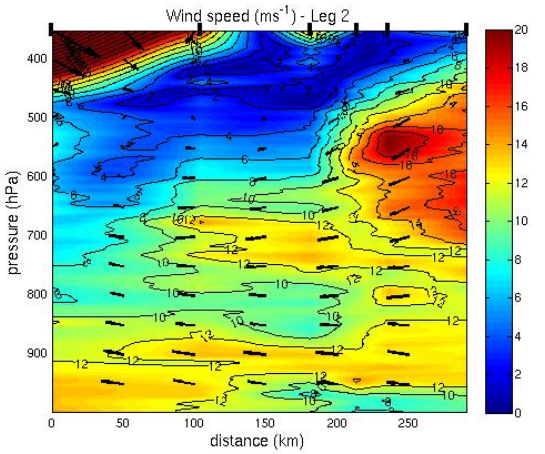

(f) Wind speed in m/s.

Figure 4.5: Results from cross section B. West (dropsonde 6) is to the left in the figures, and east is to the right (dropsonde 1). The black dots on top of each frame marks the dropsondes.

The potential temperature in figure 4.5(b) shows that the troposphere is generally stable in the lowest and highest levels. In the layer between 750hPa and 500hPa, however, there is a less stable region between dropsonde 1 to 4. The vertical potential temperature gradient is weaker in this area, which also makes the atmosphere less convective stable. A quick look at the relative humidity in figure 4.5(d), reveals high values consistent with clouds that can be seen in the satellite image in figure 4.1(a). Figure 4.5(c) illustrates the equivalent potential temperature, and resembles the potential temperature figure a lot, since the arctic air in the region normally is very dry. But the area mentioned earlier with less convective stability above 800hPa is more pronounced in this figure. This can also be seen in figure 4.5(e) which illustrates the specific humidity. Overall the specific humidity is low, with only 0.8 g/kg as maximum value (compared to 3.6 g/kg in the previous section) in the surface region between dropsonde 6-4. The division in the surface air over ice and sea is easily spotted between dropsonde 3 and 4, as a pronounced drop in the specific humidity. However, it is interesting to note the relatively high specific humidity between 800-900hPa at dropsonde 1-4. It is evident that this moisture does not come from the surface in that area. It is possibly advected over the ice from the east, which is in accordance with the strong winds and wind direction in the area.

The relative humidity is plotted in figure 4.5(d). Even with the relatively small amount of specific humidity throughout the whole cross section, the relative humidity is high near the surface and in the layer between 850-700hPa, and also up to 500hPa at the eastern part of the figure. This might indicate clouds even though the RH is never higher than 90%. There is possibly some fog close to the surface between dropsonde 6 and 4 at the division between ice and ocean, where the RH exceeds 90%.

The wind profile is shown in figure 4.5(f). The wind is generally uniform both in speed and direction in most of the lower troposphere up to 700hPa, with easterly wind of 10-12 m/s. In the upper layer there is more variation. In the eastern part, there is a section with higher wind speed up to 18 m/s and this is possibly a jet. The section above 450hPa at dropsonde 6 stands out. The wind speed increases rapidly, and the direction changes to north-westerly winds due to an upper-level jet close to the tropopause. This could be the arctic jet. There is a reversed shear in the lower levels between dropsonde 6, where the wind speed is decreasing with height.

4.2 Cyclogenesis

From 1200 on March 15 UTC until 0000 on March 16 the conditions turn even more favorable for polar low development. Figure 4.6 shows the development up to 1800 UTC on March 15. The satellite images show a huge increase in the cloud mass above the surface trough from 1121 UTC to 1942 UTC on March 15 (figure 4.6(a)). These clouds appear very white on the IR-images, indicating that the cloud tops are found at high altitudes, and therefore are cold. Furthermore, the ECMWF model analysis at 1800 UTC on March 15 (figure 4.6(b)), clearly shows that the northern end of the surface trough has been forced southwards, letting the cold arctic air flow southwards over the open ocean, consistent with the sudden appearance of very high convective clouds. Distinct wave patterns in the clouds consistent with the movements of the trough has also appeared in the satellite image at this time. There appears to be some development in the cloud pattern over the surface low at 75°N and 5°E and also at 76°N and 0°E at the very end of the surface trough. Polar air from Greenland also appears to be advancing from west, sharpening the pressure gradients also on the trough's western side.
The area of upper-level PV anomaly is now clearly entering the domain from the west, seen in figure 4.6(c). PV now exceeds 2 PVU at the western side of the domain. The area of maximum AV at lower-levels in figure 4.6(d), has become larger, but remain stationary consistent with the surface low.

At midnight on March 16 the low pressure within the surface trough has weakened. A satellite image from 0115 UTC and ECMWF-analysis of surface pressure and wind, along with upper-level PV, from 0000 UTC, are shown in figure 4.7. The northerly wind continues to force the surface trough southwards, and it is now very clear that this is a cold air outbreak.
At the south-eastern end of the trough, a new low has developed in a small basin of warm surface air near the coast of Troms at 70°N and 17°E. Minimum pressure of this low is 1000hPa. A satellite image from 0115 UTC on March 16 shows a nearly circular area of high cumulus clouds just northwest of the surface low at 71°N and 12°E at the southern end of the cloud band associated with the surface trough. Colder continental air is advected from Greenland and is emerging from the west of the domain, also bringing a high upper-level PV-anomaly seen in figure 4.7(c). The area of high PV is approaching the surface trough, with maximum values exceeding 4 PVU in a small area near the western edge of the domain. An arm of PV values exceeding 2 PVU is stretching along the northwestern part of the trough. It is interesting to note that the area of highest AV (figure 4.7(d)) has now moved southwards along the trough, away from the surface low.

Satellite images indicate polar low development around 0400 UTC on March 16, when the cluster of high convective clouds next to the surface low starts

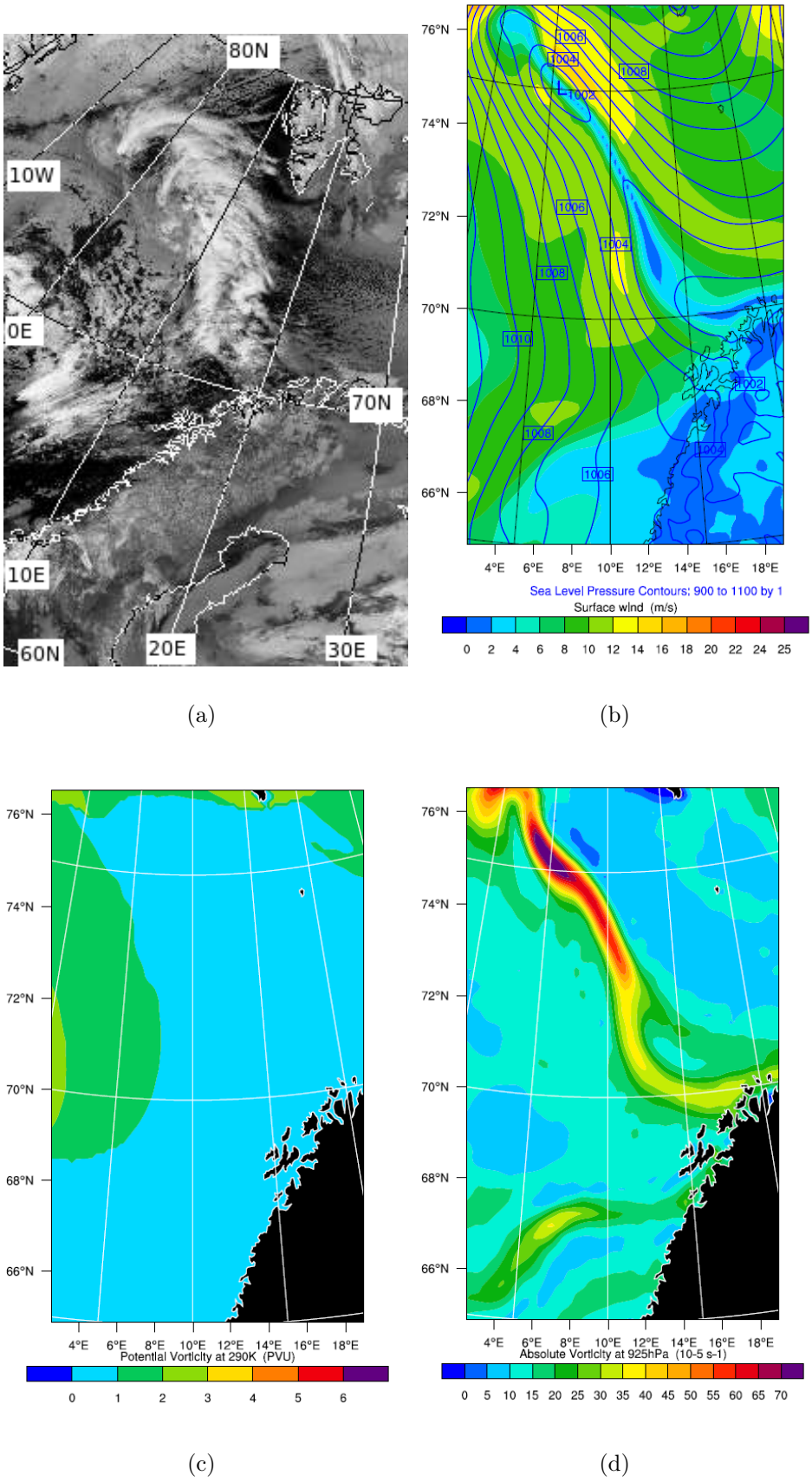

Figure 4.6: Analysis from 1800 UTC on March 15. a) NOAA AVHRR channel 4 IR-satellite image at 1942 UTC. Retrieved from Dundee Satellite Receiving Station. ECMWF-analysis of b) surface pressure and wind, c) PV at approximately 290K and d) AV at approximately 925hPa.

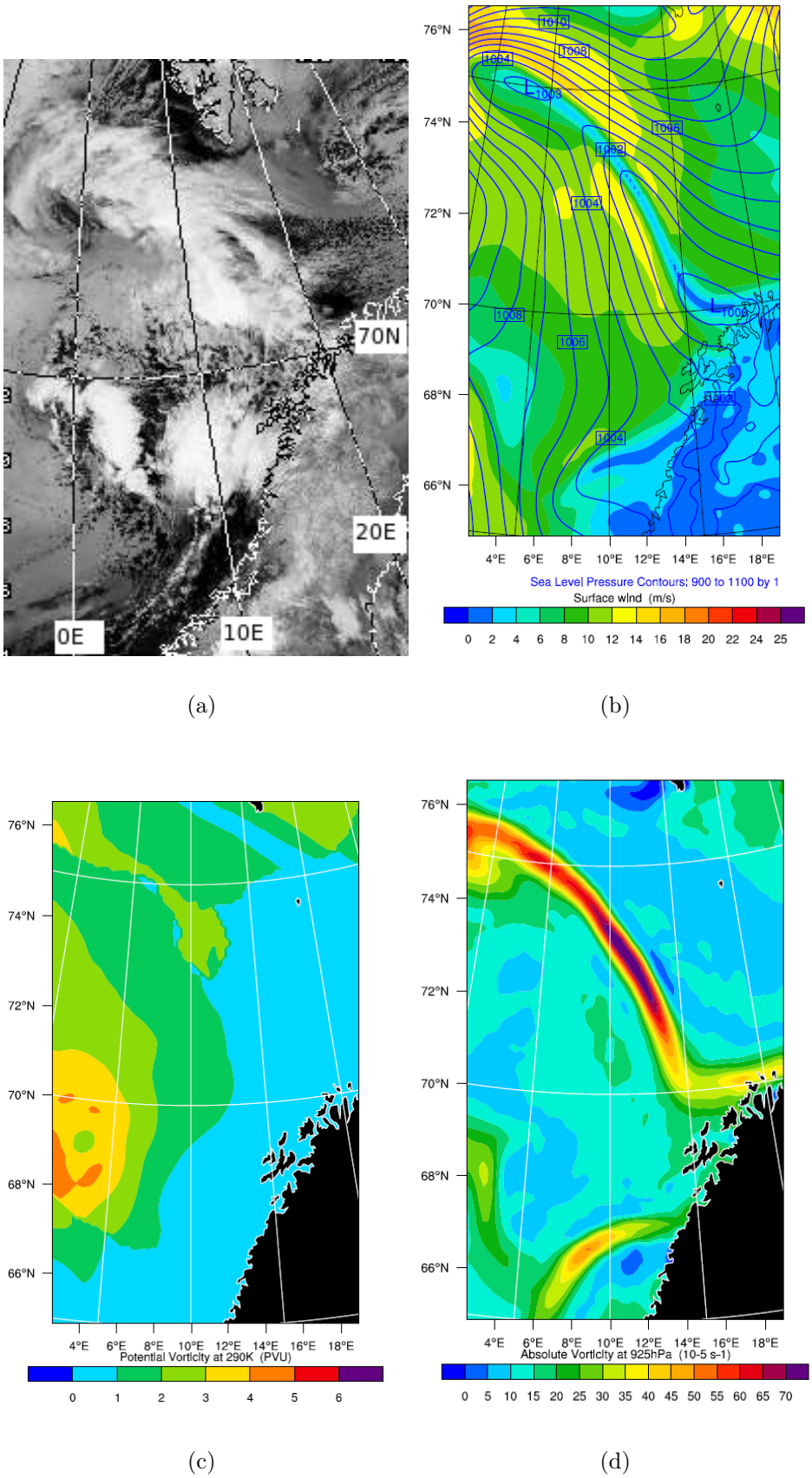

(a) (b)

(c) (d)

Figure 4.7: Analysis from 0000 UTC on March 16. a) NOAA AVHRR channel 4 IR-satellite image at 0115 UTC. Retrieved from Dundee Satellite Receiving Station. ECMWF-analysis of b) surface pressure and wind, c) PV at approximately 290K and d) AV at approximately 925hPa.

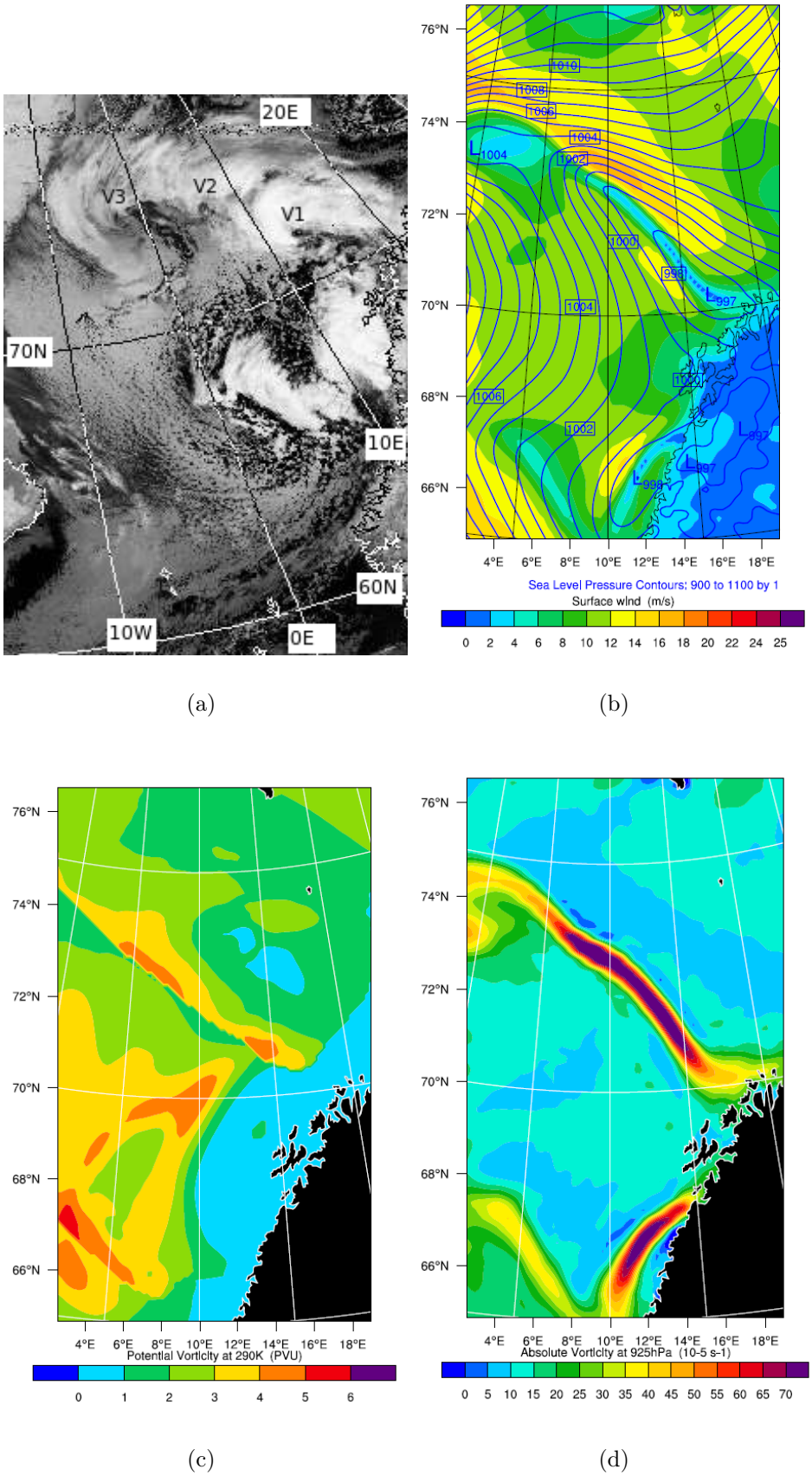

(a) (b)

(c) (d)

Figure 4.8: Analysis from 0600 UTC on March 16. a) NOAA AVHRR channel 4 IR-satellite image at 0608 UTC. Retrieved from Dundee Satellite Receiving Station. ECMWF-analysis of b) surface pressure and wind, c) PV at approximately 290K and d) AV at approximately 925hPa.

to rotate. Figure 4.8(a) shows the satellite image at 0608 UTC. A very special feature in this image, is the three vortices within the cloud band, which makes out a particular wave-pattern. The vortices are named V1, V2 and V3 in the figure, and they are stationed at 72°N and 13°E, 73.5°N and 5°E and 74°N and 3°W, respectively. V1 is the most evident of the vortices and has already what appears to be an eye-like structure in the center. This is also the vortex that will develop into a polar low.
The ECMWF model analysis at 0600 UTC (figure 4.8(b)), shows a clear deepening of the surface low near the coast of Troms, from 1000hPa to 997hPa. This low has stretched itself somewhat to the north-west and now partly cover the area where V1 is shown on the satellite image. Interestingly enough, the second surface low at the end of the original trough still covers the area of the two other vortices. But this low is weak and about to dissipate.
The high PV-anomaly continues to flow further into the domain, and the highest values are now found at the south-western corner exceeding 5 PVU. This is a very high value, and values of 4 PVU are now stationed over the surface trough and particularly over V1 and V2. This can possibly contribute to further development through deepening of the low, as described in chapter 2.
A huge increase in lower-level AV along the surface trough is found in figure 4.8(d), and covers the area of V1 and V2, indicating cyclonic rotation.

From 0600 to 1200 UTC, the satellite images show that V1 moves slightly south-westward to 71°N and 11°E, and can be seen on the satellite image from 1251 UTC (figure 4.9(a)) as a clear comma-shaped low. It is now so evident that it must be characterized as a polar low, and will from now on be called PL instead of V1. The two other vortices are no longer easily spotted on the IR-satellite images, but V2 can still be seen in the visual satellite images (not shown) as a small vortex at 73°N and 2°E, north-west of PL. The area of convective clouds surrounding PL has become much larger, and the cloud band continues to wrap itself around the center. This increased area of convective clouds indicate that convective instability now plays a major role in further intensifying the low.
The ECMWF model analysis from 1200 UTC with surface temperature, pressure and wind fields shown in figure 4.9(b) also illustrates the change of character of the low. The polar low is now fully enclosed with minimum pressure of 996hPa and has strong pressure gradients on its northern and western side. There are no signs of either of the two other vortices in within the domain. The model analysis places the low about 1°further north than the satellite images indicate, at 72°N and 11°E.
The upper-level potential vorticity distribution is shown in figure 4.9(c). An area of very high PV values exceeding 6 PVU, is now stationed over the polar low, and appears to be a result of the vortex. It is interesting to note this, as upper-level PV are normally depleted in association of a polar low. But this

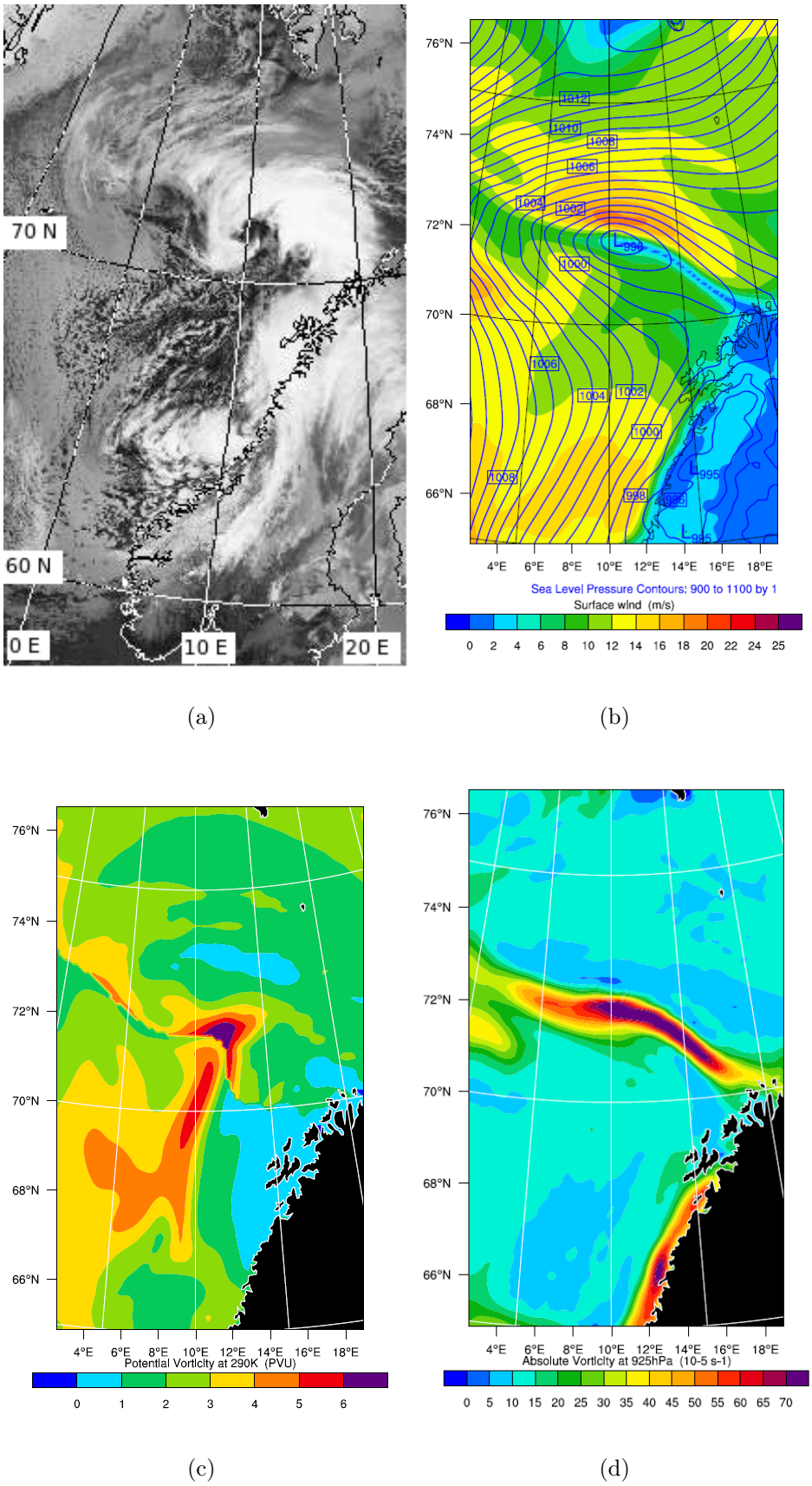

(a) (b)

(c) (d)

Figure 4.9: Analysis from 1200 UTC on March 16. a) NOAA AVHRR channel 4 IR-satellite image at 1110 UTC. Retrieved from Dundee Satellite Receiving Station. ECMWF-analysis of b) surface pressure and wind, c) PV at approximately 290K and d) AV at approximately 925hPa.

region is not stationed directly over the area with most clouds, and therefore does not experience the highest amount of diabatic heating. The low level area of high AV has decreased again mostly close to where V2 is stationed, but is still associated with the polar low.

4.3 Mature stage

V2 appears more evident in the satellite images and reaches its peak intensity around 1500 UTC (not shown), before it starts to dissipate and is nearly invisible in the IR-satellite images around 1912 UTC shown in figure 4.10(a). Only a small area of high clouds at 71°N and 1°W remains of this vortex now.
PL has moved to the south-west and is stationed at 70°N and 9°E. The indication of deepening of the polar low from the previous section turned out to be right. From 1200 to 1800 UTC the low has obtained a clear spirali-form appearance, with cloud bands spiraling out from its relatively cloud free interior, which indicate that the low has reached mature stage. The low, as it appears, is starting to detach itself from the large area of clouds north of the center. The strengthening of the low is also evident in the surface fields from the ECMWF-analysis at 1800 UTC shown in figure 4.10(b), as a clearly defined low pressure system with pressure minimum of 995hPa. The area of wind speeds exceeding 20 m/s has grown larger and is now on the north-western side of the low, while wind speeds on the eastern side of the low remains relatively calm. The model analysis places the center of the low around 1°further north, and also around 1°further west compared with the satellite image, at 71°N and 8°E at this time.
Figure 4.10(c) shows the distribution of upper-level PV from the ECMWF-analysis at 1800 UTC on March 16. It is evident that the wind fields of PL is affecting the upper-level PV field, due to the comma-shaped pattern of the area with very high PV. The center of the maximum PV is right above the surface low. The maximum AV values have decreased somewhat, but remain high close to the center of the cyclone.

During the next couple of hours, the polar low detaches itself completely from the large area of clouds north of it and moves southwards at a relatively high speed. The area of convective clouds shrinks rapidly after this, possibly due to less fluxes from latent and sensible heat generated by the low. The satellite image from 0104 UTC and ECMWF-analysis from 0000 UTC on March 17 are shown in figure 4.11. The IR-satellite image from figure 4.11(a) shows a well organized polar low stationed at 69°N and 6°E, south-west of the previous location.
The surface analysis now agrees with the satellite image on the latitude on

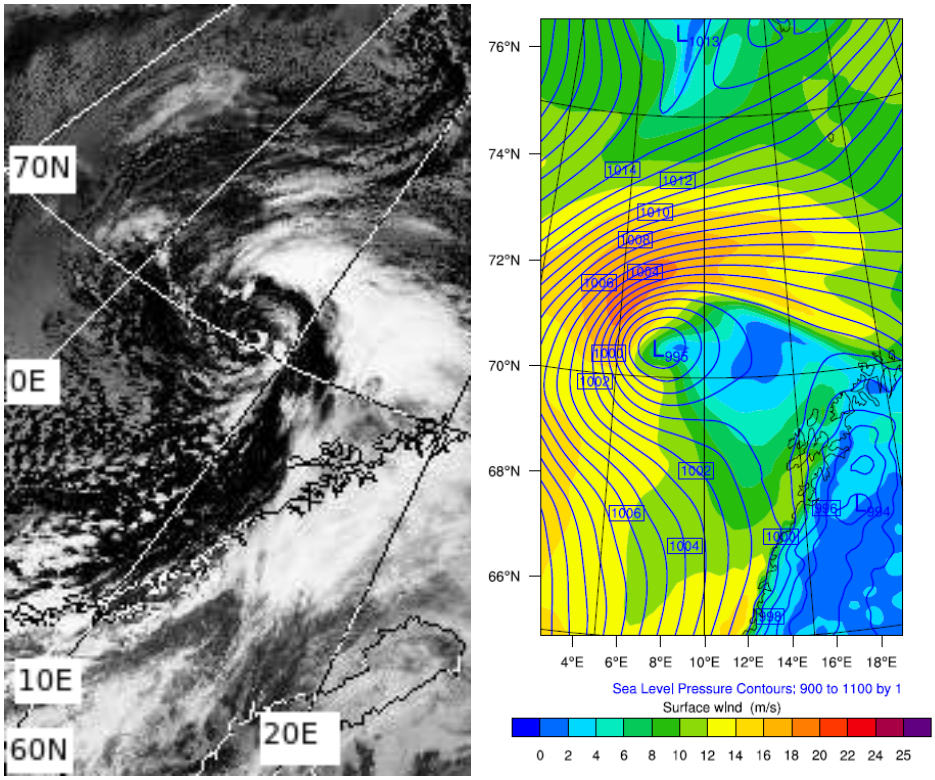

(a) (b)

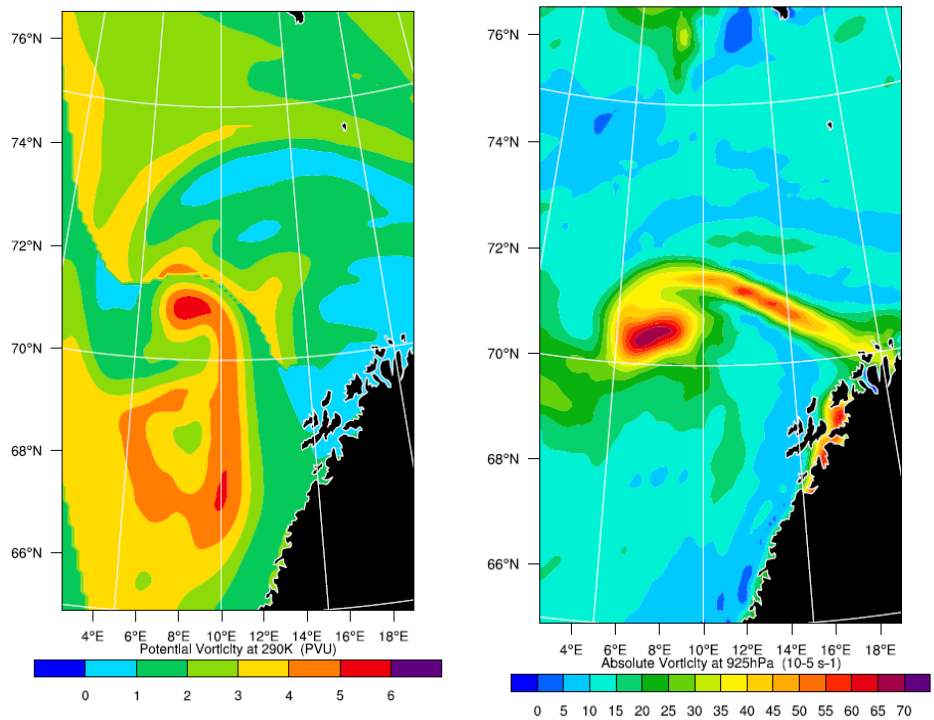

(c) (d)

Figure 4.10: Analysis from 1800 UTC on March 16. a) NOAA AVHRR channel 4 IR-satellite image at 1912 UTC. Retrieved from Dundee Satellite Receiving Station. ECMWF-analysis of b) surface pressure and wind, c) PV at approximately 290K and d) AV at approximately 925hPa.

which PL is stationed, but has placed the center 1°further east at 69°N and 7°E. Although the minimum pressure has increased with 1hPa to 996hPa, a strengthening of the pressure gradients west and north-west of the low leads to a large area of wind speeds exceeding 20 m/s. The low now appears to have developed a calm center, and the areas to the east of the low also remain calm. The area of high upper-level PV appears to follow the path of the low and is still stationed right above the center, with a tail spiraling out to its south-east. Possibly consistent with the area of cloud free air spiraling out of the low seen in the satellite image, a water vapor satellite image would reveal if this area is dry as well, which could indicate stratospheric air intrusion. The maximum AV values at the approximate 925hPa-layer continue to decrease at the center of the cyclone.

The IR-satellite image from 0544 UTC on March 17 shows that the polar low continues to travel southwards and is now positioned at 67°N and 6°E. High convective clouds are still forming spiral bands around the center, but appear less organized now. The ECMWF surface analysis show that the low has moved away from the area of the highest wind speeds, but winds are still relatively high at the western side of the low. Minimum pressure is still 996hPa at the center, and the calm area inside the center is now enclosed from the rest of the calm area on the eastern side of the low. Do note the new low that has developed south-west of Spitsbergen.

The upper-level PV-anomaly marks the position of the low with the highest PV values. The AV profile could possibly indicate that the low has lost some of its structure. The center does not appear so well defined in figure 4.12(d) as in the previous figures. Another interesting feature is the tail of high AV values following the low. Within the tail at 69.5°N and 10°E, a new maximum of AV is developing, approximately where an area of high convective clouds are found. This could possibly be the beginning of a new low.

An IR-satellite image from March 17 1240 UTC is shown in figure 4.13(a). The polar low can be seen as the area of high clouds over the coast of middle-Norway at 64°N and 8°E. Some of the spiral bands of clouds are still evident in the picture, but there is no longer a clear “eye” in the center and the cloud structures surrounding have lost most of its characteristics. The low makes landfall around 1200 UTC at the coast of Trøndelag, as seen in the ECMWF-analysis of surface fields shown in figure 4.13(b). It has lost some intensity with a pressure minimum of 998hPa, but remains well defined in the surface pressure analysis. Two regions of high wind speeds follow in the wake of the low with maximum wind speeds exceeding 18 m/s.

Shortly after this, the low dissipates over land. This is an indication of a

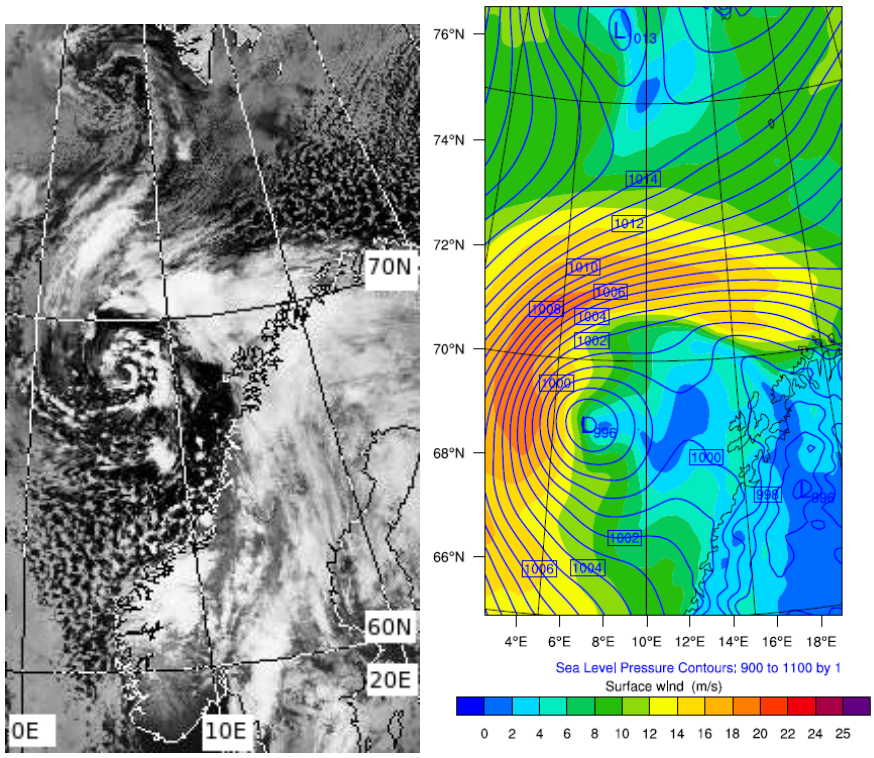

(a) (b)

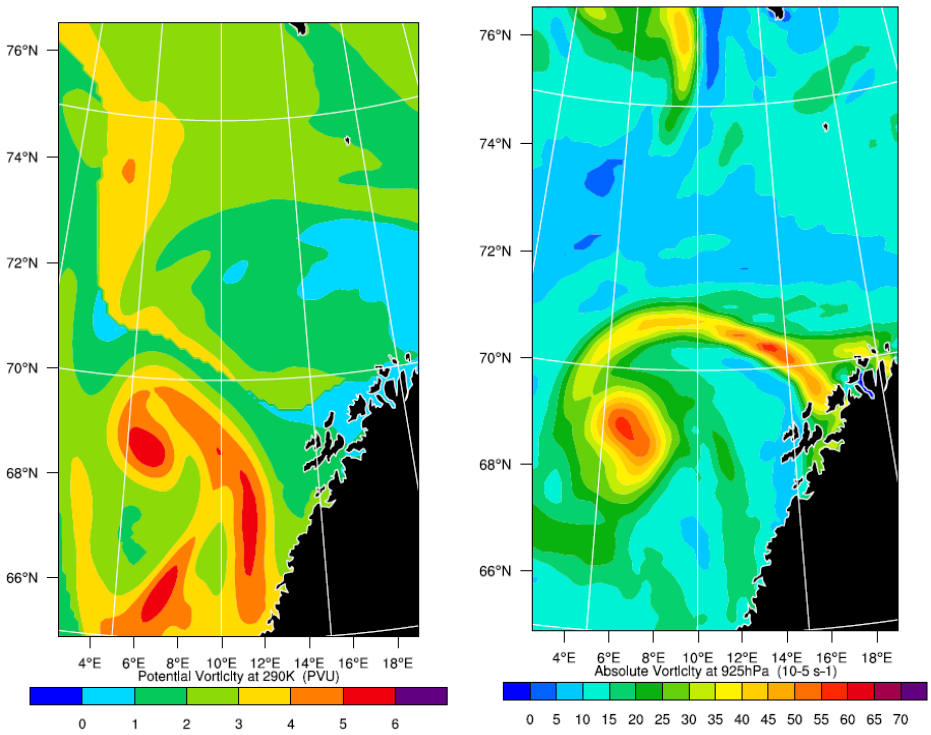

(c) (d)

Figure 4.11: Analysis from 0000 UTC on March 17. a) NOAA AVHRR channel 4 IR-satellite image at 0104 UTC. Retrieved from Dundee Satellite Receiving Station. ECMWF-analysis of b) surface pressure and wind, c) PV at approximately 290K and d) AV at approximately 925hPa.

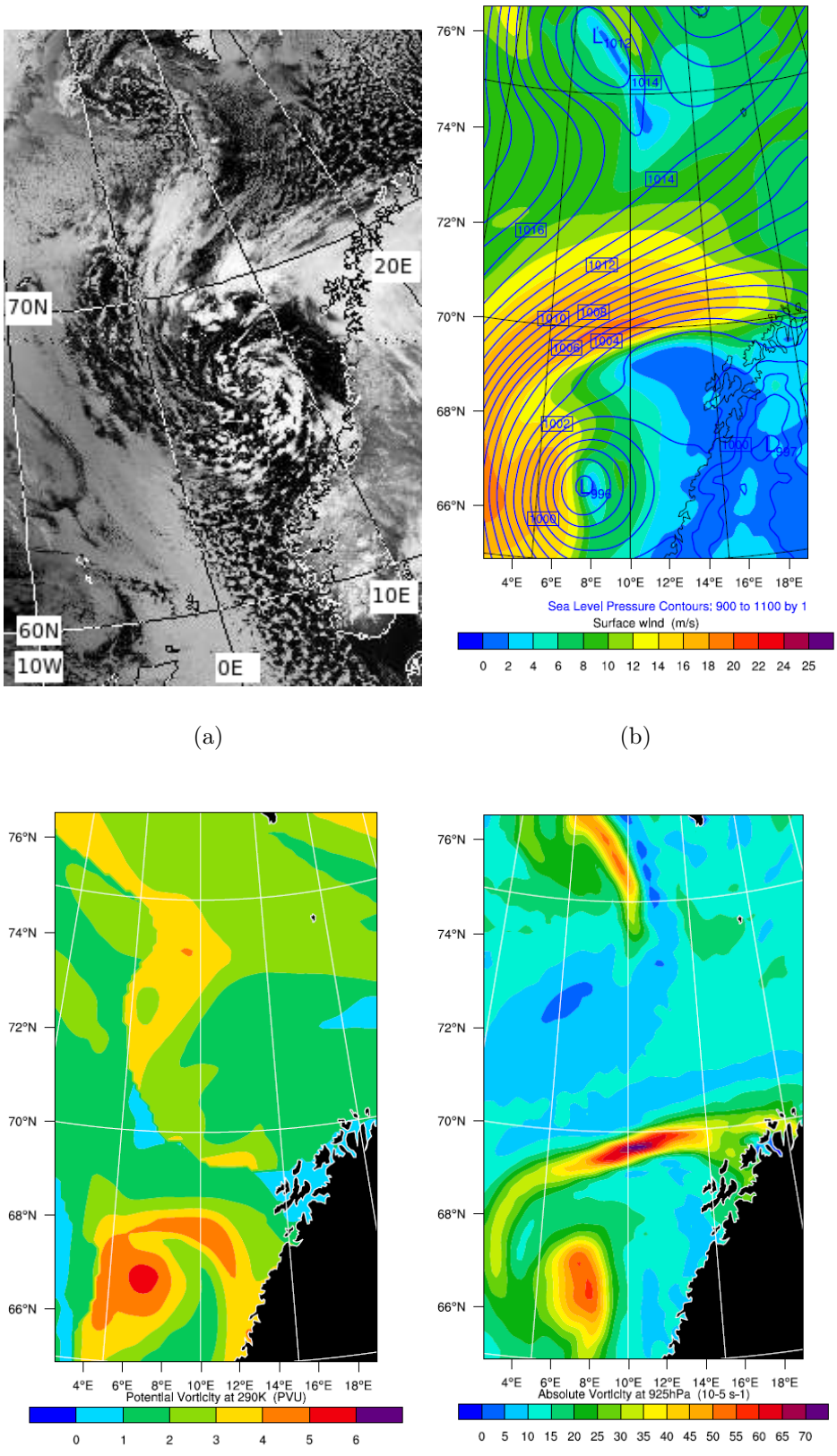

(a) (b)

(c) (d)

Figure 4.12: Analysis from 0600 UTC on March 17. a) NOAA AVHRR channel 4 IR-satellite image at 0544 UTC. Retrieved from Dundee Satellite Receiving Station. ECMWF-analysis of b) surface pressure and wind, c) PV at approximately 290K and d) AV at approximately 925hPa.

mainly convective polar low at the mature stage, since the low rapidly decays when the supply of latent and sensible fluxes is cut of. The upper-level PV values remain high over the area of the low. The AV values show three peaks in figure 4.13(d), at the polar low center, within the "tail" and at the new cyclone south-west of Spitsbergen.

4.3.1 Dropsondes from March 17

A flight was made in the morning on March 17. The aircraft flew through the polar low, which was at that time situated just north-west off the coast of Trøndelag, Norway. 13 dropsondes were launched, 11 of these making up two cross sections through the polar low. Results from the first cross section are shown in figure 4.14. The cross sections, referred to as cross section C and D with C being the northern one, are aligned in the east-west direction. This is a couple of hours before the polar low makes landfall, and considering the satellite images, the polar low was at that time at mature stage.

Cross section C

The results from cross section C are shown in figure 4.15. The figures show the vertical distribution of potential temperature, equivalent potential temperature, temperature, relative humidity, specific humidity and wind speed with wind direction. The cross section is east-west oriented with the easternmost dropsonde 1 to the right, and dropsonde 6 to the left in the figures.

Figure 4.15(a) shows the temperature distribution in cross section C. The cross section, reveals very little baroclinicity in the tropopause, so the polar low must at this time be mainly convective. The temperature is horizontally uniform in the lower part of the atmosphere, with temperature around 0°C at the surface layer. The temperature remains constant with height up to around 970hPa in most of the region, with two areas where the well-mixed surface layer appears to be higher than elsewhere, at dropsonde 5 and between dropsonde 2 and 3. It is possible that this is within convective bands in the polar low. In the uppermost layer, there is a distinct difference between the western and the eastern part, with higher temperatures in the west. This indicates that the tropopause is lower in this region. The temperature difference between the surface layer and the 500hPa-layer is 32 K at dropsonde 6 and 40 K at dropsonde 1.

The tropopause is easily seen in figure 4.15(b), which illustrates the potential temperature of the cross section. There is a clear division between the upper

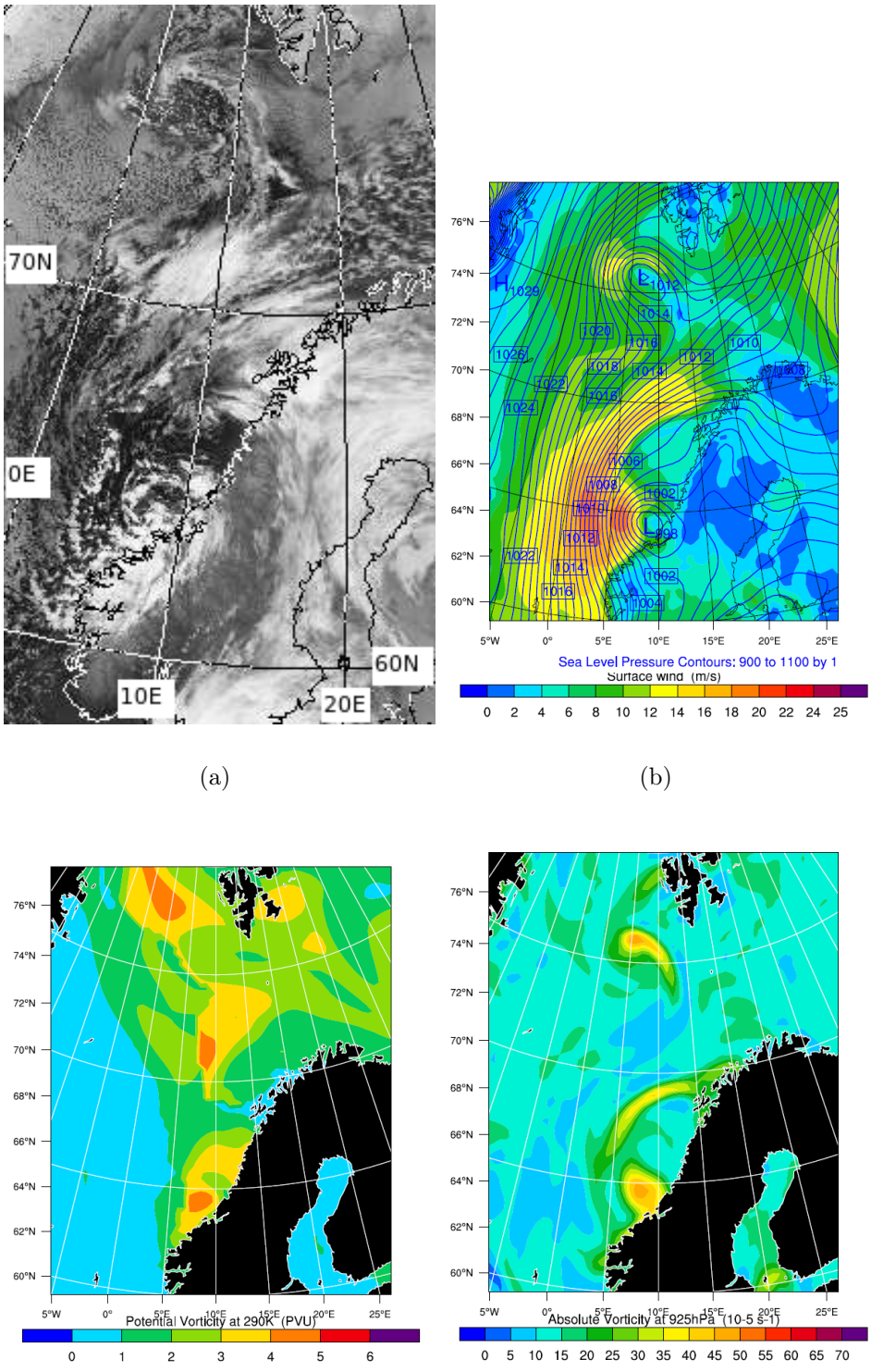

(a) (b)

(c) (d)

Figure 4.13: Analysis from 1200 UTC on March 17. a) NOAA AVHRR channel 4 IR-satellite image at 1240 UTC. Retrieved from Dundee Satellite Receiving Station. ECMWF-analysis of b) surface pressure and wind, c) PV at approximately 290K and d) AV at approximately 925hPa.

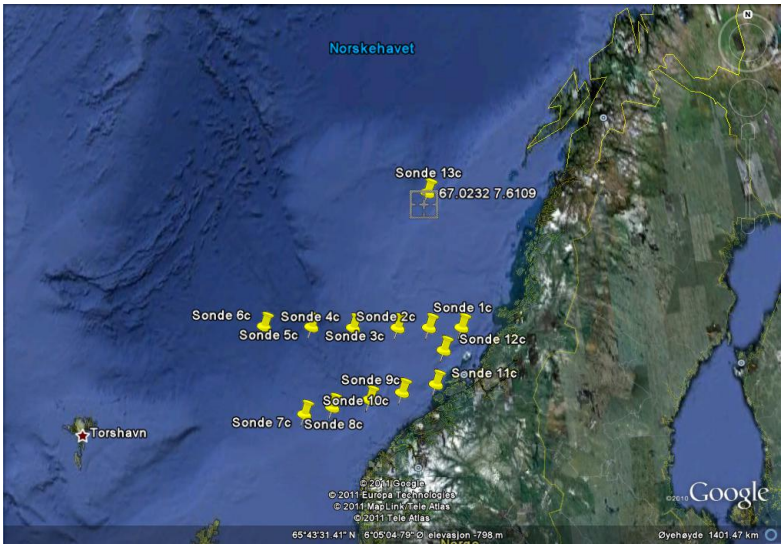

Figure 4.14: Dropsondes from flight C

and the lower part of the atmosphere. The tropopause appears lower on the left side of the cross section, which is the western part and is situated away from the polar low itself. Below the tropopause, the potential temperature is quite uniform compared to cross sections A and B. The difference in potential temperature between the surface layer and the layer just below the tropopause is only about 10°C, which indicates that the whole troposphere is relatively well-mixed, indicating that the polar low is very deep. There are also two areas from the surface to the 850hPa level, where the potential temperature is constant with height. These are the same sections, as seen in 4.15(a) at dropsonde 2-3 and 5, where there might be convective bands with ascending air.

The equivalent potential temperature shown in figure 4.15(c), displays much of the same trend as in the potential temperature, with a clear division between the troposphere and the tropopause. Apart from this, the two areas around dropsonde 2-3 and 5 once again stand out, with higher equivalent potential temperature than the rest of the surface layer. This again, strengthens the previous findings of upward motion in those areas, since there clearly is a high content of moisture. These areas fuel the polar low with warm moist air from the surface.

The relative humidity in % is shown in figure 4.15(d), and is as expected quite high in the lower part of the troposphere, until around 800hPa. The values vary from around 60 to 80 % in this region. There are higher values around 800-900hPa on each side of dropsonde 4, which indicates clouds and correlates well with the previous figures where it is presumably convective motions. A striking feature is seen at dropsonde 4, where the relative hu-

midity remains high up to 550hPa, which could be the center of the low. There is also an interesting region between 800-600hPa at dropsonde 3, with very low relative humidity compared to the ambient air. This could indicate intrusion of stratospheric air. This core region strongly resembles the core region of the March 3-4 polar low described in Føre et al. (2011).

Figure 4.15(e) illustrates the specific humidity in the cross section. The specific humidity has its peak values at the surface near dropsonde 3 with values of 3.5 g/kg. There is relatively high specific humidity up to 800hPa, above this the values remain high only at dropsonde 4 up to 550hPa. A pocket of dry air at 900hPa at dropsonde 4 supports the presumption of this being the center of the cyclone. The region of very dry air around 800-550hPa is evident also in this figure.

The horizontal wind distribution is given in figure 4.15(f). The region with the highest wind speed is the tropopause, in which a powerful jet is present, probably in association with the very high PV-anomaly seen in figure 4.13(c). Set apart from the stratospheric region the wind direction does not vary much with height. The wind direction is mainly south-westerly in the troposphere, but changes to mostly westerly winds in the eastern part of the cross section. The highest wind speeds in the troposphere are found between 700-800hPa near dropsonde 4 with wind speed of around 28 m/s. There are clearly higher wind speeds on the western side of the cross section, which is consistent with the surface analysis in figure 4.13(b) and similar to the corresponding cross section in Føre et al. (2011).

Cross section D

The results from the 5 dropsondes which makes out the 4th cross section is shown in figure 4.16. The cross section is quite close to, and almost parallel to, cross section 3. It is only taken some 100km further south. As the previous one, this cross section is also almost east-west oriented, with dropsonde 1 on the westernmost part of the section in the left of the figure, and dropsonde 5 at the easternmost part. As in the previous figures the black dots on top of the frames marks the positions of the dropsondes.

The temperature profile is shown in figure 4.16(a). As with the temperature profile of cross section C, this also show a barotropic troposphere with very weak horizontal temperature gradients. The surface layer appears more shallow compared to 4.15(a). Above the 600hPa-level there is horizontal variation that resembles the profile seen in 4.15(a), indicating a tilted tropopause.

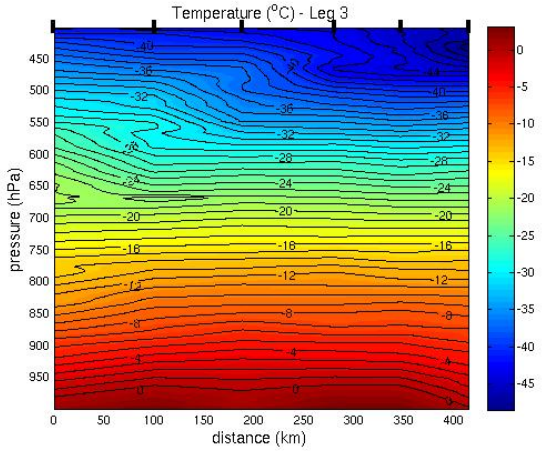

(a) Temperature in Celsius.

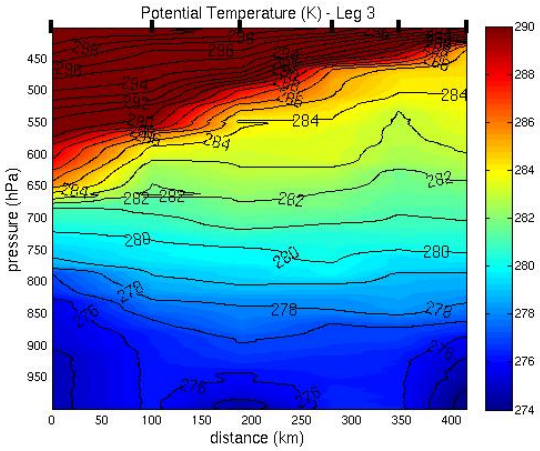

(b) Potential temperature in Kelvin.

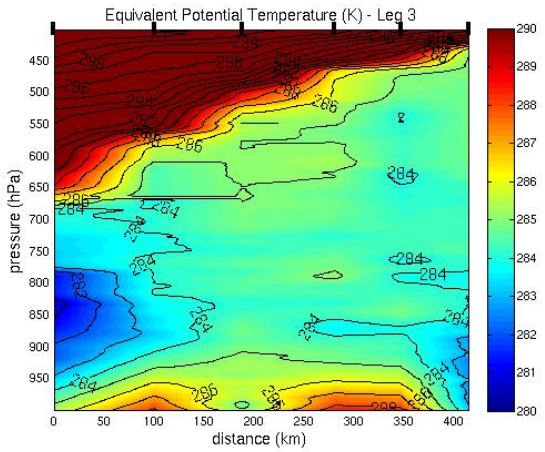

(c) Equivalent potential temperature in Celsius.

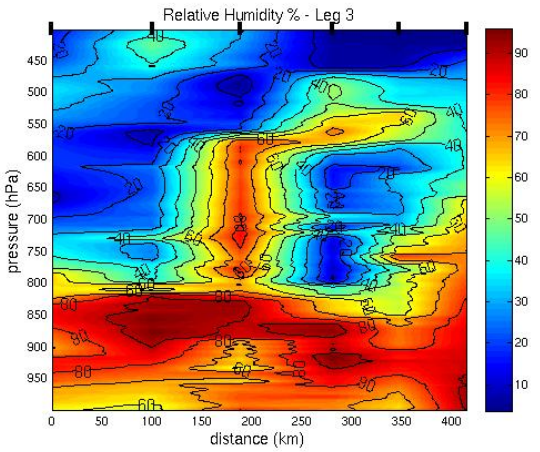

(d) Relavtive Humidity in %.

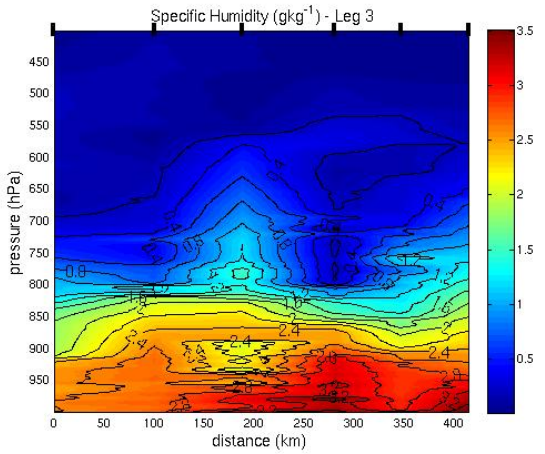

(e) Specific Humidity in g/kg.

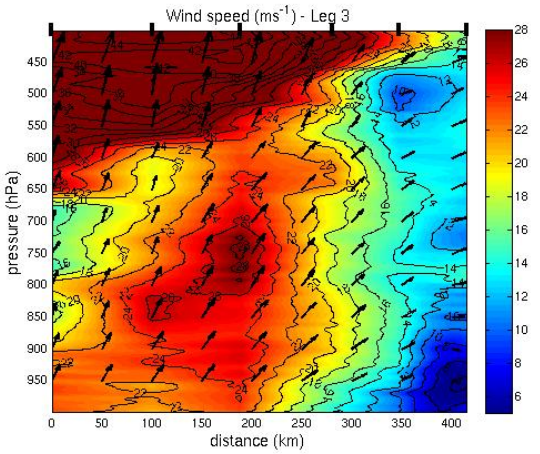

(f) Wind speed in m/s.

Figure 4.15: Results from cross section C. West (dropsonde 6) is to the left in the figures, and east is to the right (dropsonde 1). The black dots on top of each frame marks the dropsondes.

The potential temperature is shown in figure 4.16(b). As seen in 4.15(b) the potential temperature distribution does not vary much in the troposphere with only 10°separating the surface layer and the higher layers below the tropopause. Below the 800hPa-layer, the potential temperature at dropsonde 2 and 4 appear to be somewhat higher than in the ambient air.

Equivalent potential temperature is shown in figure 4.16(c) and is almost constant throughout the whole troposphere. This means that the troposphere is relatively well-mixed with respect to relative humidity. In contrast to the equivalent potential temperature distribution seen in figure 4.15(c), there are no cells of moist air near the surface in this figure, which suggest that the cross section was taken somewhat away from the center of the low.

The relative humidity profile in figure 4.16(d) also support this, as there are no well defined core structure within this frame. The relative humidity is high up to the 750hPa, with values exceeding 90% in a broad band between 900-800hPa probably in an area with much clouds. Values of 40-60% are present in the rest of the troposphere. At dropsonde 2, there is an area of dry air between 750-650hPa, which could indicate intrusion from stratospheric air.

This can again be found in figure 4.16(e), which illustrates the distribution of specific humidity. Here the values are much lower at dropsonde 2 at 750hPa. The surface values are high also in this cross section, with maximum values of 3.5 g/kg, but the surface layer is not as thick as in 4.15(e). The values are generally higher in the eastern part of the cross section near dropsonde 2. Both the upper part of the troposphere and the stratosphere are relatively dry.

The wind speed distribution is given in figure 4.16(f). The wind direction is mostly south-western in the whole cross section, but at dropsonde 4 and 5 the direction changes slightly to more westerly. In addition to the strong and pronounced jet in the tropopause, there are two areas with wind speeds exceeding 22m/s at dropsonde 4 and 5 between 600-500hPa, and at dropsonde 1 around 850hPa, which could be an upper and lower-level jet, respectively. The wind speed is generally higher on the western side of the cross section. The very high wind speeds over 40m/s in addition to the high potential temperatures is probably connected to the very high PV-values found above the polar low in the ECMWF-analysis.

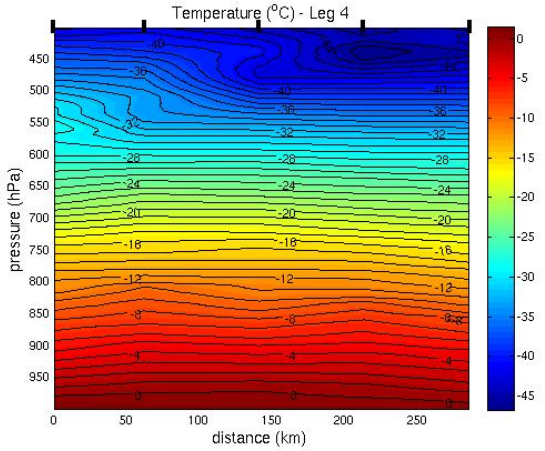

(a) Temperature in Celsius.

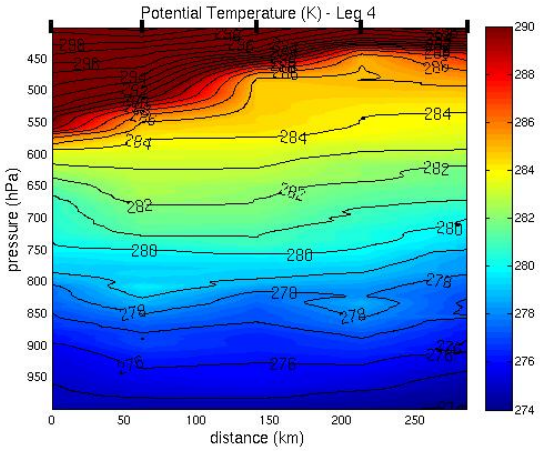

(b) Potential temperature in Kelvin.

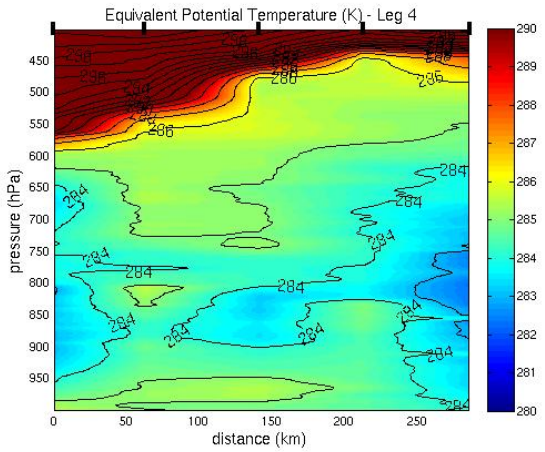

(c) Equivalent potential temperature in Celsius.

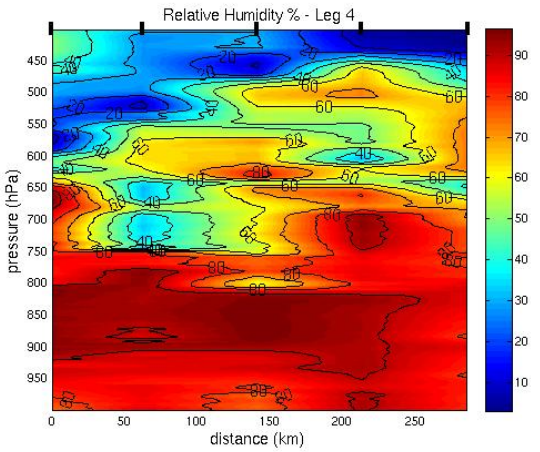

(d) Relavtive Humidity in %.

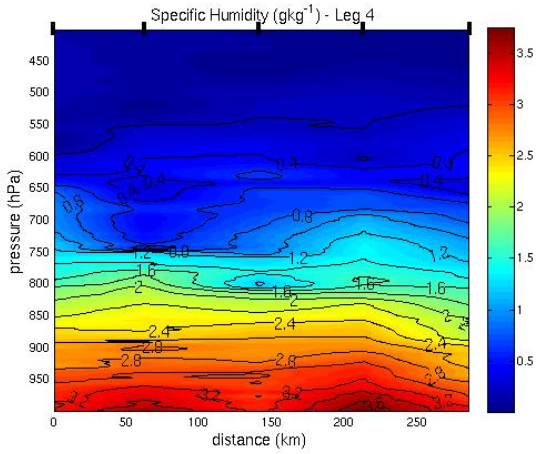

(e) Specific Humidity in g/kg.

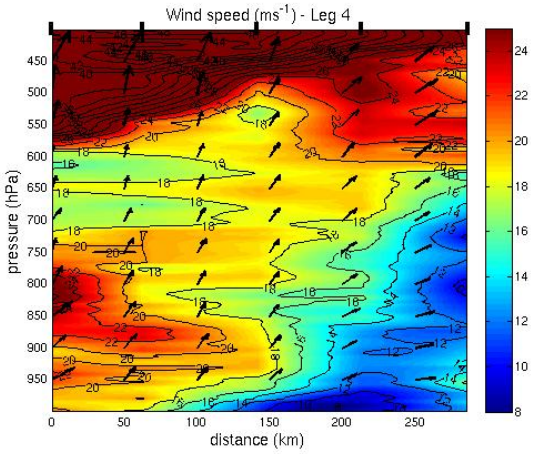

(f) Wind speed in m/s.

Figure 4.16: Results from cross section D. West (dropsonde 1) is to the left in the figures, and east is to the right (dropsonde 5). The black dots on top of each frame marks the dropsondes.

Chapter 5

Results and discussion

The purpose of this chapter is to present the results from the WRF simulations, evaluate these and compare them to the operational HIRLAM-forecast for March 16-17. To be able to do so, the first part of the chapter is devoted to evaluating the HIRLAM-prognosis, before the different WRF-simulations are presented in the following sections. Conclusions and further work will be discussed in the last part of the chapter.

All the results from HIRLAM are presented using the meteorological visualisation and production software, Diana[1], developed by DNMI. Output from the WRF model has been processed and visualized in NCL[2]. The figures presented here are from the second domain in the WRF model, as described in chapter 3.

5.1 The HIRLAM weather forecast for March 16-17

One of the main factors that made this particular polar low so interesting is the fact that is was poorly forecasted. A main objective of this study is to check if WRF can perform better than the operational HIRLAM-model. To be able to perform a comparison, an analysis of the HIRLAM-forecast first must be made. Forecasts for March 16-17 with four different initial times have been studied, and are presented in the following section.

[1]https://diana.wiki.met.no/doku.php

[2]NCAR Command Language. See more info on: http://www.ncl.ucar.edu/

5.1.1 Initial time 0000 UTC on March 15

The first model run considered here was initialized at 0000 UTC March 15. At 0100 UTC on March 16, the trough is present at the approximately correct position according to the satellite image and there appears to be a weak low at the north-west end of the trough, at 75°N and 4°W, close to V3 described in chapter 4. There could also be some development in the middle of the trough, north-west of the cluster of high cumulus clouds at 73°N and 5°E. From 0100 to 0300 UTC, this area of disturbance develops into a small low with minimum pressure of 1002hPa, while the northernmost low weakens. However, by 0600 UTC both disturbances have weakened and are no longer evident in the prognosis. After 0900 UTC a small low is visible close to V1. This low appears on and off on the prognosis, but does not develop any further. Figure 5.1(a) shows the surface pressure at 1200 UTC on March 16. There are no clear lows in the figure, but an extension of the trough is found at 70.5°N and 7.5°E, southwest of the low seen in the satellite image. After 1800 UTC March 16 through to the end of the prognosis, there is no low pressure activity visible in the vicinity of the real polar low.

5.1.2 Initial time 1200 UTC on March 15

The next model run was initiated 12 hours later. Two small lows are visible at 74°N, 5°E and near the coast of Troms, Norway at 70°N and 15°E at 0100 UTC. The minimum pressure of the two lows are 1003hPa and 1001hPa, respectively. The former of the two lows is still visible in the prognosis from 0600 UTC, but dissipates shortly after. At 1200 UTC (figure 5.1(b)), there are no lows present, but a new low forms right afterwards just next to V1, at 71°N and 11°E, with a minimum pressure of 999hPa. This low develops further and follows the approximate path of the real low until 1800 UTC. Later, the low moves in a more south-westerly direction, compared to the real low. The low is visible in the prognosis until 0600 UTC on March 17, before it dissipates without making landfall.

5.1.3 Initial time 0000 UTC on March 16

At 0600 UTC in the prognosis initialized at 0000 March 16, there are no evident low pressure systems in the area of interest. At 1200 UTC (figure 5.1(c)), there is a small and weak low just outside the coast of Troms, at 71°N and 16°E, some 100km east of the real low. This low has a minimum pressure of 998hPa. six hours later the low remains weak, but its position is now closer to the real polar low at 71°and 12°. However, a few hours after

this the prognosis shows that the low dies out without making landfall.

5.1.4 Initial time 1200 UTC on March 16

The last prognosis considered in this study was initialized at 1200 UTC March 16, mainly to look at the movements and strength of the mature low. At 1500 UTC, the low is not yet well defined, but a low pressure area with minimum pressure of 999hPa covers part of the area where the real low is situated at the time. At 2100 UTC the low has weakened, and the pressure is 1001hPa at the minimum, but better defined in the pressure field. However, the forecast places the low too far south-east and miss out the real low, as seen in figure 5.1(d) from 0600 on March 17, where the prognosis has placed the low at 65°N and 7.5°E, whereas the real low was stationed at 66.5°N and 7.5°E. This trend continues throughout the night, and the prognosis forecasts that the low would make landfall around 1100 UTC on March 17, an hour too early.

5.1.5 Evaluation of the HIRLAM-prognosis

None of the HIRLAM-prognosis considered performed very well. Only one of the prognosis initialized before the polar low developed, produced a clear polar low, six hours later than the real low developed. It is interesting to note that the best forecast was not made by the prognosis that was initialized closest in time to the development of the low, but the one initiated 12 hours before cyclogenesis. This could suggest that the model spin-up affected the simulation initiated at 0000 UTC on March 16. But even the best prognosis failed to forecast the movement of the low, and most importantly, if and where the low would make landfall.

5.2 Different initial times

In order to investigate how to best simulate this particular low, several sensitivity experiments were carried out. The main groups of these are different initial time experiments, horizontal resolution experiments and different parametrization schemes for microphysics, convective clouds and planetary boundary layer. For details on the different experiments, see chapter 3.

The polar low was simulated with several different initial times, from 72

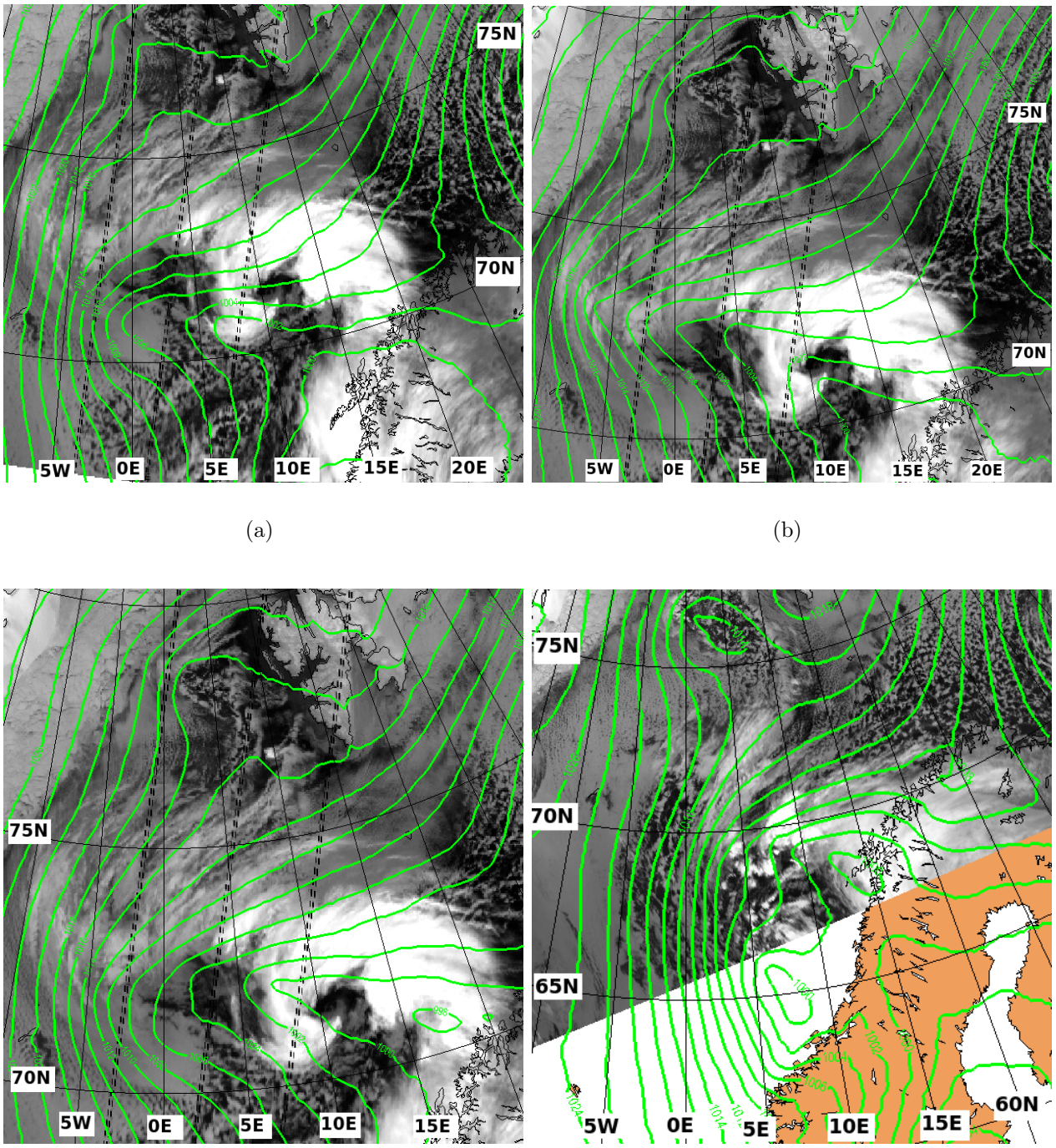

Figure 5.1: FY1D NOAA 4 IR-satellite image at 1210 UTC on March 16, and the HIRLAM prognosis of surface pressure at 1200 UTC on March 16 initiated at a) 0000 UTC on March 15, b) 1200 UTC on March 16, c) 0000 UTC on March 16. d) The NOAA-18 NOAA 4 IR-satellite image at 0557 UTC on March 17, and the HIRLAM prognosis of surface pressure at 0600 UTC on March 17, initiated at 1200 UTC on March 16. Contour lines are 2hPa.

hours prior to cyclogenesis (0000 UTC March 16) to 24 hours after this. The simulations are divided into three groups: One for simulations initiated more than 24 hours before cyclogenesis (long lead-time), one for simulations initiated less than 24 hours before cyclogenesis (short lead-time), and one group for simulations initiated after cyclogenesis.

5.2.1 Long lead-time simulations

Initialization 0000 UTC on March 13

The first model run was initialized at 0000 UTC on March 13, and the results are shown in figure 5.2, which show surface pressure and wind fields at 0600, 1200, 1800 UTC on March 16 and 0600 UTC on March 17. It was not expected that a simulation would be able to produce a good polar low forecast this long in advance. At 0000 UTC on March 16 (not shown) there is a clear trough leading from the coast of Troms and north-westward in between Svalbard and Greenland, but no clear low. And at 0600 UTC, seen in figure 5.2(a), when the ECMWF-analysis shows clear polar low development around 71.5°N and 16°E, there are still no signs of development within the domain.
It remains so until 0800 UTC, when a small low develops close to the coast of Troms and Nordland. By 1200 UTC, shown in figure 5.2(b), the low has travelled to the west and is now stationed at 68°N and 9°E with a minimum pressure of 996hPa. Wind speeds exceed 20 m/s on the low's western side. From 1200 to 1800 UTC the low moves southwards and strengthens further. Figure 5.2(c) shows the surface pressure and wind at 1800 UTC on March 16. The minimum pressure is now 994hPa, and the low is stationed at 65.5°N and 9°E. The low makes landfall between Nordland and Trøndelag only a few hours after this between 20 and 22 UTC and dissipates over land in the morning hours of March 17. During the day of March 17, only a single low south-west of Spitsbergen develops and figure 5.2(d) from 0600 at March 17 shows no low pressure activity in the vicinity of the real polar low.
As expected, this model run did not perform very well. It forecasted that one polar low would develop close to the coast of Northern Norway, but not at the right time or in the vicinity of the real polar low. However, it did predict that the chances of polar low development were high, and also that there was a chance that the polar low would hit land in the same area as the real polar low did. This is enough to alert the forecasters that a polar low could develop around this time. It should be noted that the low that appeared south-west of Svalbard in the later part of the simulation is also present in the ECMWF-analysis at 0600 UTC on March 17 at the exact same location and with the same minimum pressure. This is very impressive for a forecast initiated four days in advance! This could indicate that differences in the

character of the two lows hold the key to why the first one was so difficult to forecast.

Initialization 1200 UTC on March 14

The next model run was initiated at 1200 UTC on March 14, and the results are shown in figure 5.3. This run shows polar low development already at 0000 UTC March 16 (not shown) at 71.5°N and 10°E, north-west of the real polar low. However, this low is weak and dissipates shortly after. At 0600 UTC a new low has developed around 70.5°N and 7°E with minimum pressure of 999hPa (figure 5.3(a)).
Around 0800 UTC (not shown) there are suddenly three small lows in the same region. The two new lows are quite weak and after four hours only the easternmost one is evident at 70°N and 15°E in figure 5.3(b), which shows the results at 1200 UTC. The first low has travelled southwards and deepens with a minimum pressure of 998hPa. During the next couple of hours, the trend continues. The second low vanishes, and the first strengthens and moves further southwards. At 1800 UTC the low is centered at 66.5°N and 8°E, outside the coast of Nordland, with the same minimum pressure as before, but with stronger pressure gradients. This is seen in figure 5.3(c). In the next few hours the low travels further southwards at a much greater speed than the real low and begins to weaken. The low makes landfall at the coast of Trøndelag near midnight on March 17, 12-14 hours before the real low. A new low develops off the coast of Nordland and can be seen at 66.5°N and 11.5°E, in figure 5.3(d) from 0600 UTC on March 17. The low south-west of Spitsbergen is also present in this image.
This forecast did better than the first one. It managed to produce a polar low in the vicinity of the real low, although 6 hours later and 9°too far west. Its trajectory resembled the real lows trajectory, but it travelled too far west and too fast to the south so that the low hit land 12-14 hours earlier than the real low did. But as a whole, this was a relatively good performance for a model run made 42 hours in advance of cyclogenesis.

Initialization at 0000 UTC on March 15

Figure 5.4 shows the results from the WRF simulation initiated at reference time at 0000 UTC on March 15. At 0000 UTC March 16 (not shown), a weak low is already present at 73°N and 7°E in the middle of the surface trough close to V2 (see the analysis in chapter 4), with a minimum pressure of 1001hPa. There is also a weak low off the coast of Troms at 71°N and 17°E, where the real low develops, this too with a minimum pressure of 1001hPa.

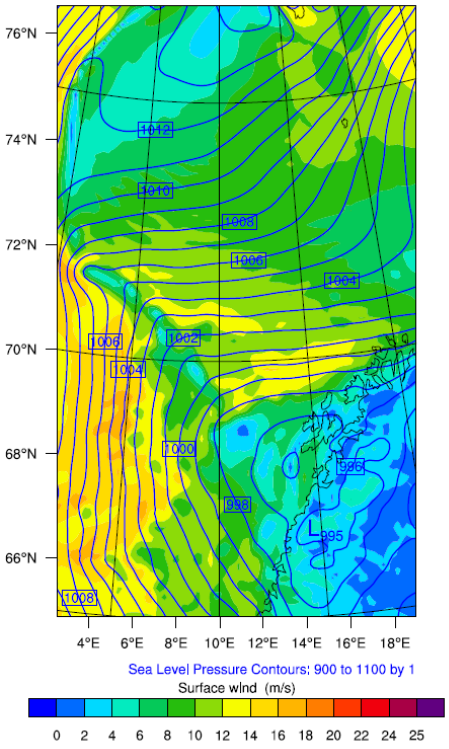

(a) 0600 UTC March 16.

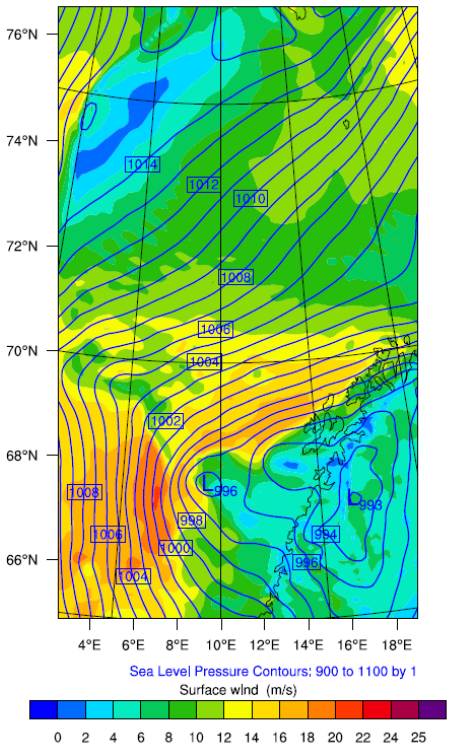

(b) 1200 UTC March 16.

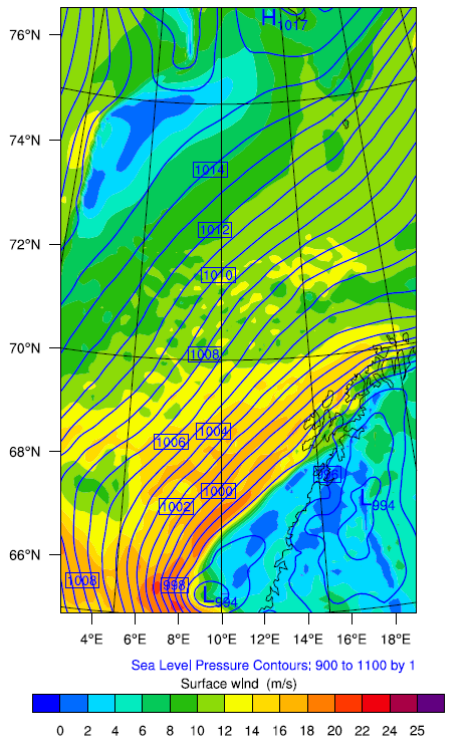

(c) 1800 UTC March 16.

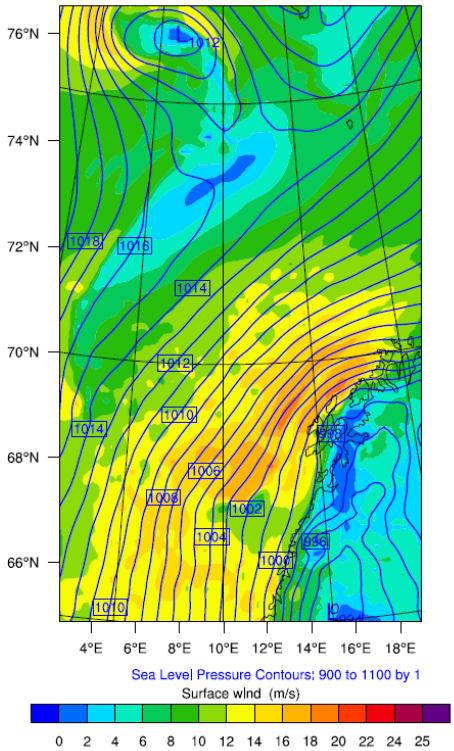

(d) 0600 UTC March 16.

Figure 5.2: Surface pressure and wind fields from the WRF simulation initiated at 0000 UTC on March 13.

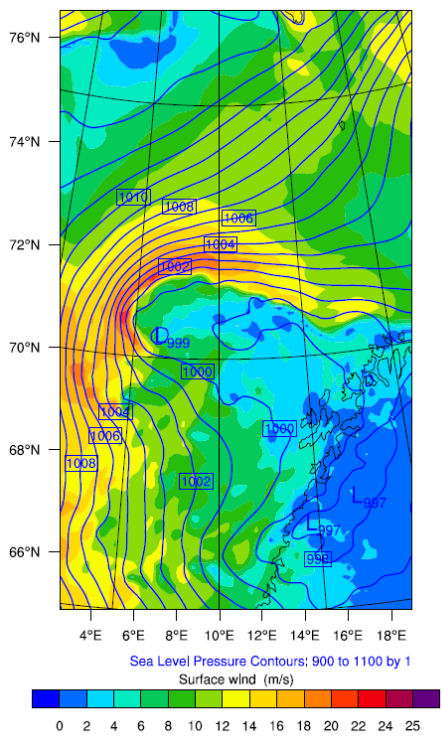

(a) 0600 UTC March 16.

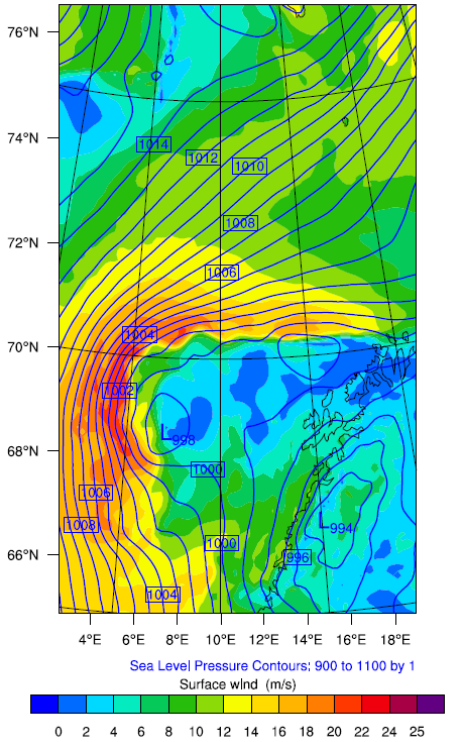

(b) 1200 UTC March 16.

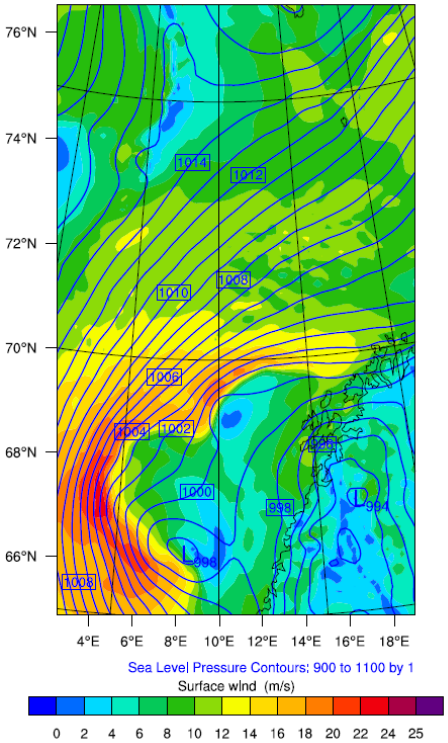

(c) 1800 UTC March 16.

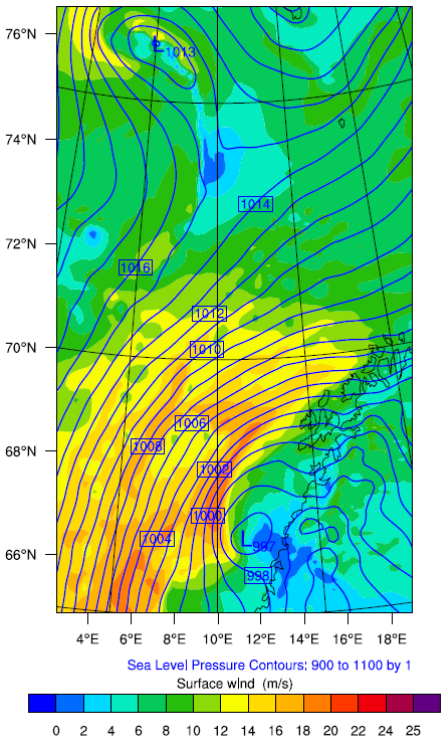

(d) 0600 UTC March 17.

Figure 5.3: Surface pressure and wind fields from the WRF simulation initiated at 1200 UTC on March 14.

Henceforth, these will be referred to as L1 and L2, respectively.
The movement of L1 is quite rapid southwards, while L2 travels slightly to the west in the next few hours. At 0600 UTC shown in figure 5.4(a), L1 is visible at 72°N and 8°E. L2 is now stationed at 71°N and 15°E, just west of the real low. In the next couple of hours, L1 travels rapidly southwards, while the movement of L2 is still westward. At 1200 UTC shown in figure 5.4(b), L1 is stationed at 69°N and 7°E and L2 at 71°N and 12°E. The minimum pressure of the lows are 999hPa and 997hPa, respectively. The movement and position of L1 is too far to the south-west, but L2 is positioned almost precisely where the real polar low is at 1200 UTC.
In the time period between 1200 and 1800 UTC, L1 continues to move southwards and also deepens, and is still too far south compared to the real polar low. L2 continues westward, but also southwards and is stationed at 70°N and 7.5°E, as seen in figure 5.4(c), exactly where the real polar low is centered at the time. The strength of L2 is now 998hPa, and it appears smaller in extent than L1 which is very evident in the figure.
This is unfortunately also the trend during the rest of the time period. L2 has the approximate path of the real polar low, but weakens through the night of March 17 and dissipates without reaching land. L1 continues on its path southwards and hits the coast of Trøndelag too far north and too early compared with the real low, at 06 UTC March 17. The minimum pressure of the low while making landfall was 997hPa, with winds of 20m/s following in its path. Figure 5.4(d) shows this.
All in all, this was a fairly good forecast. It produced two polar lows, with one following almost the exact path of the real one, which is very good for a model simulation initiated 30 hours in advance. There might have been some problems regarding the interaction between the two lows, since they were so close. As seen in the satellite images in chapter 4, there are also other vortices present when the polar low starts to develop, so the fact that this model produced several lows is not so surprising. It seems that the model underestimated the strength of L2, while it overestimated L1.

Evaluation of the long lead-time simulations

In order to give a better overview of the performance of the simulations, the positions and minimum pressures of the polar low in each run, along with the results from the ECMWF-analysis given in chapter 4, have been summarized in table 5.1. If there were several lows in the simulation, the one closest in position to the real low has been chosen, for instance L2 has been chosen for WRF1500. Undoubtedly, this will give an advantage to the simulations that produced several lows, and the ECMWF-analysis does not necessarily provide the right positions and minimum pressure of the real low. Therefore the table must be interpreted with caution.

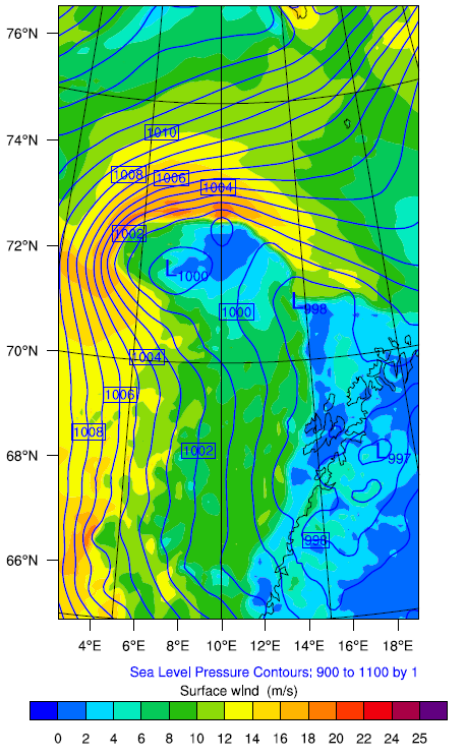

(a) 0600 UTC March 16.

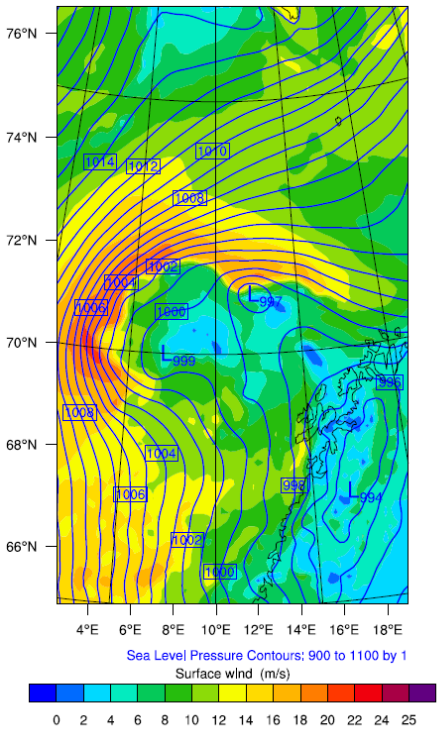

(b) 1200 UTC March 16.

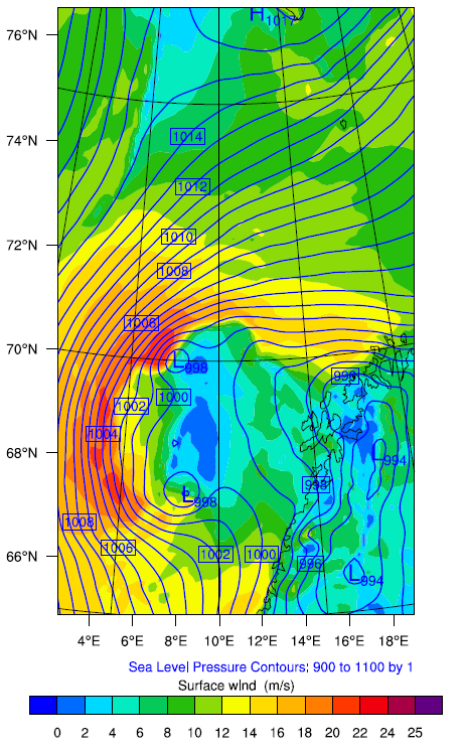

(c) 1800 UTC March 16.

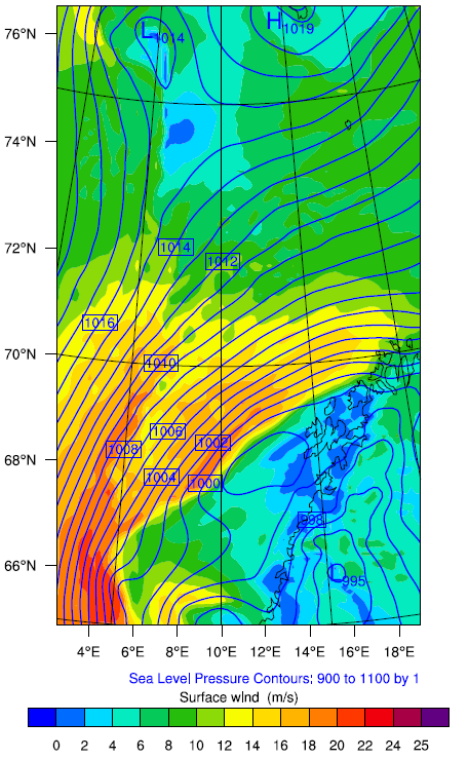

(d) 0600 UTC March 17.

Figure 5.4: Surface pressure and wind fields from the WRF simulation initiated at 0000 UTC on March 15.

The results of each run were very different. The first run was only adequate to give a warning that a polar low could develop, and the second had a similar, but slightly too far westward trajectory compared to the real low. The third simulation developed in the right area and followed closely the trajectory to the real low the first 18 hours, but traveled too fast southwards and dissipates without making landfall. Minimum pressure was generally 1-3hPa too high in the last two runs. WRF1300 produced a stronger low, with minimum pressure of 994hPa at 1800 on March 16. One possibility is that this low developed over warmer waters, and therefore became stronger. It is still a fairly good result for the long lead-time simulations, compared to the operational HIRLAM-prognosis initiated on March 15, that did not manage to produce a well defined low at all.
One interesting remark is the fact that even though the results for the polar low on March 16-17 differed a lot, the polar low that developed during the night of March 17 was well captured by all the long lead-time simulations. This suggests that the 16-17 March polar low was particularly difficult to forecast.

5.2.2 Short lead-time simulation

Initialization at 1200 UTC on March 15

In figure 5.5, the results from the WRF simulation initiated at 1200 UTC March 15, are presented. Around midnight on March 16 (not shown), a small low (L1) is present near 75°N and 5°E, with a minimum pressure of 1003hPa. This is at the north-western end of the trough and close to where V1 can be found on the satellite image presented in chapter 4. During the next few hours L1 moves to the south-west, and is on its way out of the western edge of the domain at 0600 UTC, seen in figure 5.5(a) at 74°N and 4°E. After this, the low continues westwards, weakens and dissipates (for the time being) just before 1200 UTC. There is no activity of interest within the domain at 1200 UTC (figure 5.5(b)). It remains so until 1400 UTC when another low, (L2), develops at 72°N and 8°E, also at the end of the trough. L2 deepens, and follows the direction of L1 towards south-west. At 1800 UTC, L2 is stationed at 71°N and 5°E, with a minimum pressure of 1002hPa. In figure 5.5(c) from 1800 UTC, L1 reappears south of the second low at 68.5°N and 3°E now with a minimum pressure of 1005hPa. Throughout the next hours L2 remains at the same intensity, while L1 strengthens significantly and at 0000 UTC on March 17 the minimum pressure has decreased to 1001hPa. After this, L2 starts to move southwards with increasing speed and is strength. L1 continues southwards and disappears out of the inner domain between 0400 and 0600 UTC. L2 can be found at 66.5N and 4E, with a minimum pressure of 1002hPa in figure 5.5(d) from 0600 UTC on March 17. It can be seen in the outer domain that the two lows are almost at the same latitude, when L1

Time (UTC)	Position ECMWF analysis	Position WRF1300	Position WRF1412	Position WRF1500	Min. surface pressure ECMWF (hPa)	Min. surface pressure WRF1300 (hPa)	Min. surface pressure WRF1412 (hPa)	Min. surface pressure WRF1500 (hPa)
0000 March 16	70N 17E	-	-	71N 17E	1000	-	-	1001
0600 March 16	70.5N 16E	-	70.5N 7E	71N 14.5E	997	-	999	998
1200 March 16	72N 11E	68N 9E	68.5N 7.5E	71N 12E	996	996	998	997
1800 March 16	70.5N 7.5E	65.5N 10E	66.5N 8E	70N 7.5E	995	994	998	998
0000 March 17	69N 7E	-	67N 8E	67N 6E	996	-	999	999
0600 March 17	66.5N 7.5E	-	66.5N 11.5E	-	996	-	997	-
Landfall	63.5N 10E	64N 10E	-	-	time: 1200 March 17	time: 2200 March 16	-	-

Table 5.1: Minimum surface pressure and position of the polar lows in long lead-time simulations.

makes landfall at the coast of Trøndelag around 0800 UTC, but as L2 follows in the wake of this, it does not appear to bring strong winds. The strong winds come after L2 hits land at the coast of the western part of Norway at 62°N and 7°E, between 1000 and 1200 UTC on March 17.

It is surprising to note that this simulation performed worse than the previous one initiated 12 hours earlier. It did not forecast any development in the right region around 0000 UTC on March 16. Polar low development was expected, and L1 did develop close to V1. L2 developed 12°further west than the real polar low, and 14 hours later. This low also remains quite weak throughout the period of time. The paths of the lows are too far east and their movements are too rapid southwards. In total, this was a very weak performance of a run initiated only 12 hours before cyclogenesis.

It is possible that model spin-up time affected this simulation.

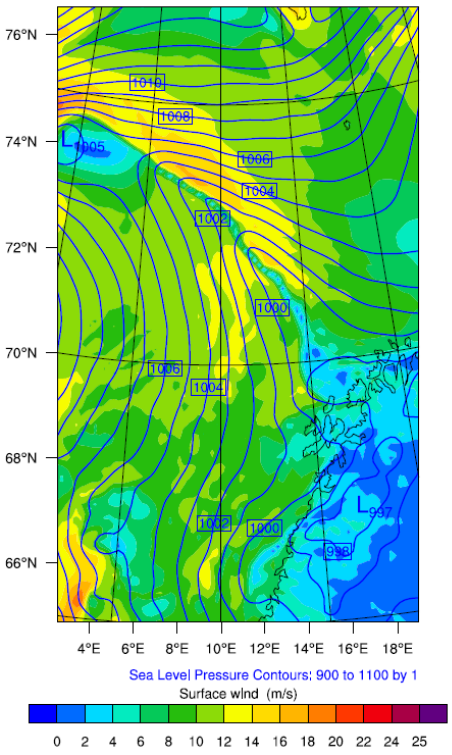

(a) 0600 UTC March 16.

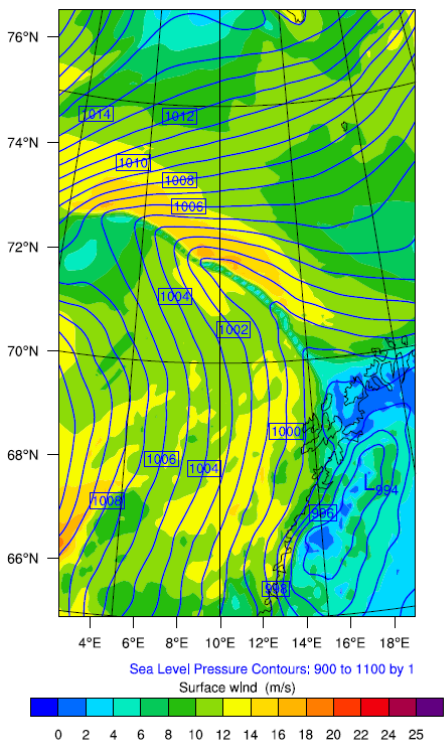

(b) 1200 UTC March 16.

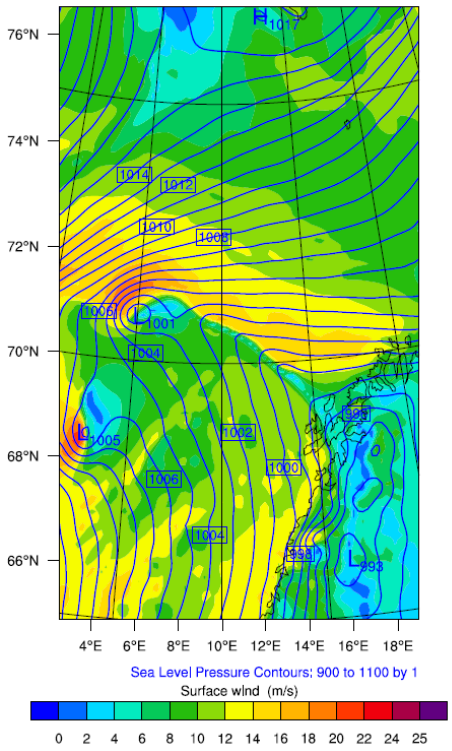

(c) 1800 UTC March 16.

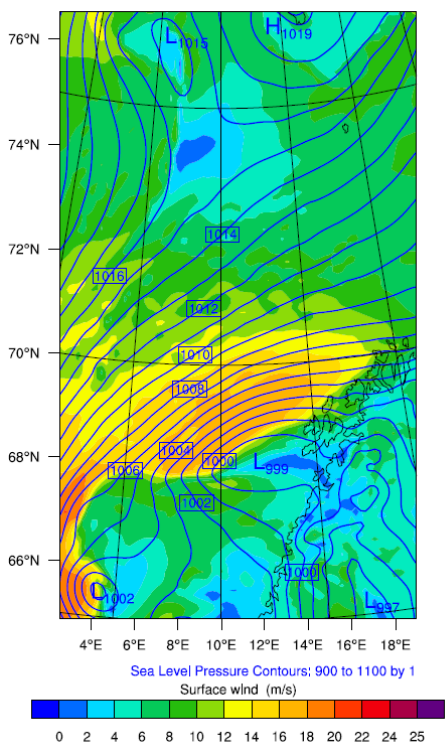

(d) 0600 UTC March 17.

Figure 5.5: Surface pressure and wind fields from the WRF simulation initiated at 1200 UTC on March 15.

Initialization at 1800 UTC on March 15

The results from the model run initiated at 1800 UTC on March 15 are shown in figure 5.6. A small low, L1, is present at 0000 UTC on March 16 (not shown), at 75°N and 4°E with minimum pressure of 1001hPa. This is at the end of the surface trough and close to V3, just as L1 in the previous section. Another small low, L2, is situated just outside the coast of Troms at 71°N and 15°E, with a minimum surface pressure of 999hPa, close to the real polar low. There is also a third small low, L3, present at 68°N and 3°E. In the next 6 hours, L1 moves out of the domain, L3 moves southwards and weakens, and L2 deepens to 998hPa and remains almost stationary, as seen in figure 5.6(a) from 0600 UTC.
At 1200 UTC (figure 5.6(b)), L2 is the only one of the original lows still visible in the surface pressure field, at 71.5°N and 11°E, still close to the real low. A new low has developed north-east of L2 at 72°N and 4°E, but this low dissipates shortly after. At 1800 UTC (figure 5.6(c)), L2 has moved south-eastward and is now stationed at 67.5°N and 4°E. L2 has weakened and the minimum pressure is now 1001hPa. Once more another low has developed, this time at 70°N and 7.5°E, also with a pressure minimum of 1001hPa. But even this low vanishes after a couple of hours, while yet another polar low develops just outside the coast of Nordland in the early morning hours of March 17. L2 continues to travel southwards and strengthens somewhat before making landfall at 0800 UTC on March 17. The newest low travels south-westward and is stationed outside the southern parts of Nordland, when the simulation ends.
This model run produced a lot of small lows, but only L2 was significant and lasted for longer than a couple of hours. L2 developed close to the real polar low and had a similar trajectory as well. Unlike many of the other simulations that predicted an early move towards the south, this run forecasted that the low would remain at latitudes higher than 70°during the first half of the period, before heading south after 1800 UTC. L2 made landfall a couple of hours too early, although still in the right area.

Initialization at 0000 UTC on March 16

The third and last run in the series of model runs initiated within this time interval, was initiated at 0000 UTC on March 16. The results from this simulation are shown in figure 5.7.
At 0600 UTC (figure 5.7(a)) a small low with minimum pressure of 997hPa, is present at 71°N and 15°E, quite similar to the real low. There are also some remains of another low near the north-western edge of the surface trough at 73.5°N and 0°E, but this vanishes shortly thereafter. Around 1000 UTC another low develops at 71°N and 16°E, where the first low also developed.

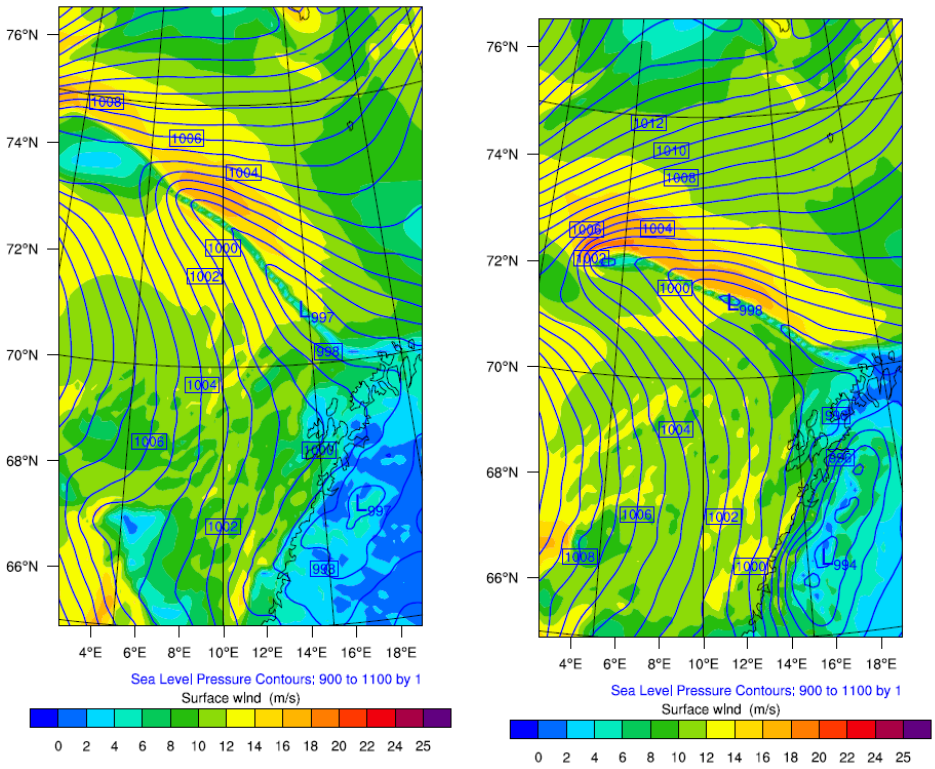

(a) 0600 UTC March 16.

(b) 1200 UTC March 16.

(c) 1800 UTC March 16.

(d) 0600 UTC March 17.

Figure 5.6: Surface temperature, pressure and wind fields from the WRF simulation initiated at 1800 UTC on March 15.

Figure 5.7(b) shows the surface wind and pressure fields at 1200 UTC on March 16. The first low, now referred to as L1, has travelled towards the north-west and is stationed at 72°N and 12°E, still following the path of the real polar low. The second low, L2, remains stationary. Both of the lows have 997hPa as minimum pressure.
During the next couple of hours, both of the lows travel westwards and L1 towards the south as well. At 1800 UTC the two lows have weakened to 998hPa, as seen in figure 5.7(c). L2 is stationed at 71°N and 14°E, while L1 is at 70°N and 5°E. L1 still stays close to the path of the true polar low, but is now a bit too far to the west. L2 has lost some of its characteristic pressure gradients, and continues to weaken during the hours afterwards. At 0000 UTC on March 17 (figure 5.7(d)), there are no traces of L2. L1 has by then travelled far south, and the center of the low is now placed at 67°N and 5°E. The pressure minimum remains the same, but the pressure gradient has sharpened a bit, at least on the eastern and southern side. L1 continues southwards and makes landfall around 1000 UTC at the coast of Trøndelag. During the morning hours before making landfall, L1 strengthens significantly and hits land as a well defined low with a minimum pressure of 995hPa.
This run was initiated at cyclogenesis and could therefore have some problems related to model spin-up time. It managed to produce a low close to where the low developed, and the relative strength of it was also very similar to the real low. The trajectory was similar to the real low during the first half of the period, but the low travelled too far west and too fast to the south during the second half. The model forecasted another small low following in the wake of the first one for some time. There are no indications that this happened in the analysis, but since the forecasted low L2 was so small and only lasted for a couple of hours, it can not be ruled out.
Finally, the most important aspect of the model run is whether, where and when the low will make landfall and was satisfactory modelled in this run. L1 deepened and made landfall in the right area, and only a few hours before the real low did. Therefore, the conclusion must be that this is a very good simulation.

Conclusion on the short lead-time simulations

As in the previous section, the positions and surface pressure minimums of the low in each simulation are listed in table 5.2. For simulation WRF1518 and WRF1600, the lows closest in position to the real low have been chosen. This means L2 for WRF1518 and L1 for WRF1600. The ECMWF-analysis is also given in this table for easier comparison. The results from the short lead-time simulations were very different, even though these are initiated closer to cyclogenesis and within a much shorter time interval. A common feature

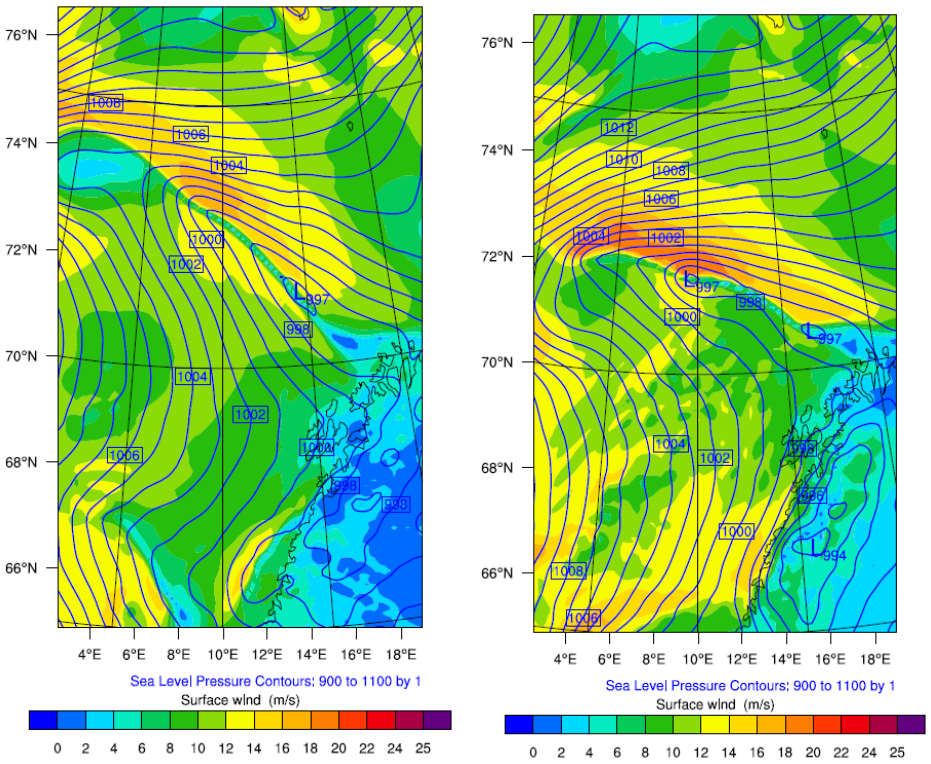

(a) 0600 UTC March 16.

(b) 1200 UTC March 16.

(c) 1800 UTC March 16.

(d) 0000 UTC March 17.

Figure 5.7: Surface pressure and wind fields from the WRF simulation initiated at 0000 UTC on March 16.

is that all of the simulations placed the trajectory too far west. These simulations also tend to produce multiple small lows. The WRF1518 simulation produced as many as 6! The minimum pressures of the lows were generally too high. The low in WRF1512 never got under 1001hPa, while WRF1518 and WRF1600 had lows with minimum pressures generally 2-3hPa too high. The short lead-time simulations did not perform significantly better than the long lead-time ones. This is surprising, as an improvement would be expected. As mentioned earlier there could be some problems regarding the spin-up time, but it is conspicuous that the simulation with the longest lead time performed worst.
Once again it is interesting to note the low south-west of Spitsbergen, which is present at almost the exact same location in the frames from 0600 UTC on March 17. It can be suggested that the 16-17 March low was very special in character compared with the Spitsbergen low. And that this factor is affecting all of the simulations, regardless of initial time.

5.2.3 Simulation after cyclogenesis

Initialization at 1200 UTC on March 16

The last set of model runs was made after cyclogenesis had taken place and mainly to forecast the strength and the path of the polar low. The results from the first of the two runs are shown in figure 5.8. This run was initiated at 1200 UTC on March 16, when the polar low already had developed and was clearly evident in the ECMWF-analysis at 72°N and 11°E.
This model run stands out in comparison with the previous runs in that the low is well defined and stronger than the others at 1800 UTC on March 16, as seen in figure 5.8(a). The minimum surface pressure is 995hPa, with strong temperature gradients on both sides, particularly on the western side. The low is stationed at 71.5°N and 6°E, also this time further west than the real polar low. During the next few hours the low travels further south-west and maintains its strength. At 0000 UTC on March 17 (figure 5.8(b)), the low is positioned at 69°N and 5°E, still 2°too far west. The strength of the low remains the same throughout the morning hours, and the low continues to move southwards. At 0600 UTC (figure 5.8(c)), the position of the low is 66°N and 6°E, still 2°too far west of the real low.
So far there have been no other lows present within the domain, but now a low has developed near the coast of northern-Nordland. This low is quite insignificant compared to the first low, and also dissipates after a few hours. At 1200 UTC the first low makes landfall at the coast of Trøndelag, after deepening during the morning hours.
It could seem that the WRF-model has trouble simulating the rapid strengthening of the low during the first half of the polar low's life cycle. Previous runs did not manage to forecast the depth of the low, but when this was

Time (UTC)	Position ECMWF analysis	Position WRF1512	Position WRF1518	Position WRF1600	Min. surface pressure ECMWF (hPa)	Min. surface pressure WRF1512 (hPa)	Min. surface pressure WRF1518 (hPa)	Min. surface pressure WRF1600 (hPa)
0000 March 16	70N 17E	-	70.5N 15E	-	1000	-	999	-
0600 March 16	70.5N 16E	-	71N 15E	71.5N 15E	997	-	997	997
1200 March 16	72N 11E	-	71.5N 11.5E	72N 12E	996	-	998	997
1800 March 16	70.5N 7.5E	71N 5E	70.5N 5.5E	70N 5E	995	1001	999	998
0000 March 17	69N 7E	68.5N 4E	67.5N 4E	67N 5E	996	1003	1001	998
0600 March 17	66.5N 7.5E	66.5N 4E	65N 8E	64.5N 8E	996	1002	998	996
Landfall	63.5N 10E	62N 7E	65N 8E	63N 9E	time: 1200 March 17	time: 1200 March 17	time: 0800 March 17	time: 1000 March 17

Table 5.2: Minimum surface pressure and position of the polar lows in the short-lead time simulations.

already given the model performed much better. This run also forecasted a strengthening in the last few hours before landfall, and did not change the strength before this. There were very few other lows present within the domain during this run. It could be that the presence of a strong polar low inhibits development of other lows close to it. The run also managed to forecast the path of the low quite well, and it made landfall around 1200 UTC, about the same time as the real low did.

Initialization at 0000 UTC on March 17

Finally, the last model run was initiated at 0000 UTC on March 17, when the real low had reached mature stage and was stationed around 68.5°N and

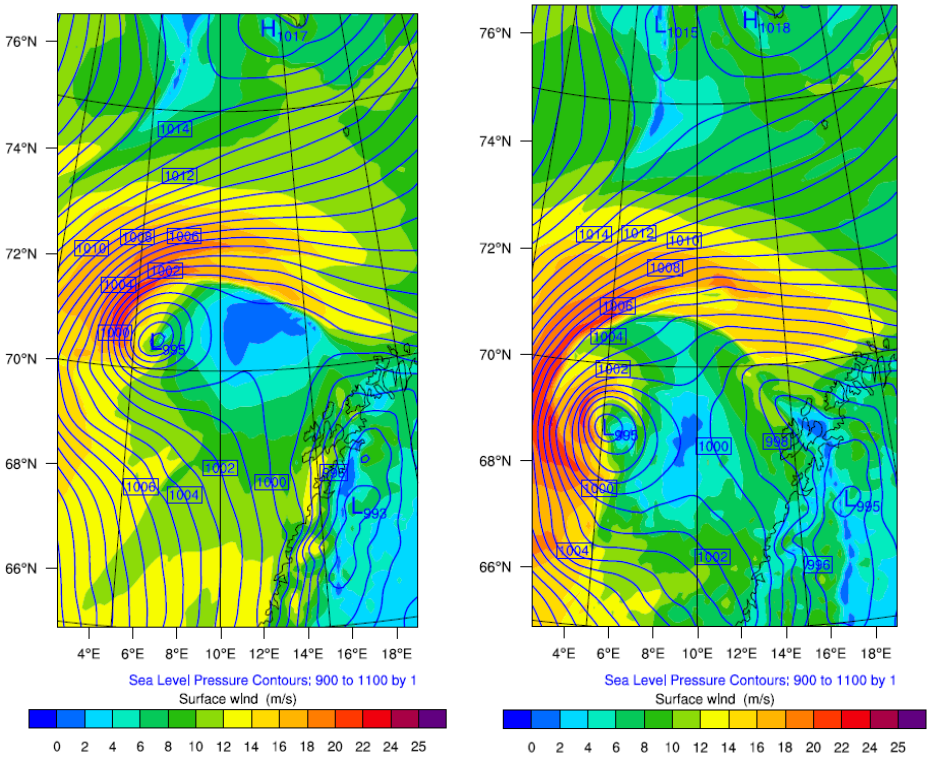

(a) 1800 UTC March 16.

(b) 0000 UTC March 17.

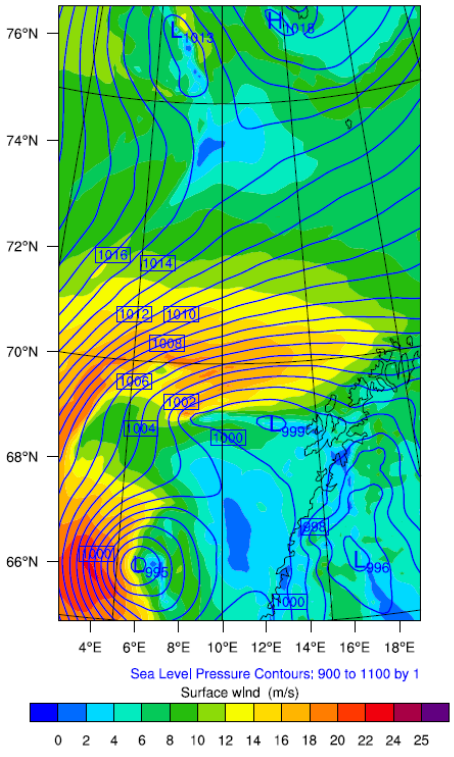

(c) 0600 UTC March 17.

Figure 5.8: Surface pressure and wind fields from the WRF simulation initiated at 1200 UTC on March 16.

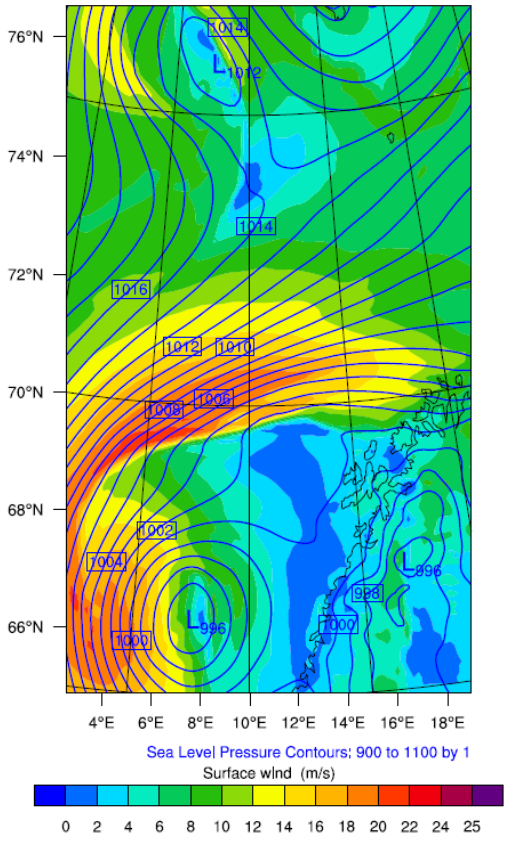

Figure 5.9: Surface pressure and wind fields at 0600 on March 17 from the WRF simulation initiated at 0000 UTC on March 17.

6.5°E. After this, the model forecasts that the low will continue to travel southward maintaining its strength and minimum pressure of 996hPa. At 0600 UTC, shown in figure 5.9, the low is positioned at 66°N and 8°E, relatively similar to the real low. The low makes landfall around 1200 UTC at the coast of Trøndelag. Unlike the previous model runs, this one did not forecast a strengthening of the low in the hours before making landfall, and had a trajectory very similar to the real low.

Conclusion on the post-cyclogenesis simulations

As with previous simulation sets, the results from this one are also summed up in table 5.3, along with the ECMWF-analysis. The rapid deepening of the low during cyclogenesis had already occurred when these simulations were initiated. The result of this is that both simulations had a minimum pressure much closer to the analysis than the other simulations. The trajectories were also more similar, but the WRF1612 simulations still placed the low too far west. Apparently, the improvements made by these simulations on depth and trajectories of the lows, are more to the fact that the low was already

Time	Position ECMWF analysis	Position WRF1612	Position WRF1700	Min. surface pressure ECMWF (hPa)	Min. surface pressure WRF1612 (hPa)	Min. surface pressure WRF1700 (hPa)
0000 March 16	70N 17E	-	-	1000	-	-
0600 March 16	70.5N 16E	-	-	997	-	-
1200 March 16	72N 11E	-	-	996	-	-
1800 March 16	70.5N 7.5E	70.5N 6E	-	995	995	-
0000 March 17	69N 7E	69.5N 5E	-	996	995	-
0600 March 17	66.5N 7.5E	66N 6E	66N 8E	996	995	996
Landfall	63.5N 10E	63N 9E	64N 10E	time: 1200 March 17	time: 1200 March 17	time: 1200 March 17

Table 5.3: Minimum surface pressure and position of the polar lows in the post-cyclogenesis simulations.

at its mature stage when they were initiated, and therefore did not have to simulate the difficult cyclogenesis stage.

5.2.4 Conclusion of the different initial times experiments

The simulations initiated at different times deviated much from each other, and the only set that managed to model the depth and trajectory of the low satisfactory was the set of simulations initiated after cyclogenesis. The long lead-time simulations performed reasonably well given the fact that they were initiated a long time in advance of cyclogenesis, but deviated much from each other as was expected. It was therefore surprising that also the short-lead

time simulations gave so different results, but this could be due to the model spin-up time.
It is worth noticing that all of the simulations predicted a low south-west of Spitsbergen at 0600 UTC on March 17, at approximately the same position. This provides a nice sanity-check of the runs and supports that the March 16-17 low had dynamics that made this particular low difficult to model.

5.3 High resolution simulations

High resolution modelling was tested out decreasing the horizontal grid spacing from 30km and 10km to 9km and 3km. Two different initial times were used, 0000 UTC on March 15 and 0000 on March 16. The runs are called WRF15HR and WRF16HR, respectively. We expect to see improved accuracy at the expense of the increased computational cost.

5.3.1 Simulation initiated at 0000 UTC on March 15

The results from WRF15HR initiated at 0000 UTC on March 15 are shown in figure 5.10. From midnight March 16, some small lows are present at the south-eastern end of the trough, but there is no clear development before 0600 UTC, when the northernmost low detaches itself from the rest of the trough, and moves in a north-westerly direction, as seen in figure 5.10(a). After a couple of hours at 1000 UTC, the next small low follows in the wake of the first, and moves away from the original trough.
The two lows continue westward and deepen. At 1200 UTC (see figure 5.10(b)), both lows are well defined and have a minimum pressure of 999hPa and 1000hPa.

The first and second low are stationed near 72°, and 6°E and 9°E, respectively. In the following hours, both lows continue to strengthen and to move westwards. The two lows seem to merge together, and at 1800 UTC (see figure 5.10(c)) there is only one low present. This is stationed at 71°N and 4°E, and has a minimum pressure of 1000hPa, quite far to the west of the real polar low. The low has now changed course to a southerly direction, which is in accordance with the real low. At 0600 UTC (figure 5.10(d)), the low has left the inner domain, and two small lows have developed off the coast of Nordland.
As most of the other runs, this one also forecasts that the low continues southwards and strengthens further during the morning hours on March 17. The low makes landfall at the coast of Trøndelag at 1000 UTC on March 17. The strongest coastal winds associated with this low are found just south-west of the center of the low, around Møre.

This simulation performed significantly worse than the previous model run initiated 24 hours before RT, which is very surprising. It did not produce a significant low before 1200 UTC on March 16, when there should be a clear low already by 0600 UTC. First, it produced two lows almost at the same time, but after a couple of hours they had merged together. The trajectory of the low was quite far to the west most of the time, as seen in many of the previous runs. Otherwise, the low does strengthen in the early morning hours like most of the other simulations, and makes landfall close to when and where the real low does.

5.3.2 Simulation initiated at 0000 UTC on March 16

The second high resolution run, WRF16HR, was initiated at 0000 UTC on March 16. The results are illustrated in figure 5.11. At 0600 UTC (figure 5.11(a)), there is a small low at 71°N and 15°E. The low remain quite weak throughout the night with no further development until 0800 UTC, when the it starts to become more organized. During the next couple of hours, the low continues to strengthen, and moves rapidly to the northwest, detaching itself from the rest of the trough.
In figure 5.11(b) (1200 UTC), the simulated low is stationed at 72°N and 8°E, when the real low was stationed at 71.5°N and 10.5°E at the same time. Minimum pressure is 996hPa. The low turns in a south-westerly direction and is located at the western edge of the domain at 1800 UTC (figure 5.11(c)). A couple of small lows have appeared during this time interval. Among them is a low south of the developed low, at 68.5°N and 5.5°E. Around 2200 UTC on March 16, the two lows start to merge together, and the new low continues in a south-easterly direction.
The low deepens before it divides itself into two separate lows at 0600 UTC on March 17, and travels out of the inner domain, as seen in figure 5.11(d). The deepest part of it continues towards the coast of Norway relatively fast, while the other part is somewhat slower and weakens. At 1000 UTC, the first and strongest part of the low hits the coast of Trøndelag, a couple of hours before the real low does. The minimum pressure of the low before making landfall is 993hPa (around 0800 UTC).

Also the WRF16HR did not perform any better than the corresponding coarse grid run. While WRF1600 produced a clear low at 0600 UTC, this run did not follow until 1200 UTC, and its trajectory was too far west. Both runs forecasted the low to make landfall at the coast of Trøndelag around 1000 UTC. The depth of the WRF16HR low deviated less from the real low

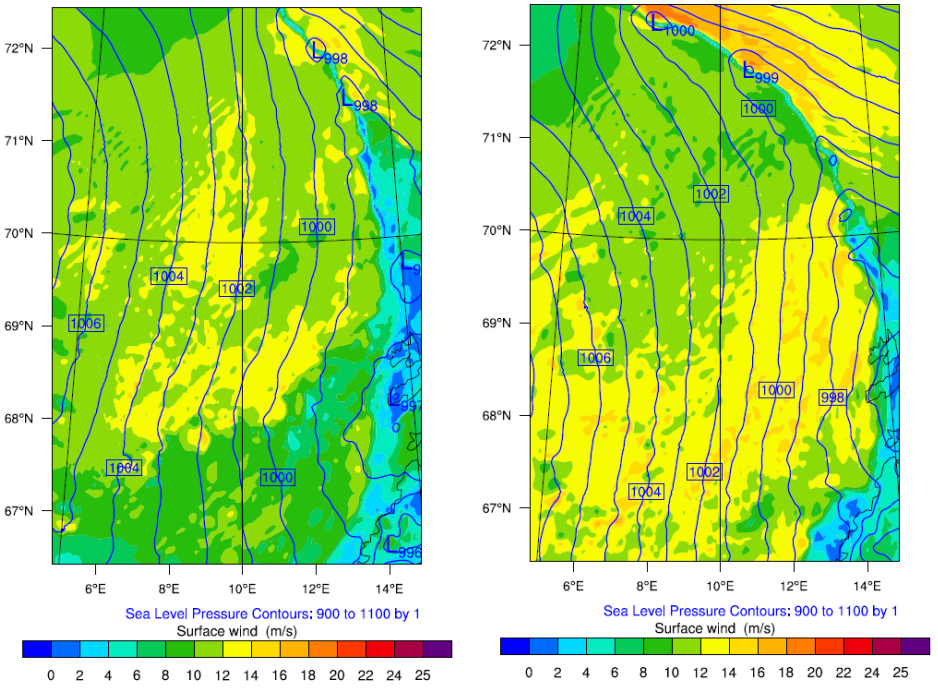

(a) 0600 UTC March 16.

(b) 1200 UTC March 16.

(c) 1800 UTC March 16.

(d) 0600 UTC March 17.

Figure 5.10: Surface pressure and wind fields from the high resolution WRF simulation initiated at 0000 UTC on March 15.

than the low produced by WRF1600. However, even though the minimum pressure is lower in the high resolution run, the pressure gradient is actually stronger in the coarse resolution run, and the wind field surrounding the low is also stronger in that run.

5.3.3 Evaluation of the high resolution simulations performance

The minimum pressures and locations of the lows closest to the path of the real low is summarized in table 5.4. On the whole, the performances of the high resolution runs were not convincing compared to the coarse grid runs. One of the most interesting component in these cases, is the fact that the high resolution runs produced one or more lows following closely in the wake of the first low, and also several small short-lived lows.

It is interesting to note that the late initial time does not appear to affect the performance of WRF16HR negatively, as in the similar high resolution experiment in McInnes et al. (2011). . When computational cost also is taken into account, it is beyond doubt that the relatively low resolution runs are preferable.

5.4 Different parametrisation options

The results from the third set of simulations where different physics options have been used are presented in this section. The difference between the options chosen are described in chapter 3. All the model simulations in this section were initiated at 0000 UTC on March 15, and only one parameter was changed from the original set during each simulation. The original domains and grid spacing were used.

5.4.1 Bulk microphysics scheme

The first scheme to be changed was the bulk microphysics scheme, that was changed from Lin et al. to the WRF Single-Moment 6-class (WSM6) scheme. Wu and Petty (2010) state that previous studies have shown that latent heat release in the convection process is crucial in order to obtain sufficient strong development of polar lows, and so a realistic treatment of cloud and precipitation processes is important for numerical simulation of polar lows. The article concludes that none of the different bulk microphysics schemes seemed to affect the position of the low, whereas the WSM6 scheme produced the

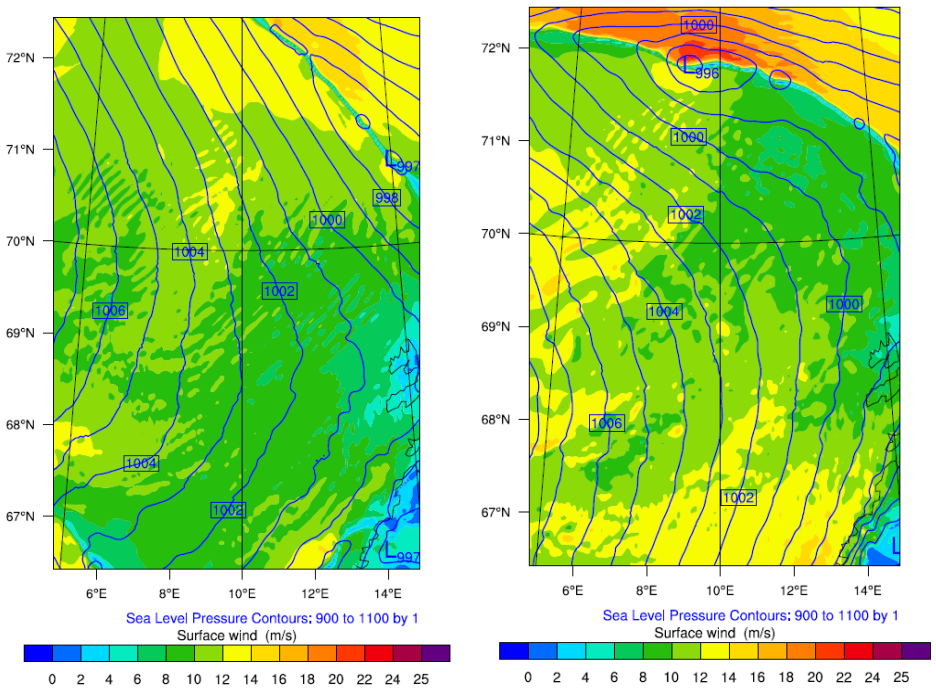

(a) 0600 UTC March 16.

(b) 1200 UTC March 16.

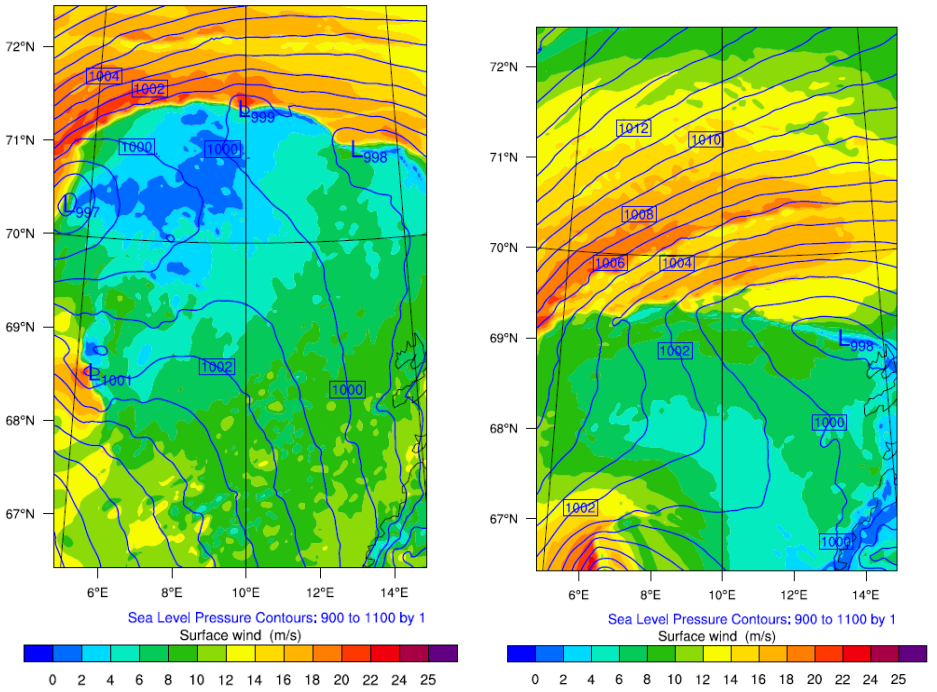

(c) 1800 UTC March 16.

(d) 0600 UTC March 17.

Figure 5.11: Surface pressure and wind fields from the high resolution WRF simulation initiated at 0000 UTC on March 16.

Time (UTC)	Position ECMWF analysis	Position WRF15HR	Position WRF16HR	Min. surface pressure ECMWF (hPa)	Min. surface pressure WRF15HR (hPa)	Min. surface pressure WRF16HR (hPa)
0000 March 16	70N 17E	71N 13E	-	1000	1001	-
0600 March 16	70.5N 16E	71.5N 13E	71N 15E	997	998	997
1200 March 16	72N 11E	71.5N 11E	72N 8E	996	999	996
1800 March 16	70.5N 7.5E	71N 4E	72N 8E	995	999	997
0000 March 17	69N 7E	68N 4E	67.5N 7.5E	996	1001	995
0600 March 17	66.5N 7.5E	65N 6E	65.5N 9.5E	996	997	994
Landfall	63.5 10E	64N 9E	64N 10E	time: 1200 March 17	time: 1000 March 17	time: 1200 March 17

Table 5.4: Minimum surface pressure and position of the polar lows in the high resolution simulations.

most realistic cloud and precipitation processes during the polar low events. Therefore this scheme was tested in the present study.

This run is called WRFMP and the results are shown in figure 5.12. At 0000 UTC on March 16, there are a couple of small lows present. The most evident is stationed at 73.5°N and 7.5°E, with a minimum pressure of 1001hPa. There is another rather clear low, L2, near 71.5°N and 16°E just outside the coast of Troms and where the real low also develops at that time. L2 has a minimum pressure of 1001hPa. The results at 0000 UTC March 16 strongly resemble WRF1500, which also has two small lows in the same area, but with a more well-defined second low.
During the next few hours until 0600 UTC (figure 5.12(a)), both lows develop further. L1 moves southwards, and L2 to the north. L2 appears to move faster than the similar low in WRF1500 and is also more evident, with

a minimum pressure of 999hPa. But there is still no huge difference between the two runs. L1 is almost exactly the same as in the reference run.
The big differences do not show up until 1200 UTC, shown in figure 5.12(b). L2 has nearly disappeared in this figure, but in the same figure in WRF1500, L2 has even strengthened and is more evident than L1. The remnants of L2 are positioned at 72°N and 9°E. L1, however, has deepened and moved towards the south with a minimum pressure of 999hPa, just like the similar low in WRF1500. It is now stationed at 70°N and 7.5°E, still too far southwest of the real low.
From 1200 to 1800 UTC (figure 5.12(c)), L1 continues southwards and remains quite weak. Another low develops shortly after 1200 UTC and continues to strengthen until 1800 UTC. This new low, L3, is stationed close to 70°N and 10°E, closer to the real polar low than L1 at the time. Minimum pressure in L3 is 997hPa, while L1 remains constant at 999hPa. In WRF1500, there are no new lows developing within this time interval, but L2 remains present and moves southwest. In contrast to WRFMP, L1 in WRF1500 has deepened and is now positioned more to the south.
During the night and early morning hours, the model forecasts L1 to deepen, and L3 to dissipate. L1 makes landfall between 0200-0400 UTC at the coast of Nordland and Trøndelag, 2-4 hours earlier than L1 in WRF1500, and 10-12 hours earlier than the real low.
This model run was not significantly different from WRF1500. L1 was very similar in the two runs, with only some differences in the hours around 0000 on March 1700. The largest difference was the development and strength of additional lows to L1, and L2 in particular since this is the low that developed and followed the path of the real low closest. L2 in this run was much weaker than L2 in WRF1500 and dissipates halfway into the simulation. Additionally, the position of the low is also further away from the real low. Hence it must be concluded that this simulation performed worse than WRF1500 with the Purdue Lin scheme. It appears that the WSM6 scheme overestimated the depth of L1 and underestimated the depth of L2. But it could also be that the difference observed between the two model simulations is more due to the chaotic behavior of the atmosphere, rather than the different processes in the microphysics schemes.

5.4.2 Cumulus scheme

The Grell-3 cumulus scheme was switched to the Kain-Fritsch cumulus scheme. As the Grell-3 scheme has not been tested out extensively for polar low simulation, it is interesting to compare it with the more common Kain-Fritsch scheme.

Results are shown in figure 5.13, and the simulation is called WRFCU. At

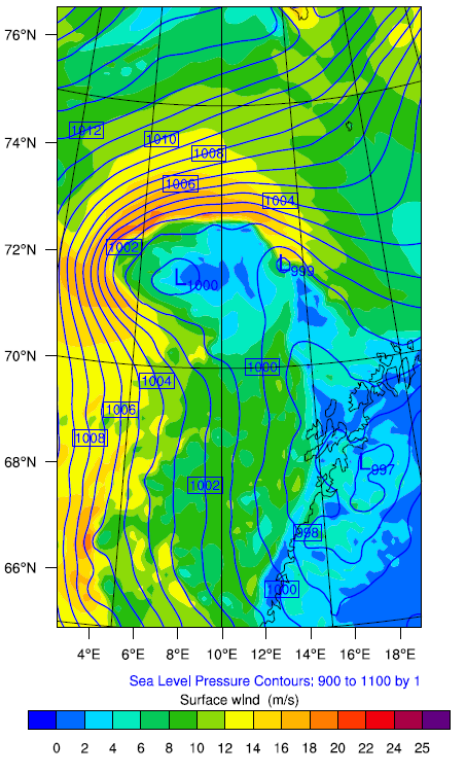

(a) 0600 UTC March 16.

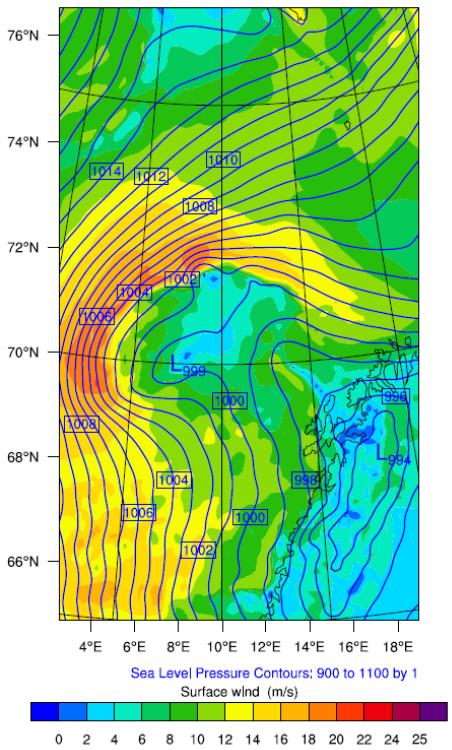

(b) 1200 UTC March 16.

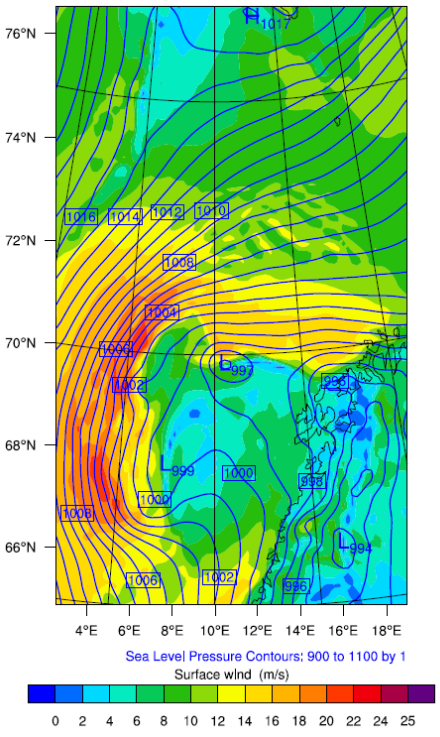

(c) 1800 UTC March 16.

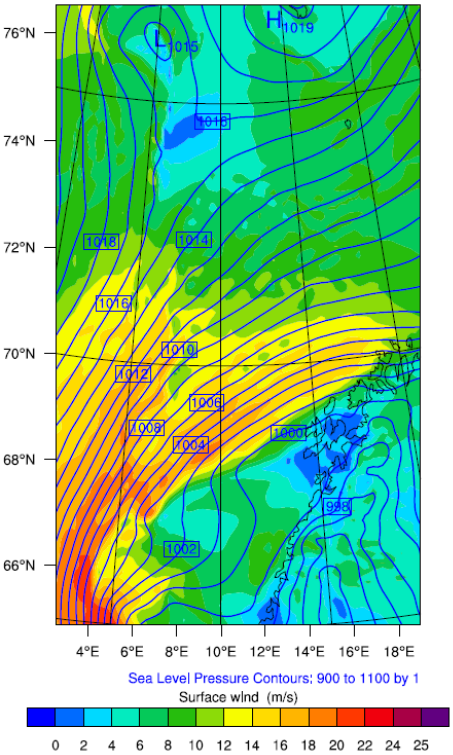

(d) 0600 UTC March 17.

Figure 5.12: Surface pressure and wind fields from the microphysics experiment WRF simulation initiated at 0000 UTC on March 15.

0000 UTC, the results are quite similar to the WRFMP run, with two lows present. One at 73.5°N and 7.5°E (L1) and the other at 71.5°N and 15.5°E (L2), almost exactly where the two lows from the previous run were stationed at the same time. Both of the lows are quite weak, with minimum pressure of 1000hPa. From 0000 to 0600 UTC, L1 moves relatively fast southwards, while L2 remains almost stationary. Both lows have become more evident in figure 5.13(a). L1 is now positioned at 71.5°N and 8°E, too far west of the real polar low, but almost exactly where L1 in the reference run is stationed. L2 is settled a bit too far east of the real polar low, still at 71.5°N and 15.5°E, and is more evident than the reference L2. Minimum pressures of L1 and L2 low are 999hPa and 998hPa, respectively.
In the next couple of hours both lows weaken. At 1200 UTC seen in figure 5.13(b), L2 has vanished and L1 is not very evident in the surface pressure field. Still L1 is very close to the reference L1 both in position and strength, and these trends continues in the hours until 1800 UTC as well. L1 moves fast southwards, and regains some strength, as seen in figure 5.13(c). This is just like L1 in WRF1500. There are no signs of other development within the domain. Throughout the night and early morning hours, L1 strengthens and travels towards the Norwegian coast. The low makes landfall between 0600 and 0800 UTC on March 17 (figure 5.13(d)), just like L1 in WRF1500. The results in this simulation strongly resemble WRF1500 as well. L1 has almost exactly the same strength and trajectory throughout the whole life cycle. Once again the most interesting feature is additional lows. In this simulation, L2 vanished before 1200 UTC on March 16, and no other lows developed afterwards. Thus, it appears that the Kain-Fritsch cumulus scheme inhibited further growth of L2. Or it could be as mentioned in the previous section that the chaotic behavior of the atmosphere leads to this difference between the simulations.

5.4.3 Planetary Boundary Layer scheme

In this run, the Mellor-Yamada-Nakanishi-Niino (MYNN) planetary boundary layer scheme was used instead of the older Mellor-Yamada-Janjic TKE scheme. MYNN is a relatively new scheme and has been introduced to WRF to reduce the biases that the MYJ scheme have.

Figure 5.14 illustrates the results from this simulation, called WRFPBL. This simulation too starts up with two weak lows almost in the same places as in the previous runs, at 73°N and 8°E (L1) and 71°N and 16°E, (L2), at 0000 UTC on March 16. The pattern of movement of the two lows is also quite similar to the previous run, when L1 moves southwards, and L2 travels north-westward.
At 0600 UTC (seen in figure 5.14(a)), L1 and L2 are stationed at 72°N and 7°E and 71°N and 15°E, respectively. L1 is positioned further north than in

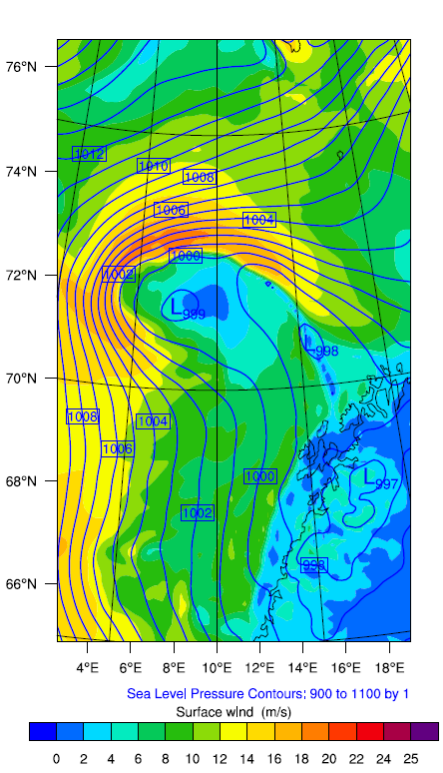

(a) 0600 UTC March 16.

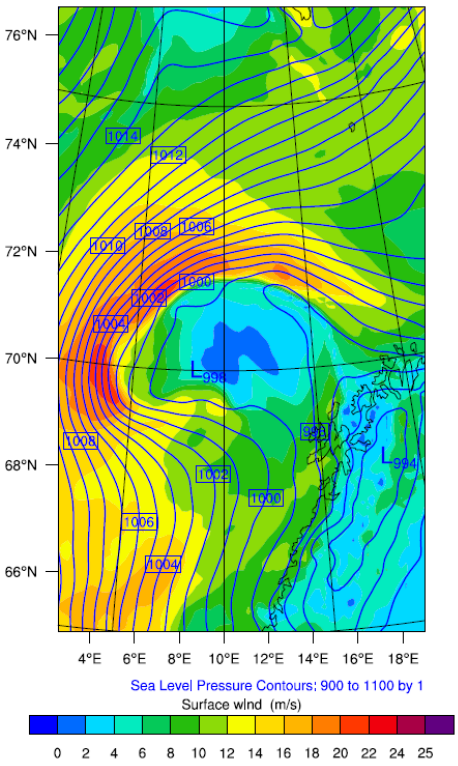

(b) 1200 UTC March 16.

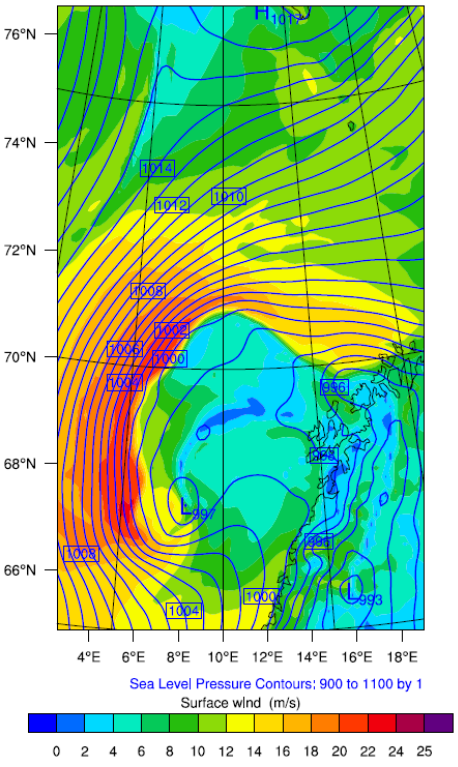

(c) 1800 UTC March 16.

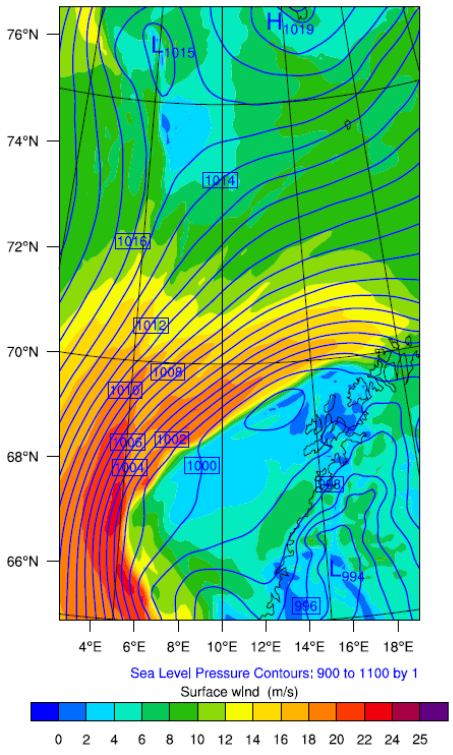

(d) 0600 UTC March 17.

Figure 5.13: Surface pressure and wind fields from the cumulus experiment WRF simulation initiated at 0000 UTC on March 15.

WRF1500, with a minimum pressure of 999hPa. L2 has the right latitude, but is positioned 1°too far west compared with the ECMWF-analysis. L2 has a minimum pressure of 998hPa, similar to L2 in WRF1500.
Figure 5.14(b) shows the results at 1200 UTC on March 16. Once again, the figure is very similar to the WRF1500 run. L1 has now traveled further southwards and become weaker, while the strength of L2 remains constant, and the movements are directed westward. Its coordinates are 71.5°N and 11.5°E, very close to the approximate center of the low from the analysis.
L2 continues south-westwards during the next hours and still remains almost constant in strength. Figure 5.14(c) illustrates the results from 1800 UTC. L2 is now too far south compared with the ECMWF-analysis. L1 has regained some strength and is now positioned at 68°N and 8°E, to the north of L1 in WRF1500, but still too far south of the real low. A key feature of this simulation occurs in the evening hours up to midnight on March 17. L1 and L2 move closer and merge into each other around 0000 UTC on March 17. The combined low continues southwards and deepens before making landfall at the coast of Trøndelag around 0600 UTC, seen in figure 5.14(d).
The most interesting feature of this simulation is the merging of the two lows in the evening hours of March 16. This is consistent with the satellite images, which show a possible merge between PL and V2 around 1800 UTC on March 16. The satellite images also show a distinct change in the structure of the polar low after this, which can also be seen in this run, as the combined low strengthens rapidly afterwards. Otherwise it was quite similar to the WRF1500 run, but with a more accurate trajectory compared with the satellite images.

5.4.4 Evaluation of the performance of the different physics parametrisation schemes

There was generally little difference between the simulations with different choices of parametrization of cumulus clouds, bulk microphysics and planetary boundary layer. All of the simulations had a quite significant first low, L1, that was present during the whole simulation, before making landfall at approximately the same place and time. The most important factor, L2, however, deviated much between the simulations. The position and minimum pressure of L2 from the three simulations, along with the ECMWF-analysis are summarized in table 5.5. WRFMP and WRFCU did not perform very well, as L2 dissipated after a short period of time. As the relative positions and minimum pressures also deviated more from the ECMWF-analysis than WRF1500, it is clear that the Purdue Lin bulk microphysics scheme and Grell 3D cumulus scheme are preferable in this particular polar low case.
The most accurate simulation was WRFPBL, where L1 and L2 merged halfway into the simulation. L2 was also more intense than L1 during most

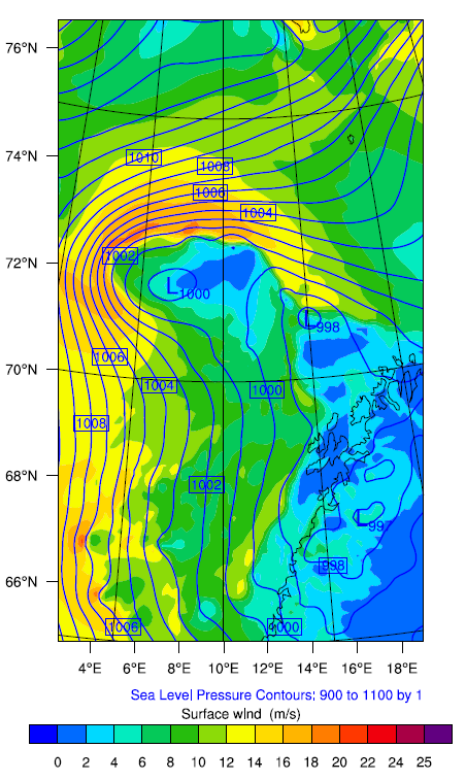

(a) 0600 UTC March 16.

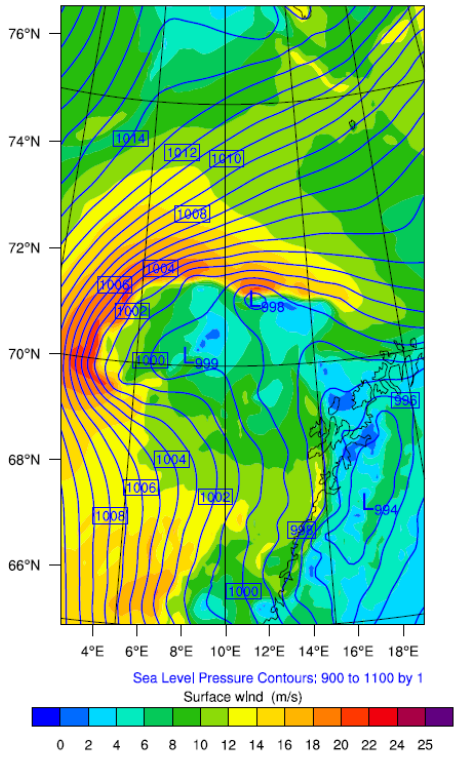

(b) 1200 UTC March 16.

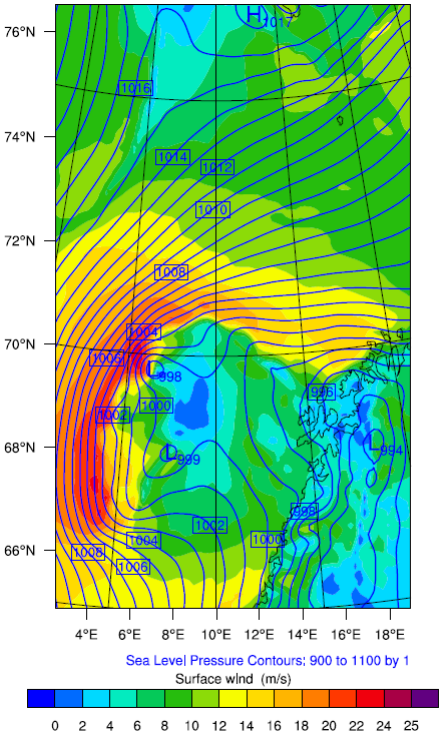

(c) 1800 UTC March 16.

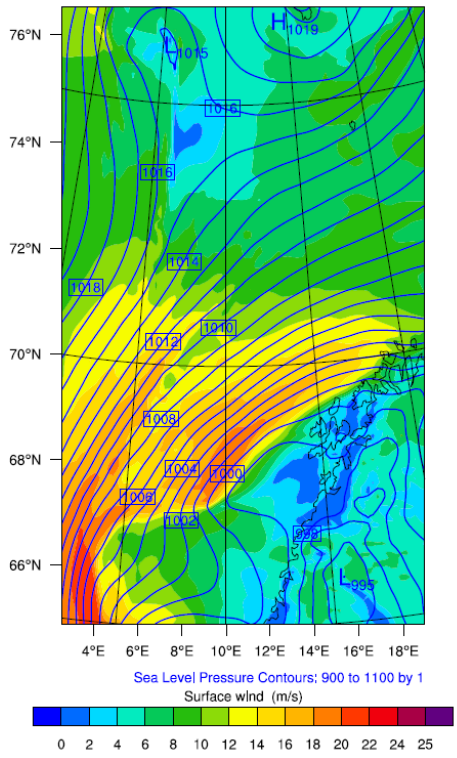

(d) 0600 UTC March 17.

Figure 5.14: Surface pressure and wind fields from the planetary boundary layer experiment WRF simulation initiated at 0000 UTC on March 15.

Time	Position ECMWF analysis	Position WRFMP	Position WRFCU	Position WRF-PBL	Min. surface pressure ECMWF (hPa)	Min. surface pressure WRFMP (hPa)	Min. surface pressure WRFCU (hPa)	Min. surface pressure WRF-PBL (hPa)
0000 March 16	70N 17E	71N 16E	71N 15.5E	71N 17E	1000	1001	1000	1000
0600 March 16	70.5N 16E	72N 14E	71N 16E	71N 15E	997	999	998	998
1200 March 16	72N 11E	72N 9E	-	71N 12E	996	1001	-	998
1800 March 16	70.5N 7.5E	-	-	69.5N 6E	995	-	-	998
0000 March 17	69N 7E	-	-	66.5N 6.5E	996	-	-	999
0600 March 17	66.5N 7.5E	-	-	-	996	-	-	-
Landfall	63.5N 10E	-	-	64N 9.5E	time: 1200 March 17	-	-	time: 0600 March 17

Table 5.5: Minimum surface pressure and position of the polar lows in the different parametrisation scheme simulations.

of the simulation, and the positions and minimum pressures of L2 matched the ECMWF-analysis much better than both WRFMP and WRFCU. The WRF1500 run performed slightly better in predicting the minimum pressures and positions of the low, but did not predict any landfall, which WRFPBL did. This suggests that the WRFPBL model outperformed WRF1500 during this polar low event.

Chapter 6

Summary and conclusion

In this thesis, the March 16-17 2008 polar low over the Norwegian Sea has been studied and simulated. The polar low developed rapidly during the night of March 16 2008, and was poorly forecasted by the operational models. This thesis sought to find out why the polar low was difficult to forecast, and if the numerical weather prediction (NWP) model weather research and forecasting (WRF), is able to provide a better forecast. The weather analysis consisted of satellite images and ECMWF model analyses, as well as observations provided by dropsonde data. WRF was used to simulate the polar low event in a number of sensitivity studies, investigating the impact of different initial times, high resolution simulations, and different parametrization schemes for bulk microphysics, cumulus clouds and planetary boundary layer (PBL), on the simulations behavior.

The weather analysis showed that the polar low developed in a confluence zone between arctic and polar air. Satellite images revealed several vortices within this confluence zone, but only the south-easternmost developed into a polar low. There was an area of particularly high clouds around this vortex and it was close to a surface low. Six hours later the surface low was stretched to cover also the area of high clouds, and a rotation was evident within the cloud area. The cross section taken twelve hours before cyclogenesis, revealed high baroclinicity within the whole cross section, and showed high surface temperatures and low static stability in the lower troposphere close to the area of cyclogenesis. This could be the reason why this vortex developed further into a polar low and the two others dissipated after a short period of time. The cyclogenesis was aided by an upper-level region of high potential vorticity, advancing over the whole confluence zone, as well as a lower-level absolute vorticity maximum close to the surface low. At the early stage, the low takes on a comma shape, but later transforms into a spiraliformed polar low. Cross sections from March 17 showed that the mature low had little baroclinicity, and it was therefore concluded that the forcing mechanisms at

this stage of the low were mainly convective and aided by the upper-level PV-anomaly.

Results from the WRF simulations revealed that the March 16-17 polar low was particularly unpredictable. All of the different initial time simulations initiated before cyclogenesis deviated much from each other, and there was no clear improvement from the long lead-time to the short-lead time simulations. Many of the simulations produced more than one low, which could be connected with the multiple vortices found in the satellite images during cyclogenesis. Some of these additional lows were predicted to be just as significant as, or even deeper than the low closest to the trajectory of the real low.
Another common error was that the polar low moved too far west and too fast southwards. The lows produced by the post-cyclogenesis runs were significantly deeper than the lows produced by the pre-cyclogenesis runs, indicating that the rapid cyclogenesis stage was particularly difficult to model. However, a small low that developed south-west of Spitsbergen at the end of the simulation was picket up by all of the simulations, indicating that the March 16-17 low was very difficult to forecast.
In contrast to other studies like McInnes et al. (2011), the high resolution runs did not improve the performance of the model significantly. This could be linked to the cumulus parametrization scheme used in this study, compared with similar studies. When the cumulus scheme was switched to a different scheme, the model appeared to favor development of another low, instead of the low closest to the real low. A similar development was seen when the bulk microphysics scheme was switched. The only scheme change that made an improvement was when the PBL scheme was changed, as the new scheme appeared to favor development of the "right" low, and ended up with a merge between the two lows.

Although the results of the WRF simulations differed from each other and had room for many improvements, they still performed much better than the operational prognosis from HIRLAM, and also the experiments carried out by McInnes et al. (2011) with UM. All of the simulations lead to a development of at least one low, so it could give a warning of possible polar low development already three days ahead. Most of the simulations initiated after one day prior to cyclogenesis, predicted development in the right area. The position of landfall did not differ much between the simulations, but time varied from 2200 UTC on March 16 to 1200 UTC on March 17.

The conclusions of this study are summarized here:

1) The polar low developed during particularly challenging weather conditions, involving multiple vortices and interaction of different forcing mechanisms like baroclinicity, upper-level PV-anomaly, convective clouds and low-level absolute vorticity maximum.

2) The WRF simulations provided a much improved forecast, but still had trouble particularly regarding multiple lows, rapid deepening during cyclogenesis and trajectory of the low.

6.1 Further work

McInnes et al. (2011) suggested that the UMs failure to simulate the March 16-17 polar low, could be partly due to the quality of the lateral boundary conditions, as only 48h predictions were used. Randriamampianina et al. (2011) improved the forecast by using the ECMWF analysis and adding the infrared atmospheric sounding interferometer (IASI), but it still predicted that the low would develop at the northwestern part of the confluence zone. It is difficult to compare the present study directly to Randriamampianina et al. (2011), but even without the extra observations added to the lateral boundary conditions, the WRF simulations initiated at 0000 UTC on March 15 and 0000 UTC on March 16 placed the low within 1°radius away from the ECMWF-analysis at 1200 UTC on March 16. The WRF nesting option provides the inner domain with lateral boundary conditions from the parent domain, and this could be a reason why the WRF simulations performed better than the other models. A new study where the performance of WRF with and without nesting is compared could reveal if this is the case.

It is without a doubt that the weather conditions during cyclogenesis were challenging, as there were several vortices involved. A closer investigation of the forcing mechanisms, could answer why this particular vortex developed into a polar low. For instance the contribution of PV-anomalies at different altitudes using PV inversion, similar to the investigations carried out by Føre et al. (2011), Bracegirdle and Gray (2009) and Wu et al. (2011). More model simulations, with surface fluxes of heat and moisture turned off or reduced (McInnes et al. (2011) and Bracegirdle and Gray (2009)), could also reveal more about the relative importance of CISK and particularly WISHE.

The experiments carried out in this thesis regarding parametrisation schemes, could indicate sensitivity to different schemes. New comparison studies like Wu and Petty (2010) with focus on cumulus schemes and particularly PBL

schemes, could shed light on the effects of these schemes on polar low modelling. Comparison studies would therefore be useful for future research.

References

Aspelien, T., T. Iversen, J. B. Bremnes, and I.-L. Frogner (2011). Short-range probabilistic forecasts from the norwegian limited-area eps: long-term validation and a polar low study. *Tellus*.

Bjørnæs, C. (2008). Flyr inn i arktisk uvær. `http://www.ipy-thorpex.no/no/feltarbeid/andoeya-2008/flyr-inn-i-arktisk%-uvaer`. Accessed: 30.11.11.

Blechschmidt, A.-M. (2008, May). A 2-year climatology of polar low events over the nordic seas from satellite remote sensing. *Geophysical research letters 35*.

Blechschmidt, A. M., S. Bakan, and H. Grassl (2009). Large-scale atmospheric circulation patterns during polar low events over the nordic seas. *Journal of geophysical research*.

Bracegirdle, T. J. and S. L. Gray (2008, February). An objective climatology of the dynamical forcing of polar lows in the nordic seas. *International Journal of Climatology 28*, 1903–1919.

Bracegirdle, T. J. and S. L. Gray (2009). The dynamics of a polar low assessed using potential vorticity inversion. *Quarterly journal of the royal meteorological society*.

Craig, G. C. and S. L. Gray (1996). Cisk or wishe as the mechanism for tropical cyclone intensification. *Journal of the atmospheric sciences*.

Dudhia, J. Microphysics options in wrf. `http://www.mmm.ucar.edu/wrf/users/workshops/WS2010/presentations/Lectur%es/Microphysics10.pdf`. Accessed: 30.11.11.

Føre, I., J. E. Kristjánsson, Øyvind Saetra, Øyvind Breivik, B. Røsting, and M. Shapiro (2011). The full life cycle of a polar low over the norwegian sea observed by three research aircraft flights. *Quarterly Journal of the Royal Meteorological Society*.

Gill, D. and M. Pyle (2008). Wrf nesting. `http://http://www.mmm.ucar.edu/wrf/users/tutorial/200801/WRFNesting.pdf%`. Accessed: 30.11.11.

Hodnebrog, Ø. (2008, June). Impact of fine scale variability on large scale atmospheric chemistry. Master's thesis, University of Oslo, Institute of Geosciences, Department of meteorology and oceanography.

Holton, J. R. (2004). *An Introduction to Dynamic Meteorology*. Elsevier academic press.

Kolstad, E. W. (2006). A new climatology of favourable conditions for reverse-shear polar lows. *Tellus*.

Kolstad, E. W., T. J. Bracegirdle, and I. A. Seierstad (2008). Marine cold-air outbreaks in the north atlantic: temporal distribution and associations with large-scale atmospheric circulation. *Clim Dyn 33*, 187–197.

Kristiansen, J., S. L. Sørland, T. Iversen, D. Bjørge, and M. Ødegaard Køltzow (2011). High-resolution ensemble prediction of a polar low development. *Tellus*.

Kristjánsson, J. E., I. Barstad, T. Aspelien, I. Føre, Ø.Godøy, Ø. Hov, E. Irvine, T. Iversen, E. Kolstad, T.E.Nordeng, H. McInnes, R. Randriamampianina, J. Reuder, Ø. Saetra, M. Shapiro, T. Spengler, and H. Ólafsson (2011). The norwegian ipy-thorpex: Polar lows and arctic fronts during the 2008 andøya campaign. *Bulletin of the American Meteorological Society*. (in press).

Linders, T. and Ø. Saetra (2010, August). Can cape maintain polar lows? *Journal of the atmospheric sciences 67*, 2559–2571.

McInnes, H., J. Kristiansen, J. E. Kristjánsson, and H. Schyberg (2011). The role of horizontal resolution for polar low simulations. *Quarterly Journal of the Royal Meteorological Society*.

Olson, J. B. and J. M. Brown. A comparison of two mellor-yamada-based pbl schemes in simulation a hybrid barrier jet. P2B.4.

Randriamampianina, R., T. Iversen, and A. Storto (2011, October). Exploring the assimiliation of iasi radiances in forecasting polar lows. *Quartely Journal of the Royal Meteorological Society 137*, 1700–1715.

Rasmussen, E. A. and J. Turner (Eds.) (2003). *Polar Lows*. Cambridge university press.

Skamarock, W. C. and J. B. Klemp (2007). A time-split nonhydrostatic atmospheric model for weather research and forecasting applications. *Journal of Computational Physics*.

Skamarock, W. C., J. B. Klemp, J. Dudhia, D. O. Gill, D. M. Barker, M. G. Duda, X.-Y. Huang, W. Wang, and J. G. Powers (2008, June). *A Description of the Advanced Research WRF Version 3*. Boulder, Colorado, USA: National Center for Atmospheric Research, Mesoscale and Microscale Meteorology Division.

Wagner, J., A. Gohm, A. Dörnbrack, and A. Schäfler (2011, July). The mesoscale structure of a polar low: airborne lidar measurments and simulations. *Quaterly Journal of the Royal Meteorological Society* (137), 1516–1531.

Wallace, J. M. and P. V. Hobbs (2006). *Atmospheric Science: An introductory survey* (2nd ed.). Elsevier Inc.

Wang, W. and N. L. Seaman (1996). A comparison study of convective parameterization schemes in a mesoscale model. *Monthly Weather Review 125*, 252–278.

Wu, L., J. E. Martin, and G. W. Petty (2011). Piecewise potential vorticity diagnosis of the development of a polar low over the sea of japan. *Tellus 63A*, 198–211.

Wu, L. and G. W. Petty (2010, June). Intercomparison of bulk microphysics schemes in model simulations of polar lows. *Monthly Weather Review 138*, 2211–2228.

Yanase, W., H. Niino, and K. Saito (2002). High-resolution numerical simulation of a polar low. *Geophysical Research Letters 29*(14).